

TECHNISCHE
UNIVERSITÄT
DRESDEN

Flooding of Regular Phase Space Islands by Chaotic States

Dissertation
zur Erlangung des akademischen Grades
Doctor rerum naturalium

vorgelegt von

Lars Bittrich

geboren am 29.06.1981 in Görlitz

Institut für Theoretische Physik
Fachrichtung Physik
Fakultät für Mathematik und Naturwissenschaften
Technische Universität Dresden

2010

Eingereicht am 23. Juni 2010

1. Gutachter: Prof. Dr. Roland Ketzmerick
2. Gutachter: Prof. Dr. Hans-Jürgen Stöckmann

Verteidigt am 26. Oktober 2010

Abstract

We investigate systems with a mixed phase space, where regular and chaotic dynamics coexist. Classically, regions with regular motion, the regular islands, are dynamically not connected to regions with chaotic motion, the chaotic sea. Typically, this is also reflected in the quantum properties, where eigenstates either concentrate on the regular or the chaotic regions. However, it was shown that quantum mechanically, due to the tunneling process, a coupling is induced and flooding of regular islands may occur. This happens when the Heisenberg time, the time needed to resolve the discrete spectrum, is larger than the tunneling time from the regular region to the chaotic sea. In this case the regular eigenstates disappear. We study this effect by the time evolution of wave packets initially started in the chaotic sea and find increasing probability in the regular island. Using random matrix models a quantitative prediction is derived. We find excellent agreement with numerical data obtained for quantum maps and billiards systems. For open systems we investigate the phenomenon of flooding and disappearance of regular states, where the escape time occurs as an additional time scale. We discuss the reappearance of regular states in the case of strongly opened systems. This is demonstrated numerically for quantum maps and experimentally for a mushroom shaped microwave resonator. The reappearance of regular states is explained qualitatively by a matrix model.

Zusammenfassung

Untersucht werden Systeme mit gemischtem Phasenraum, in denen sowohl reguläre als auch chaotische Dynamik auftritt. In der klassischen Mechanik sind Gebiete regulärer Bewegung, die sogenannten regulären Inseln, dynamisch nicht mit den Gebieten chaotischer Bewegung, der chaotischen See, verbunden. Dieses Verhalten spiegelt sich typischerweise auch in den quantenmechanischen Eigenschaften wider, so dass Eigenfunktionen entweder auf chaotischen oder regulären Gebieten konzentriert sind. Es wurde jedoch gezeigt, dass aufgrund des Tunneleffektes eine Kopplung auftritt und reguläre Inseln geflutet werden können. Dies geschieht wenn die Heisenbergzeit, das heißt die Zeit die das System benötigt, um das diskrete Spektrum aufzulösen, größer als die Tunnelzeit vom Regulären ins Chaotische ist, wobei reguläre Eigenzustände verschwinden. Dieser Effekt wird über eine Zeitentwicklung von Wellenpaketen, die in der chaotischen See gestartet werden, untersucht. Es kommt zu einer ansteigenden Wahrscheinlichkeit in der regulären Insel. Mithilfe von Zufallmatrixmodellen wird eine quantitative Vorhersage abgeleitet, welche die numerischen Daten von Quantenabbildungen und Billardsystemen hervorragend beschreibt. Der Effekt des Flutens und das Verschwinden regulärer Zustände wird ebenfalls mit offenen Systemen untersucht. Hier tritt die Fluchtzeit als zusätzliche Zeitskala auf. Das Wiederkehren regulärer Zustände im Falle stark geöffneter Systeme wird qualitativ mithilfe eines Matrixmodells erklärt und numerisch für Quantenabbildungen sowie experimentell für einen pilzförmigen Mikrowellenresonator belegt.

Contents

| | | |
|----------|---|-----------|
| 1 | Introduction | 1 |
| 2 | Systems with a mixed phase space | 5 |
| 2.1 | Kicked maps | 5 |
| 2.1.1 | Standard map | 6 |
| 2.1.2 | Designed kicked maps | 8 |
| 2.2 | Quantized torus maps | 9 |
| 2.2.1 | Time evolution operator | 12 |
| 2.2.2 | Quasi-periodic potential and kinetic energy functions | 13 |
| 2.3 | Mushroom billiard | 14 |
| 3 | Flooding of regular states | 17 |
| 3.1 | Numerical time evolution in quantum maps | 17 |
| 3.1.1 | Husimi weight | 17 |
| 3.1.2 | Projection onto regular states | 19 |
| 3.2 | Dynamical tunneling | 26 |
| 3.2.1 | Linear regime | 26 |
| 3.2.2 | Complete flooding | 29 |
| 3.3 | Saturation regime | 32 |
| 3.3.1 | Saturation value and effective coupling | 32 |
| 3.3.2 | Random matrix model | 36 |
| 3.3.3 | Simplified RMT model | 38 |
| 3.3.4 | Non-transporting islands | 40 |
| 3.4 | Full time-dependent solution | 42 |
| 3.5 | Flooding in the standard map | 46 |
| 3.6 | Flooding in the mushroom billiard | 50 |
| 4 | Flooding in open quantum systems | 53 |
| 4.1 | Open quantum maps | 53 |
| 4.1.1 | Reappearance of regular states | 55 |
| 4.1.2 | Matrix model | 57 |
| 4.2 | Experiments in microwave billiards | 59 |

| | | |
|----------|---|------------|
| 4.2.1 | Experimental setup | 61 |
| 4.2.2 | Transmission and reflection measurements | 61 |
| 4.2.3 | Wave functions measurements | 63 |
| 4.2.4 | Reappearance of regular states | 68 |
| 5 | Summary and outlook | 73 |
| A | Classical and quantum kicked systems | 77 |
| A.1 | System-adapted units | 77 |
| A.2 | Smoothing of designed maps | 78 |
| B | Numerics with quantum maps | 81 |
| B.1 | Time evolution of wave packets | 81 |
| B.2 | Efficient calculations of the Husimi function | 85 |
| B.3 | Numerical errors in the regular weight | 87 |
| C | Analytic solutions of the matrix models | 89 |
| C.1 | Saturation value | 89 |
| C.2 | Two by two coupling model | 91 |
| C.3 | Non-transporting islands | 94 |
| D | Adjustment of the antenna positioning in the microwave billiard experiment | 95 |
| | Bibliography | 101 |

1 Introduction

In this thesis we investigate quantum systems for which the corresponding classical dynamics shows a mixed phase space. In such systems regular and chaotic motion coexist. The regular motion is stable under small variations of the initial conditions, whereas in chaotic regions even tiny changes of initial conditions lead to an exponential separation in phase space. The understanding of quantum mechanical properties of systems with a mixed phase space is an important topic of current research in quantum chaos [1–3]. In the past decades many important results have been obtained considering systems, which are either completely regular or completely chaotic [4–6]. Typical Hamiltonian systems, however, have a mixed phase space [7]. An example of such a system is presented in Fig. 1.1(a). Regular trajectories (red) show an elliptical shape and together they form the so-called regular island, while the chaotic trajectories (blue) are distributed over two-dimensional regions in phase space, the so-called chaotic sea. One aim in the field of quantum chaos is to understand the quantum mechanical properties of such systems by means of classical trajectories. For this purpose typical actions S of the system have to be large in comparison with Planck's constant \hbar . The corresponding limit $\frac{S}{\hbar} \rightarrow \infty$ can be described by an effective Planck constant $h_{\text{eff}} = \frac{\hbar}{S}$, which goes to zero in the semiclassical limit. In this limit quantum mechanical eigenfunctions localize on classical structures in phase space and thus they can be classified as regular or chaotic. This behavior is predicted by the semiclassical eigenfunction hypothesis [8–10]. Even in the quantum regime for finite $h_{\text{eff}} \neq 0$ one often finds regular states as shown in Fig. 1.1(b) and chaotic states shown in Fig. 1.1(c), which is also verified in the literature [11–16].

Semiclassically one can construct by the WKB-quantization [17] purely regular states, which concentrate on classical regular tori \mathcal{C}_m , fulfilling the quantization condition

$$\oint_{\mathcal{C}_m} p dq = \left(m + \frac{1}{2}\right) h_{\text{eff}} . \quad (1.1)$$

These tori are shown as red ellipses in Fig. 1.1(a). This yields a fixed number of regular states, which only depends on the area of the regular island. For chaotic states no such construction exists, yet their statistical properties can be described by random matrix models [11, 18, 19]. However, due to the so-called dynamical tunneling [20], regular and chaotic states are coupled, in a way that no eigenfunction is purely regular or purely chaotic and a regular state decays to the chaotic sea with a characteristic rate, the tunneling rate γ_m . Usually this coupling is

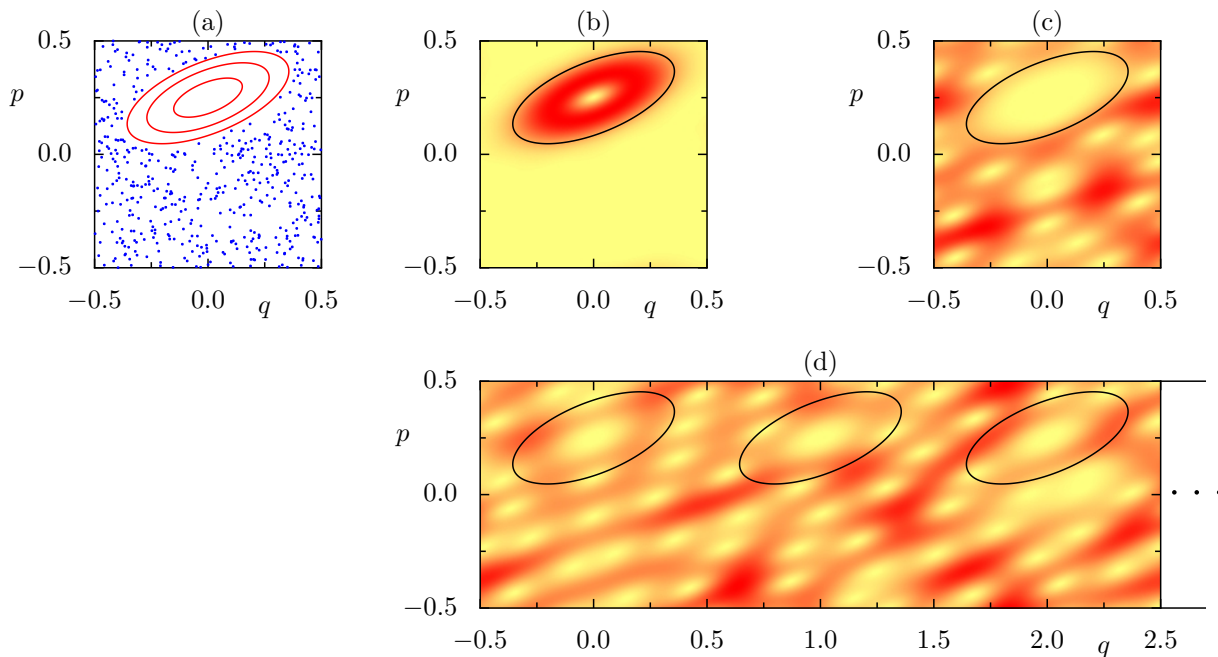


Figure 1.1: Flooding in a system with a mixed phase space: (a) classical phase space. The regular island consists of regular trajectories in red, whereas a chaotic trajectory is shown in blue. The Husimi function of a regular (b) and a chaotic (c) eigenfunction of the corresponding quantum system are shown in comparison. A flooded state (d) ignores the classical phase space structure and extends over chaotic and regular regions.

exponentially small and for each eigenfunction either chaotic or regular behavior dominates. In Ref. [21] the authors found eigenstates, which completely ignore classical phase space structures. These so-called flooded states, see Fig. 1.1(c), extend over both chaotic and regular regions in phase space. In systems with flooded states the effective coupling of regular and chaotic states is very strong, such that some regular states no longer exist, and an additional condition for the existence of regular states was found [22, 23]

$$\gamma_m < \frac{1}{\tau_{H, \text{ch}}} . \quad (1.2)$$

The tunneling rate γ_m of the regular state with quantum number m has to be smaller than the Heisenberg time $\tau_{H, \text{ch}} = \frac{\hbar_{\text{eff}}}{\Delta_{\text{ch}}}$ of the chaotic sea with mean level spacing Δ_{ch} . The knowledge about the flooding of regular states was used for example to explain the conductance behavior of nano wires with one-sided surface roughness [24, 25].

In this work we study the flooding of regular phase space islands by the time evolution of wave packets, which are initially localized within the chaotic sea. In contrast to the classical analog, where a trajectory remains in the chaotic sea for all times, the quantum mechanical probability in the regular island increases with time until a saturation plateau is reached. The height of this plateau is a measure for the amount of flooding in the system. A quantitative flooding criterion, based on the properties of eigenfunctions, is derived and numerical results

are compared to predictions obtained by numerically evaluated random matrix models. We find a universal behavior, which can be predicted by the analytic solution of a 2×2 matrix model. With the mushroom billiard we show, that also two dimensional systems can be described by this model.

So far all investigations of flooding have considered closed systems, which are difficult to access experimentally. Hence, we also study flooding in open quantum systems by introducing absorbing regions in phase space. In analogy to the analysis of eigenfunctions in closed systems we study the resonance states of open systems. When opening a system with flooded regular states, we find the reappearance of the corresponding regular states. Each resonance state decays, due to absorption, with a characteristic rate, the escape rate. With increasing absorption also the decay rates increase until a critical opening is reached. The coupling of regular and chaotic states, which leads to flooded states, vanishes at this point and a regular resonance reappears. The corresponding decay rate saturates or even decreases with further increasing absorption. Such a behavior is also called resonance trapping [26–28]. Using a matrix model the reappearance of regular states can be explained qualitatively.

We discuss the first experimental investigations of flooding using microwave billiards. Here, the similarity of Maxwells equations to the Schrödinger equation in two dimensions allows to study quantum systems with a mixed phase space via an analog macroscopic setup [29–32]. By measurement of the transmission properties in mushroom shaped microwave resonator we experimentally observe the reappearance of regular states.

This thesis is organized as follows: After the introductory Chapter 2, which discusses the properties of systems with a mixed phase space, we study flooding in closed quantum systems in Chapter 3. The reappearance of flooded regular states is investigated for quantum maps and in mushroom billiard experiments in Chapter 4. Finally, the thesis is concluded in Chapter 5 with a summary and outlook.

2 Systems with a mixed phase space

In this chapter we introduce the main concepts and properties of systems with a mixed phase space. We concentrate on area preserving maps and define the classical kicked maps used in this thesis in Sec. 2.1. The quantization of maps on the torus is discussed in Sec. 2.2. In Sec. 2.3 we introduce the two-dimensional mushroom billiard as another example with a mixed phase space. Unless explicitly stated we use system-adapted units. These are introduced for the kicked rotor in App. A.1.

2.1 Kicked maps

Classical kicked maps allow for a very easy modeling and understanding of systems with a mixed phase space, see Refs. [33, 34] for a detailed introduction. These systems are described by the explicitly time-dependent Hamiltonian

$$H(q, p, t) = T(p) + V(q) \sum_{n \in \mathbb{Z}} \delta(t - n) . \quad (2.1)$$

The kinetic energy T depends on the momentum p and the potential energy V on the position variable q .

Hamilton's equations of motion yield

$$\dot{q} = \frac{\partial H(q, p, t)}{\partial p} = T'(p) , \quad (2.2a)$$

$$\dot{p} = -\frac{\partial H(q, p, t)}{\partial q} = -V'(q) \sum_{n \in \mathbb{Z}} \delta(t - n) . \quad (2.2b)$$

We get a stroboscopic view of the solution of these equations by evaluating $q(t)$ and $p(t)$ just after the n -th kick

$$q_n = \lim_{\varepsilon \searrow 0} q(n + \varepsilon) , \quad (2.3a)$$

$$p_n = \lim_{\varepsilon \searrow 0} p(n + \varepsilon) . \quad (2.3b)$$

The sequence of successive phase space points (q_n, p_n) is called orbit. We define the mapping

\mathcal{M} via

$$\mathcal{M} : (q_n, p_n) \mapsto (q_{n+1}, p_{n+1}) . \quad (2.4)$$

By construction the momentum is constant between the kicks and thus the position changes linearly. The change in momentum is instant at each kick and the mapping yields by use of Eq. (2.2)

$$\mathcal{M} : \begin{aligned} q_{n+1} &= q_n + T'(p_n) \\ p_{n+1} &= p_n - V'(q_{n+1}) = p_n - V'(q_n + T'(p_n)) . \end{aligned} \quad (2.5)$$

In the following we introduce several kicked maps, which are used in this work.

2.1.1 Standard map

The first example is the Chirikov standard map [35]. The corresponding Hamiltonian describes the dynamics of a kicked rotor

$$H(q, p) = \frac{p^2}{2} + \frac{k}{(2\pi)^2} \cos(2\pi q) \sum_{n \in \mathbb{Z}} \delta(t - n) , \quad (2.6)$$

with kicking strength k . The transformation from metric units to the system-adapted units is shown in App. A.1 for the standard map. With Eq. (2.5) one obtains

$$\tilde{\mathcal{M}}_{\text{standard}} : \begin{aligned} q_{n+1} &= q_n + p_n \\ p_{n+1} &= p_n + \frac{k}{2\pi} \sin(2\pi[q_n + p_n]) . \end{aligned} \quad (2.7)$$

The Hamiltonian is invariant to translations in position space

$$H(q + 1, p) = H(q, p) . \quad (2.8)$$

The mapping in phase space is also invariant under integer translations in momentum direction

$$p_{n+1} = p_n + \frac{k}{2\pi} \sin(2\pi[q_n + p_n]) \Leftrightarrow p_{n+1} + 1 = p_n + 1 + \frac{k}{2\pi} \sin(2\pi[q_n + p_n + 1]) . \quad (2.9)$$

Although the total number of full rotations of the kicked rotor between the kicks is changed by this translation, one defines the mapping $\mathcal{M}_{\text{standard}}$ by use of the modulo operation in both coordinates q and p

$$\mathcal{M}_{\text{standard}} : \begin{aligned} q_{n+1} &= (q_n + p_n) \bmod 1 \\ p_{n+1} &= \left[\left(p_n + \frac{k}{2\pi} \sin 2\pi q_{n+1} + \frac{1}{2} \right) \bmod 1 \right] - \frac{1}{2} . \end{aligned} \quad (2.10)$$

This reduces the mapping to the torus $[0, 1] \times [-\frac{1}{2}, \frac{1}{2}]$. The application of this mapping is shown in Fig. 2.1 for various kicking strengths k . For $k = 0$ the system is integrable because of momentum conservation as shown in (a) and the horizontal lines are regular tori. For small

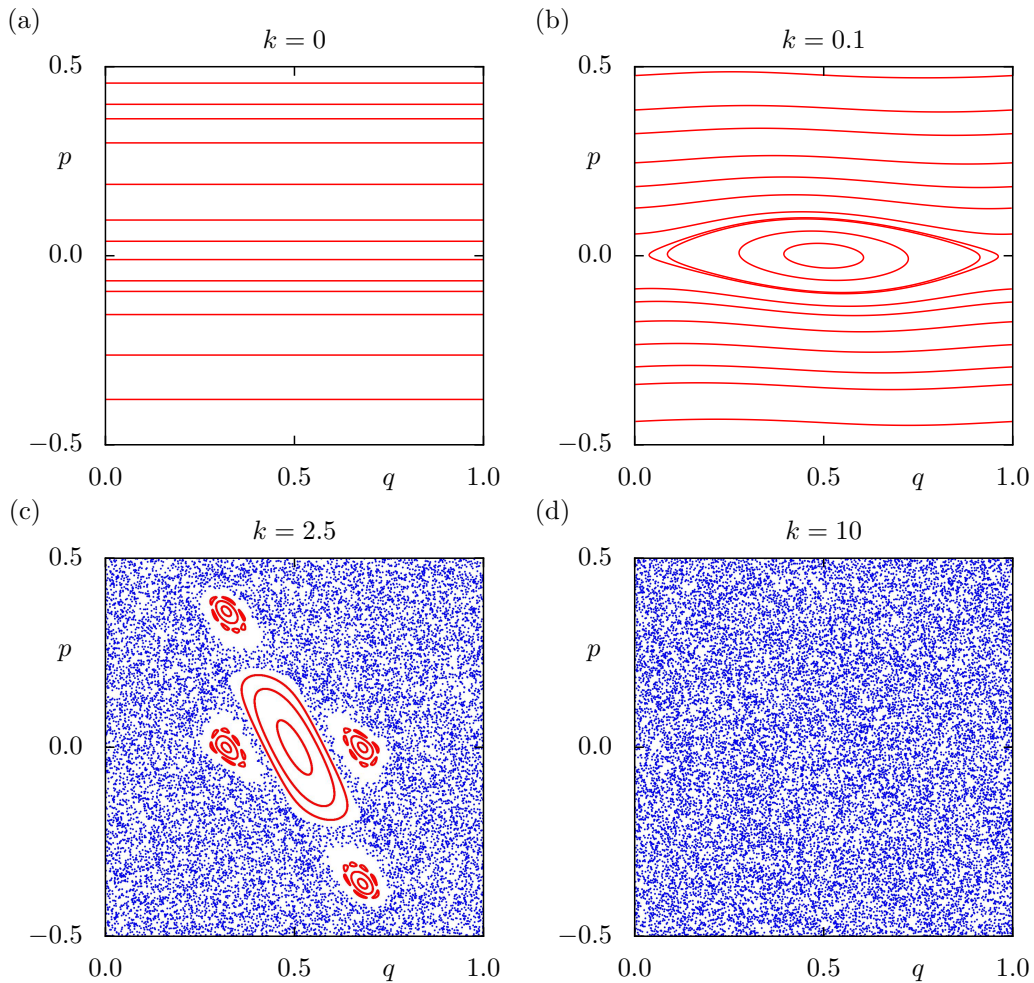


Figure 2.1: Orbits of the standard map for various kicking strength.

perturbations almost all tori persist and are deformed as stated by the KAM-theorem [36]. This is illustrated for $k = 0.1$ in (b). In the center at $q^s = 0.5, p^s = 0$ is a stable fix point and at $q^u = 0, p^u = 0$ one has an unstable fix point. For $k = 2.5$ (c) the mixed phase space structure is clearly visible with regular motion around stable fixed or periodic points and chaotic motion that fills whole phase space areas and forms the chaotic sea. Whereas there are no visible regular islands for $k = 10$ (d). The mapping defined with the standard map shows very rich and complicated structures with a mixed phase space, resonance chains, which influence the tunneling in the quantum mechanics [37–40], and partial barriers, which limit the classical transport [41–43].

To investigate the flooding effect in systems with a mixed phase space we want to study systems as simple as possible. Therefore we choose designed maps, which allow to control the various properties of the phase space structure at a much finer scale.

2.1.2 Designed kicked maps

For most of the investigations in this thesis we use designed kicked maps. They are constructed such that the phase space shows a large regular island without visible island chains in the transition region to the chaotic sea [21]. Although generally there are always small island chains we choose maps for which they are not relevant for the quantum mechanics in the considered h_{eff} -regime. The phase space in Fig. 2.2(a) shows the structure of one regular island, which is surrounded by the chaotic sea. The potential and kinetic energy are defined as

$$V(q) = -kb \left(\frac{k(q)}{2} + x(q) \right) - \frac{rx(q)^2}{2} \quad (2.11a)$$

$$T(p) = \begin{cases} \frac{sp}{4} - p + \frac{sp^2}{2} - \frac{s}{32} - \frac{a}{4} & (p \leq 0) \\ \frac{sp}{4} + ap - \frac{sp^2}{2} - \frac{s}{32} - \frac{a}{4} & (p > 0) \end{cases} . \quad (2.11b)$$

where s , r , a , and b are free parameters. To extend the potential to many unit-cells in phase space we use the cell index k and inter-cell position variable x as auxiliary variables

$$k(q) = \left\lfloor q + \frac{1}{2} \right\rfloor \quad (2.12a)$$

$$x(q) = q - k = q - \left\lfloor q + \frac{1}{2} \right\rfloor , \quad (2.12b)$$

where $\lfloor \cdot \rfloor$ is the integer part of a number. Both functions are continuous and the kinetic energy in the center of the regular island at $p = 0.25$ is set to zero. For the mapping the first derivative is needed

$$V'(q) = -rx(q) - bk(q) \quad (2.13a)$$

$$T'(p) = \begin{cases} sp + \frac{s}{4} - 1 & (p \leq 0) \\ -sp + \frac{s}{4} + a & (p > 0) \end{cases} . \quad (2.13b)$$

The phase space for three unit-cells in phase space is shown in Fig. 2.2(b). For analytic

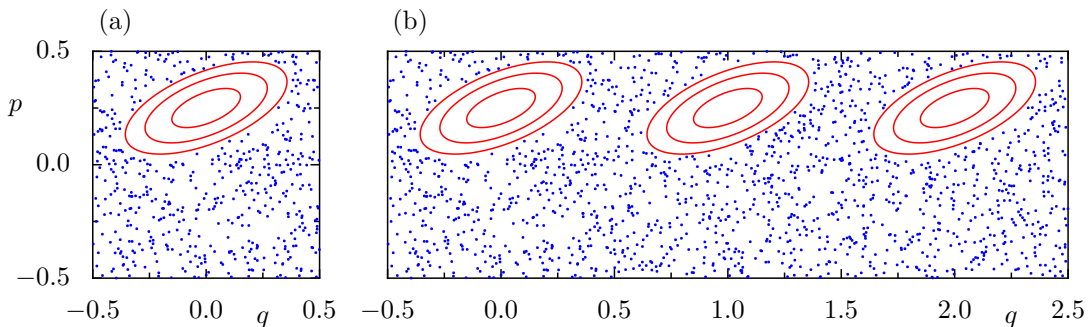


Figure 2.2: Classical phase space of the designed kicked map with one (a) and with three unit-cells (b) in phase space.

| parameter | \mathcal{M}_1 | \mathcal{M}_2 |
|-----------|-----------------|-----------------|
| s | 2 | 2 |
| r | 0.65 | 0.65 |
| a | 1 | 0 |
| b | 1 | 0 |

Table 2.1: Parameters used for the mappings \mathcal{M}_1 and \mathcal{M}_2 .

computations of tunneling rates and to control the transition region between regular and chaotic motion a smoothing of the discontinuous mapping with a Gaussian of width $\epsilon = 0.015$ is used. The resulting equations are shown in App. A.2. In this thesis we use two sets of parameters, which are listed in Tab. 2.1 and define the maps \mathcal{M}_1 and \mathcal{M}_2

$$\mathcal{M}_{1,2} : \quad \begin{aligned} q_{n+1} &= \left(q_n + T'(p_n) + \frac{1}{2} \right) \bmod M_q - \frac{1}{2} \\ p_{n+1} &= \left(p_n - V'(q_n + T'(p_n)) + \frac{1}{2} \right) \bmod 1 - \frac{1}{2} \end{aligned} \quad (2.14)$$

where M_q is the number of unit-cells in q -direction and the phase space is restricted to the torus $[-\frac{1}{2}, M_q - \frac{1}{2}] \times [-\frac{1}{2}, \frac{1}{2}]$. The functions for the potential and kinetic energy are visualized in Fig. 2.3. The average value of $T'(p)$ defines the transport behavior along the q -axis of the mapping. In the case of \mathcal{M}_1 the averaged $T'(p)$ is -1 in the lower part of the phase space with $p < 0$ and 1 in the upper part $p > 0$. This leads to transport of the regular islands to the right and in the chaotic sea the diffusive transport is biased to the left. The mapping of a phase space point inside the first regular island yields a point inside the second when $M_q > 1$. For \mathcal{M}_2 the upper part of the phase space and thus the regular island shows no transport. Thus each regular orbit is restricted to one of the M_q regular islands.

2.2 Quantized torus maps

We want to investigate the quantum mechanics of the systems introduced in the previous section. Several approaches on the quantization of area preserving maps can be found in Refs. [17, 44–47]. The periodic boundary conditions imply that the wave functions in position and momentum representation have to fulfill the Bloch condition

$$\langle q + M_q | \psi \rangle = e^{2\pi i \theta_q} \langle q | \psi \rangle \quad (2.15a)$$

$$\langle p + M_p | \psi \rangle = e^{-2\pi i \theta_p} \langle p | \psi \rangle \quad , \quad (2.15b)$$

where θ_q and θ_p are Bloch phases. The number of unit-cells M_p in p -direction is set to one for all cases considered in this thesis. We use the de-Broglie relation for plane waves with

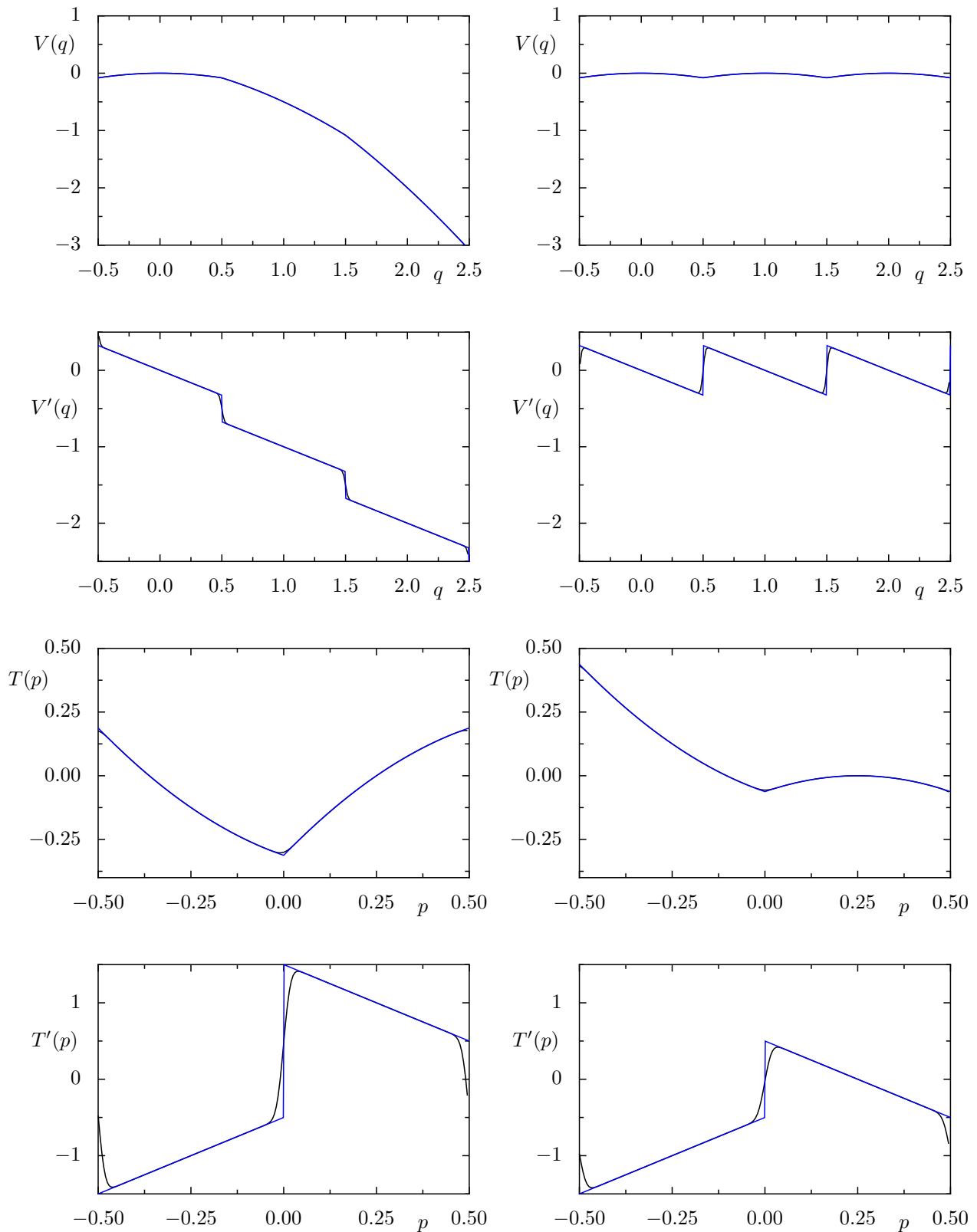


Figure 2.3: Potential and kinetic energy and their derivatives for the mappings \mathcal{M}_1 (left) and \mathcal{M}_2 (right). The discontinuous functions are plotted in blue in comparison to the Gaussian smoothed ones used for the quantum mechanics in black.

momentum p_l

$$p_l = \frac{h_{\text{eff}}}{\lambda} \quad (2.16)$$

where h_{eff} is the effective Planck constant, see App. A.1, and λ is the wave length. With Eq. (2.15) one obtains

$$e^{\frac{i}{h_{\text{eff}}} p_l q} \stackrel{(2.15)}{=} e^{\frac{i}{h_{\text{eff}}} p_l (q + M_q)} e^{-2\pi i \theta_q} \quad (2.17)$$

$$e^{2\pi i \frac{q}{\lambda}} = e^{2\pi i \frac{q + M_q}{\lambda}} e^{-2\pi i \theta_q} \quad (2.18)$$

$$= e^{2\pi i \frac{q}{\lambda}} e^{2\pi i \left(\frac{M_q}{\lambda} - \theta_q \right)} \quad (2.19)$$

a quantization condition for the wave length λ

$$\lambda = \frac{M_q}{l + \theta_q} , \quad (2.20)$$

where l is an integer number. Thus also the momentum is quantized

$$p_l = \frac{h_{\text{eff}}}{M_q} (l + \theta_q) . \quad (2.21)$$

Suppose the number of momentum values that fit in the interval $[-\frac{1}{2}, M_p - \frac{1}{2}]$ is N . Then the difference of neighboring discrete momentum values is

$$p_{l+1} - p_l = \frac{M_p}{N} . \quad (2.22)$$

The same difference evaluated using Eq. (2.21) gives

$$p_{l+1} - p_l = \frac{h_{\text{eff}}}{\frac{M_q}{l+1+\theta_q}} - \frac{h_{\text{eff}}}{\frac{M_q}{l+\theta_q}} = \frac{h_{\text{eff}}}{M_q} . \quad (2.23)$$

By comparison of Eqs. (2.22) and (2.23) we obtain a relation for the effective Planck constant

$$h_{\text{eff}} = \frac{M_q M_p}{N} . \quad (2.24)$$

The units of momentum and position fix the Hilbert space dimension N such that exactly N Planck cells cover the available phase space volume on the torus. With Eqs. (2.24) and (2.21) one obtains the possible values for p

$$p_n = M_p \frac{\theta_q + n_p^{(0)} + n}{N} \quad \text{with } n = 0, \dots, N - 1 , \quad (2.25)$$

where $n_p^{(0)}$ is used to shift the momentum lattice such that $p_{\min} = -0.5$. In a similar way we find for the position lattice

$$q_k = M_q \frac{\theta_p + n_q^{(0)} + k}{N} \quad \text{with } k = 0, \dots, N-1 . \quad (2.26)$$

The lattice shifts are computed as follows

$$n_q^{(0)} = \left[\frac{N}{M_q} q_{\min} - \theta_p \right] , \quad (2.27)$$

$$n_p^{(0)} = \left[\frac{N}{M_p} p_{\min} - \theta_q \right] , \quad (2.28)$$

where $[x]$ denotes the smallest integer larger or equal to x . For the maps \mathcal{M}_1 and \mathcal{M}_2 we choose the beginning of the lattice in analogy to the modulo operation for the classical mapping as $q_{\min} = -0.5$ and $p_{\min} = -0.5$.

2.2.1 Time evolution operator

The time evolution operator corresponds to the classical kicked map and one studies the eigenvalue equation of the time evolution operator

$$U |\psi_n\rangle = e^{2\pi i \varphi_n} |\psi_n\rangle , \quad (2.29)$$

where $|\psi_n\rangle$ are the eigenstates and φ_n the eigenphases of the time evolution operator U . It is evaluated over one period of the kicking just after the kick

$$U \equiv \lim_{\epsilon \searrow 0} U(t+1+\epsilon, t+\epsilon) . \quad (2.30)$$

This operator separates in two parts K and F

$$U = e^{-\frac{i}{\hbar_{\text{eff}}} V(q)} e^{-\frac{i}{\hbar_{\text{eff}}} T(p)} \equiv: K \circ F . \quad (2.31)$$

In order to fulfill periodic boundary conditions in the Eq. (2.15) the potential and kinetic energy functions $V(q)$ and $T(p)$ both have to be either strictly periodic or the Bloch phases are restricted by further conditions as will be discussed in the following section. The matrix representation of K is diagonal in position space

$$\langle q_k | K | q_l \rangle = e^{-\frac{i}{\hbar_{\text{eff}}} V(q_l)} \delta_{kl} \quad (2.32)$$

and F is diagonal in momentum representation

$$\langle p_k | F | p_l \rangle = e^{-\frac{i}{\hbar_{\text{eff}}} T(p_l)} \delta_{kl} . \quad (2.33)$$

In position representation F is given by

$$\langle q_k | F | q_l \rangle = \sum_{m,n} \langle q_k | p_m \rangle \langle p_m | F | p_n \rangle \langle p_n | q_l \rangle . \quad (2.34)$$

Using

$$\langle q_k | p_n \rangle = \frac{1}{\sqrt{N}} e^{\frac{i}{\hbar_{\text{eff}}} q_k p_n} , \quad (2.35)$$

one obtains with Eq. (2.25) and Eq. (2.26)

$$\langle q_k | F | q_l \rangle = \sum_m \langle q_k | p_m \rangle \langle p_m | q_l \rangle e^{-\frac{i}{\hbar_{\text{eff}}} T(p_m)} \quad (2.36)$$

$$= \frac{1}{N} \sum_m e^{\frac{2\pi i}{N} (\theta_q + n_p^{(0)} + m)(k-l)} e^{-\frac{i}{\hbar_{\text{eff}}} T(p_m)} . \quad (2.37)$$

This leads to $U = K \circ F$ in position representation

$$\langle q_k | K \circ F | q_l \rangle = \sum_m \langle q_k | K | q_m \rangle \langle q_m | F | q_l \rangle \quad (2.38)$$

$$= \frac{1}{N} e^{-i/\hbar_{\text{eff}} V(q_k)} \sum_m e^{\frac{2\pi i}{N} (\theta_q + n_p^{(0)} + m)(k-l)} e^{-\frac{i}{\hbar_{\text{eff}}} T(p_m)} . \quad (2.39)$$

Remarks on the numerical implementation of the time evolution of wave packets can be found in App. B.1.

2.2.2 Quasi-periodic potential and kinetic energy functions

As already mentioned the quantization on the torus relies strongly on the periodicity, which is given for example using a periodic Hamiltonian. However the kinetic energy of the standard map and the potential of the designed maps are not periodic, which can lead to discontinuities on the torus. They have a strong and unwanted influence on the quantum mechanical system.

For example for the standard map the kinetic energy is quadratic

$$T(p_n) = \frac{p_n^2}{2} . \quad (2.40)$$

Obviously this function is not periodic, though the part of the time evolution operator, which depends on T , the operator F , can be made periodic for certain lattices p_n . The diagonal matrix in momentum representation, Eq. (2.33), contains only exponential functions, which are

periodic if the argument is an integer multiple of 2π

$$\frac{2\pi i}{h_{\text{eff}}} T(p_n + M_p) = 2\pi i \left(\frac{1}{h_{\text{eff}}} T(p_n) + k \right) \quad \text{with } k \in \mathbb{Z} . \quad (2.41)$$

This condition is equivalent to

$$\frac{1}{h_{\text{eff}}} (T(p_n + M_p) - T(p_n)) = k \quad (2.42)$$

$$\stackrel{(2.40)}{=} \frac{1}{2h_{\text{eff}}} [(p_n + M_p)^2 - p_n^2] \quad (2.43)$$

$$= \frac{N}{2M_p} [2M_p p_n + M_p] \quad (2.44)$$

$$\stackrel{(2.25)}{=} \frac{N}{2M_p} \left[\frac{2M_p}{N} (\theta_q + n_p^{(0)} + n) + M_p \right] \quad (2.45)$$

$$= \frac{N}{2} + \theta_q + n_p^{(0)} + n . \quad (2.46)$$

The periodicity of F is valid if the resonance condition for θ_q is fulfilled

$$\theta_q = \frac{N}{2} \pmod{1} . \quad (2.47)$$

In a similar way we obtain a restriction for θ_p in the case of \mathcal{M}_1 by using the potential energy V and the operator K in position representation

$$\theta_p = \frac{N}{2} \pmod{1} . \quad (2.48)$$

Thus, the only Bloch phase to choose freely is θ_q for the map \mathcal{M}_1 and for the standard map it is θ_p .

2.3 Mushroom billiard

A billiard system is given by a freely moving point-like particle confined by hard wall boundaries $\partial\Omega$, which are perfectly reflecting, such that the angle of incidence equals the angle of reflection, see Fig. 2.4. Depending on the shape of the billiard one obtains integrable dynamics like in the rectangular, circular, and elliptical billiard [48] or ergodic motion like in the Sinai [49, 50] and the stadium billiard [51, 52]. The mushroom billiard [53] gives an example of a mixed system. It consists of a rectangular stem of length l and width a and a half circular cap with radius R . In Fig. 2.4 the shape of the boundary of the desymmetrized mushroom billiard is shown. Since the system has two degrees of freedom the phase space is four dimensional. The energy and thus the modulus of the momentum are conserved. Therefore we fix both quantities by demanding $|\vec{p}| = 1$, which restricts the dynamics to a three dimensional hyper-surface. In order to further

reduce the dimensionality we use the Birkhoff coordinates [54] (s, p_t) with the arc-length along the boundary s and the tangential momentum p_t at the moment when the particle is reflected on the blue wall in Fig. 2.4. One obtains a Poincaré section of the phase space, which contains almost all possible trajectories except a set of measure zero e.g. bouncing ball orbits in the stem. In Fig. 2.5(a) the structure of the Poincaré section is shown. The blue dots indicate a chaotic orbit and the motion extends over the whole mushroom area, see Fig. 2.5(c), whereas the motion in the regular part of the phase space, marked in red, is limited to the cap with conserved modulus of the angular momentum with respect to the center of the circle, shown in Fig. 2.5(b).

The quantum mechanics of the mushroom billiard is described by the time-independent Schrödinger equation in two dimensions

$$-\frac{\hbar^2}{2m} \left(\frac{\partial^2}{\partial x^2} + \frac{\partial^2}{\partial y^2} \right) \psi_n = E_n \psi_n \quad (2.49)$$

with Dirichlet boundary conditions, i.e. $\psi_n(x, y) = 0$ for $(x, y) \in \partial\Omega$. There is no analytic solution of this eigenvalue problem and we use for the numerical computation of wave functions the improved method of particular solutions [55, 56].

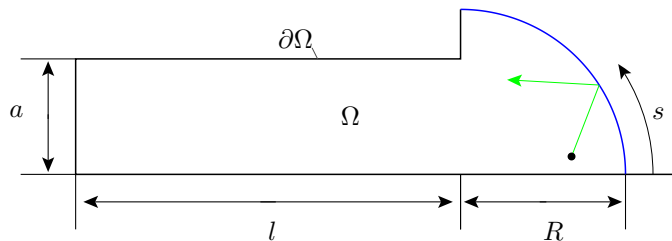


Figure 2.4: Desymmetrized mushroom billiard with stem length l , stem width a , and radius R . The arc length s is measured along the boundary starting at the corner to the right.

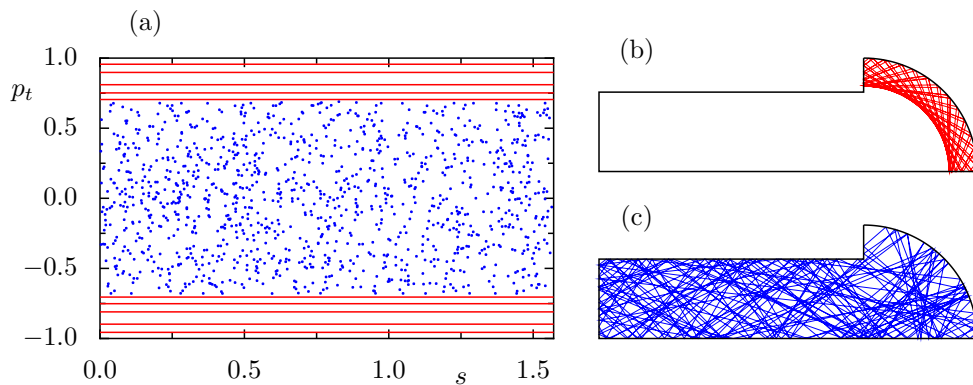


Figure 2.5: Phase space of the mushroom billiard in Birkhoff coordinates (a). Regular tori are marked in red and a chaotic orbit is shown in blue, whereas the corresponding trajectories are shown in position space (b) and (c).

3 Flooding of regular states

In this chapter we study the flooding of regular states. For this we mainly consider the time evolution of wave packets started in the chaotic sea for quantum maps, which leads to linearly increasing probability within the regular island in a first time regime, explained in Sec. 3.2. Afterwards the full time-dependent solution is modeled in Sec. 3.4. We also find adaptive solutions for the case of the standard map in Sec. 3.5 and show in Sec. 3.6 that the theoretical results are applicable to two dimensional billiards, particularly discussing the mushroom billiard here.

3.1 Numerical time evolution in quantum maps

The first class of systems for which we study the flooding phenomenon are quantum maps. The time evolution of wave packets gives an intuitive understanding of the nature of flooding. We analyze a sequence of wave functions $|\phi(n)\rangle$ generated by the iterative application of the time evolution operator

$$|\phi(n+1)\rangle = U |\phi(n)\rangle . \quad (3.1)$$

Remarks on the numerics of the time evolution can be found in App. B.1. The initial wave packet $|\phi(0)\rangle$ is chosen such that it is located in the chaotic sea. To measure the amount of flooding we use two different measures. The first is the probability in the regular part of the phase space expressed in terms of the Husimi function, see Sec. 3.1.1. A second measure is based on the projection of the time-evolved wave packet onto states localized within the regular island, see Sec. 3.1.2.

3.1.1 Husimi weight

Using the Husimi function [57] allows to study the probability of a wave function within the classical regular island as was demonstrated in Ref. [22]. To define the Husimi function, one starts with a coherent state $|\alpha(\tilde{q}_0, \tilde{p}_0)\rangle$, which is localized around the phase space point $(\tilde{q}_0, \tilde{p}_0)$ and embodies the minimal uncertainty of position and momentum width. The position repre-

sensation of a coherent state $|\alpha(\tilde{q}_0, \tilde{p}_0)\rangle$ respecting the periodic boundary conditions is

$$\alpha(q_n, \tilde{q}_0, \tilde{p}_0) = \left(\frac{2h_{\text{eff}} \Re c}{M_p^2} \right)^{\frac{1}{4}} \sum_{l=-\infty}^{\infty} \exp \left(-\frac{c}{2h_{\text{eff}}} (q_n - (\tilde{q}_0 + lM_q))^2 + i \frac{\tilde{p}_0 q_n}{h_{\text{eff}}} + 2\pi i \theta_q l \right) . \quad (3.2)$$

The Husimi function is then given by

$$\mathcal{H}_{|\phi\rangle}(\tilde{q}_0, \tilde{p}_0) = \frac{1}{h_{\text{eff}}} |\langle \alpha(\tilde{q}_0, \tilde{p}_0) | \phi \rangle|^2 . \quad (3.3)$$

Numerically this quantity is evaluated on an equidistant grid in phase space and the result is usually illustrated in a two dimensional color plot. Details on the implementation can be found in App. B.2.

We consider an eigenstate $|p_i\rangle$ of the momentum operator as initial state $|\phi(0)\rangle$

$$\langle p_i | \phi(0) \rangle = \delta_{ij} , \quad (3.4)$$

where p_j is chosen randomly in the chaotic sea $p_j \in [-0.4, -0.1]$. The Husimi function of the time-evolved wave packet $|\phi(t)\rangle$ is shown in Fig. 3.1 for the first time steps. By the use of the Husimi function $\mathcal{H}_{|\phi(t)\rangle}$ we define a regular weight $w(t)$ by integration over the classical regular part of the phase space

$$w(t) = \sum_{k=0}^{M_q-1} \int_{I_k} \mathcal{H}_{|\phi(t)\rangle}(q, p) dq dp . \quad (3.5)$$

The boundary of the integration area I_k is determined by a regular torus at the border of regular island in the corresponding classical map around the fixed point $(q_c, p_c) = (k, 0.25)$ in the k -th unit-cell. Since the Husimi function resembles the Heisenberg uncertainty relation it is not necessary to determine this border with a very high accuracy if we restrict our numerical experiments to parameters not far in the semi-classical limit ($h_{\text{eff}} \geq \frac{1}{50}$). In Fig. 3.2(a) the weight $w(t)$ is shown on a logarithmic timescale for the time evolution of the same wave packet $|\phi\rangle$ that is shown in Fig. 3.1. The different curves are computed with varying numbers of unit-

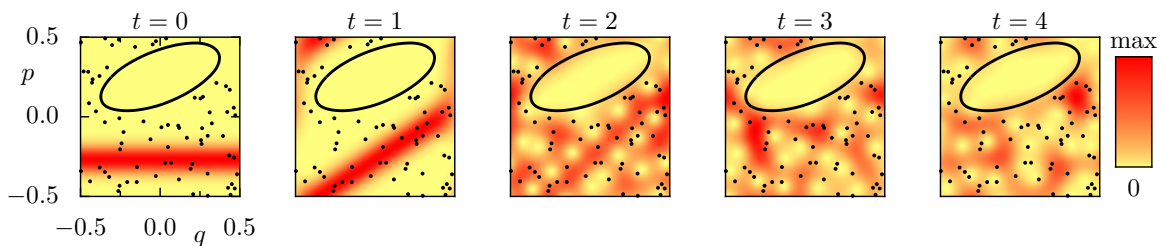


Figure 3.1: A wave packet is started in the chaotic sea for $t = 0$. The Husimi function of the wave packet is shown together with the classical phase space structure. High probability is marked in red whereas low probability corresponds to yellow.

cells M_q and the area of the Planck cell h_{eff} is fixed at $\frac{1}{30}$. In all cases $w(t)$ increases with time until a saturation plateau is reached. However, especially for $M_q = 1$ the weight $w(t)$ is strongly fluctuating, whereas for $M_q = 1597$ the integration area in Eq. (3.5) is much larger and thus the amplitude of the fluctuations is small. The final probability distribution in phase space is shown in the insets on the right hand side. For the cases where $M_q \neq 1$ the Husimi functions of every unit-cell is computed separately and the result is averaged. To reduce the fluctuations we use an additional average over Bloch phases θ_q . For each value of θ_q the time evolution is evaluated and the Husimi weight is computed. With respect to the different integration areas we use much more Bloch phase values for $M_q = 1$ than for $M_q = 1597$ as is listed in Tab. 3.1. The results are shown in the graph of Fig. 3.2(b) and the two different regimes of increasing weight and saturation plateaus are clearly visible in all cases. The Husimi functions in the inset show, that a higher saturation plateau for larger M_q corresponds to an effectively smaller regular island, because the wave packet extends uniformly over the chaotic sea and a part of the regular island, which grows with increasing M_q . The regular island is flooded for large numbers of unit-cells M_q in phase space. In the following we are going to find a quantitative description in dependence of the parameters M_q and h_{eff} .

3.1.2 Projection onto regular states

As a second measure for the flooding of regular islands we use the projection onto regular states. As discussed in the introduction the semi-classical eigenfunction hypothesis [8–10] states that eigenfunctions are either chaotic or regular in the semi-classical limit. For finite h_{eff} Fig. 3.3 shows the Husimi functions of some eigenfunctions of the kicked map \mathcal{M}_1 . The left one is a typical example of a chaotic state whereas the following sequence is concentrated mostly on classical regular tori. They are ordered with respect to the area those tori enclose and labeled by the quantum number m . The outer tori with $m = 4$ and $m = 5$ show already significant probability in the chaotic part of phase space. Thus they are neither purely regular nor purely chaotic. To characterize the eigenfunctions of such a system quantitatively we want to compare them to purely regular states. These are eigenstates of a system, which does not contain regular to chaotic coupling. It was shown for example in Ref. [58] that purely regular states

| M_q | number of Bloch phases θ_q for average |
|-------|---|
| 1 | 20000 |
| 13 | 2000 |
| 144 | 200 |
| 1597 | 20 |

Table 3.1: The number of Bloch phase averages used for the realizations of the quantum map \mathcal{M}_1 for the different values of M_q .

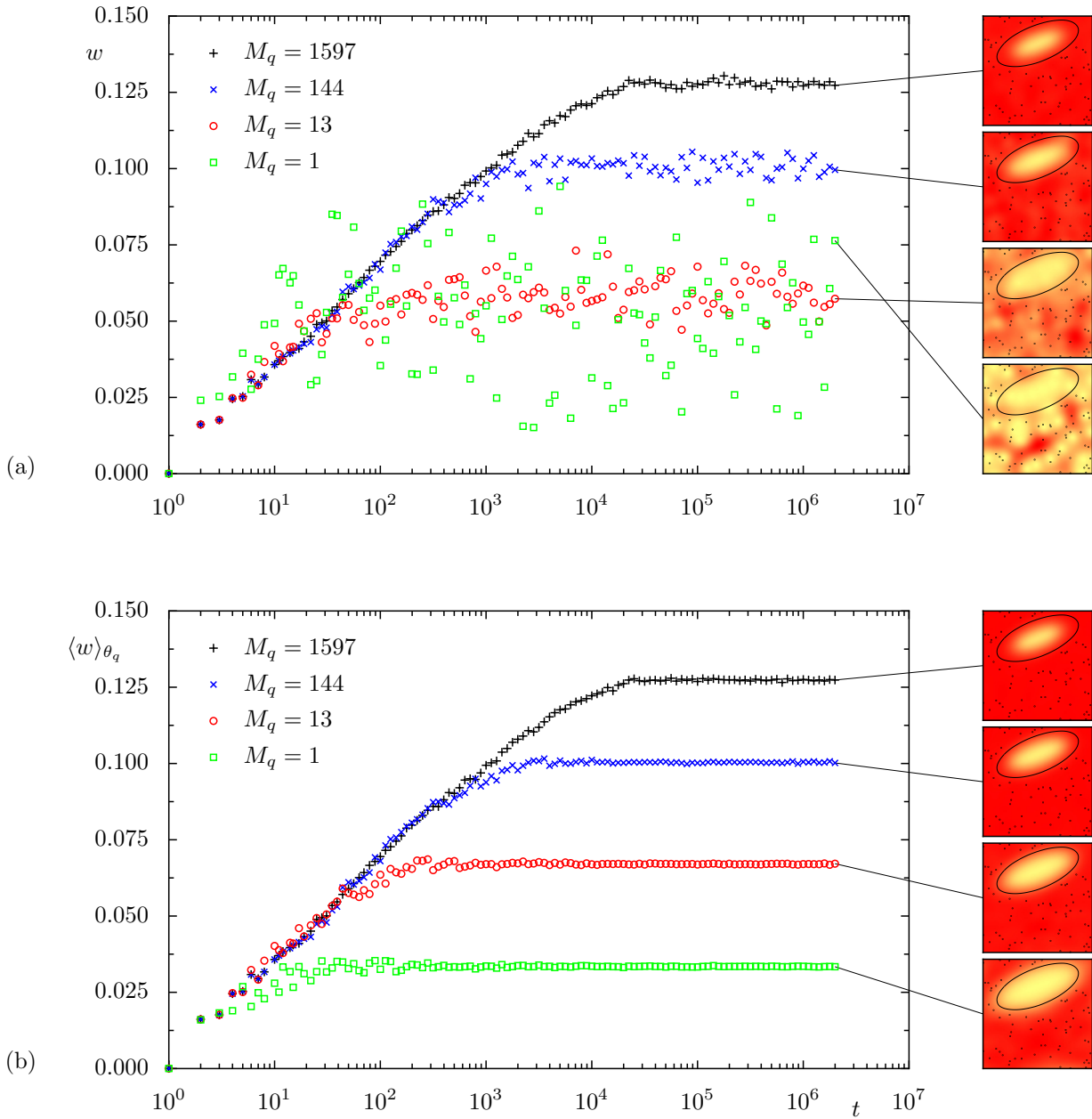


Figure 3.2: Time-dependent Husimi weight $w(t)$ inside the classical regular island for a wave packet which initially is a momentum eigenstate at $p = -0.25$ (a). The number M_q of unit cells in q -direction is varied, while the effective Planck constant is fixed at $h_{\text{eff}} \approx \frac{1}{30}$. The averaged Husimi weight $\langle w \rangle_{\theta_q}$ is shown in (b).

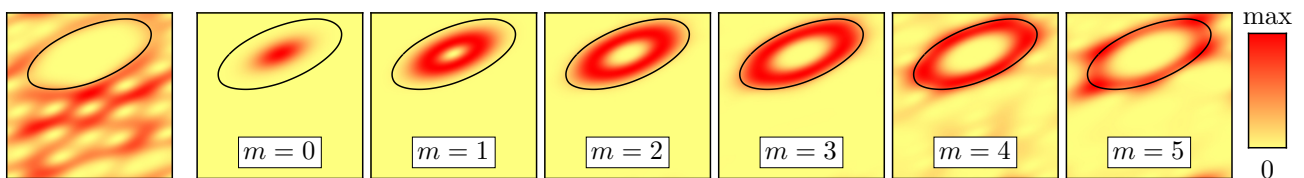


Figure 3.3: Eigenfunctions of the quantum map \mathcal{M}_1 . The left picture shows a typical chaotic state. The following sequence are eigenstates that live mostly on classical regular tori. They are sorted by the quantum number m .

can be constructed as eigenstates of a fictitious integrable system. These states fulfill the WKB quantization rule

$$A_m = \oint_{\mathcal{C}_m} p \, dq = \left(m + \frac{1}{2}\right) h_{\text{eff}} . \quad (3.6)$$

Each state concentrates along a classical regular torus \mathcal{C}_m that encloses the area A_m . For the designed maps $\mathcal{M}_{1,2}$ with $M_q = 1$ due to their elliptical island an analytic expression was found for the regular states. The eigenfunctions of the fictitious integrable system are harmonic oscillator states that are squeezed in p -direction, rotated around the origin, and shifted to $q = 0, p = 0.25$. Neglecting the periodic boundary conditions on torus their position representation is given by [23]

$$\begin{aligned} \langle q | \chi_{\text{reg},m,k} \rangle &= \sqrt{\frac{M_q}{2^m m! N}} \left(\frac{\Re c}{\pi h_{\text{eff}}}\right)^{1/4} H_m \left(\sqrt{\frac{\Re c}{h_{\text{eff}}}}(q - k)\right) \\ &\times \exp\left(-\frac{c}{2h_{\text{eff}}}(q - k)^2 + \frac{i}{4h_{\text{eff}}}(q - k/2)\right) . \end{aligned} \quad (3.7)$$

This result depends on the quantum number m and the index k of the unit cell in phase space. The function H_m is the m -th Hermite polynomial and the complex tilting factor c describes the orientation of the ellipse that can be derived from the linearized map. The numerical value of c is given for the designed maps $\mathcal{M}_{1,2}$ by $c = (\sqrt{351} - 13i)/40$ [23]. Although the $|\chi_{\text{reg},m,k}\rangle$ are constructed for $M_q = 1$, the index k allows for purely regular states in every unit-cell in phase space. By construction those states form an orthogonal basis

$$\langle \chi_{\text{reg},m,k} | \chi_{\text{reg},n,k} \rangle = \delta_{mn} \quad (3.8)$$

with the exception of quasi modes centered in different unit-cells k and l . But the overlap $\langle \chi_{\text{reg},m,k} | \chi_{\text{reg},m,l} \rangle$ is exponentially small as long as we only consider states that live inside the regular island

$$\langle \chi_{\text{reg},m,k} | \chi_{\text{reg},n,l} \rangle \approx 0 \quad k \neq l, \quad n, m < m_{\text{max}} . \quad (3.9)$$

The number of regular states m_{max} in each island is given by the island area A_{reg} and Eq. (3.6)

$$A_{\text{reg}} \geq \left(m + \frac{1}{2}\right) h_{\text{eff}} \quad (3.10)$$

Such that

$$\Rightarrow m_{\text{max}} = \left\lfloor \frac{A_{\text{reg}}}{h_{\text{eff}}} - \frac{1}{2} \right\rfloor + 1 . \quad (3.11)$$

We find for the maps $\mathcal{M}_{1,2}$ numerically that $A_{\text{reg}} \approx 0.2126$. The Husimi functions of all regular states $m = 0, \dots, m_{\text{max}} - 1$ for $h_{\text{eff}} = \frac{1}{30}$ and $M_q = 1$ are shown in Fig. 3.4. These states form an orthogonal subspace in the Hilbert space of the system and we study the occupation

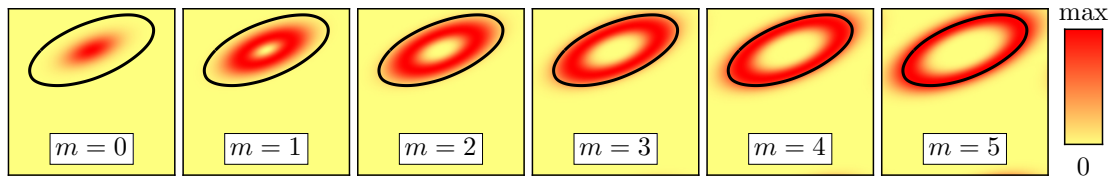


Figure 3.4: Husimi representation of semi-classically constructed regular states. Those states fulfill the WKB quantization rule with the quantum numbers m . The number of states is limited by the area inside the classical regular island.

probability $p_m^{\text{reg}}(t)$ in every regular state by

$$p_m^{\text{reg}}(t) = \sum_{k=0}^{M_q-1} \left| \langle \chi_{\text{reg},m,k} | \phi(t) \rangle \right|^2 . \quad (3.12)$$

Note, that the sum runs over all unit-cells in phase space. Without transport from one island to another (\mathcal{M}_2) regular states in different unit-cells are independent and the $|\chi_{\text{reg},m,k}\rangle$ are a good approximation for the purely regular states even for $M_q \neq 1$. But due to the classical hopping in the island chain for \mathcal{M}_1 the M_q purely regular states with quantum number m extend over all cells. As long as the M_q states $|\chi_{\text{reg},m,k}\rangle$ with constant m in different cells are non-overlapping they form a basis in the same subspace as the regular states with the same quantum number. For the quantum maps $\mathcal{M}_{1,2}$ the relevant properties, given by the tunneling rates and the Heisenberg time, are equal for all regular states with constant quantum number m . Thus the summation represents an average in the M_q -dimensional subspace.

In Fig. 3.5 the probability p_m^{reg} of the regular torus $m = 1$ is shown. Since the wave packet is started in the chaotic sea all regular probabilities are zero at $t = 0$ and we observe Rabi oscillations for $t > 0$. In the following we are interested in the long-time behavior and therefore the data is also shown on logarithmic scale where the initial quadratic increase and the averaged regular probability is pronounced. Under variation of the Bloch phase θ_q the amplitude and frequency of the Rabi oscillations change drastically, because p_m^{reg} is very sensitive to spectral fluctuations especially if there is only one unit-cell and no averaging. A discussion of numerical errors for the regular weights is presented in App. B.3.

In order to understand the fluctuations we investigate the spectrum of eigenphases φ , that are shown in Fig 3.6(a) as a function of the Bloch phase θ_q . One observes many phases θ_q where the eigenphases of regular states with negative slope seem to cross with the eigenphases of chaotic states, which show mostly positive slope. These different slopes are caused by the underlying transport of the classical mapping [17, 59]. A magnification in (b) reveals that the regular and chaotic states actually perform a so-called avoided crossing due to the tunneling coupling of these states. Away from the center of the avoided crossing, see the insets on the left or right hand side, one of the two corresponding eigenfunctions is very close to a purely regular state, while the other eigenfunction is chaotic. At the center both eigenfunctions show

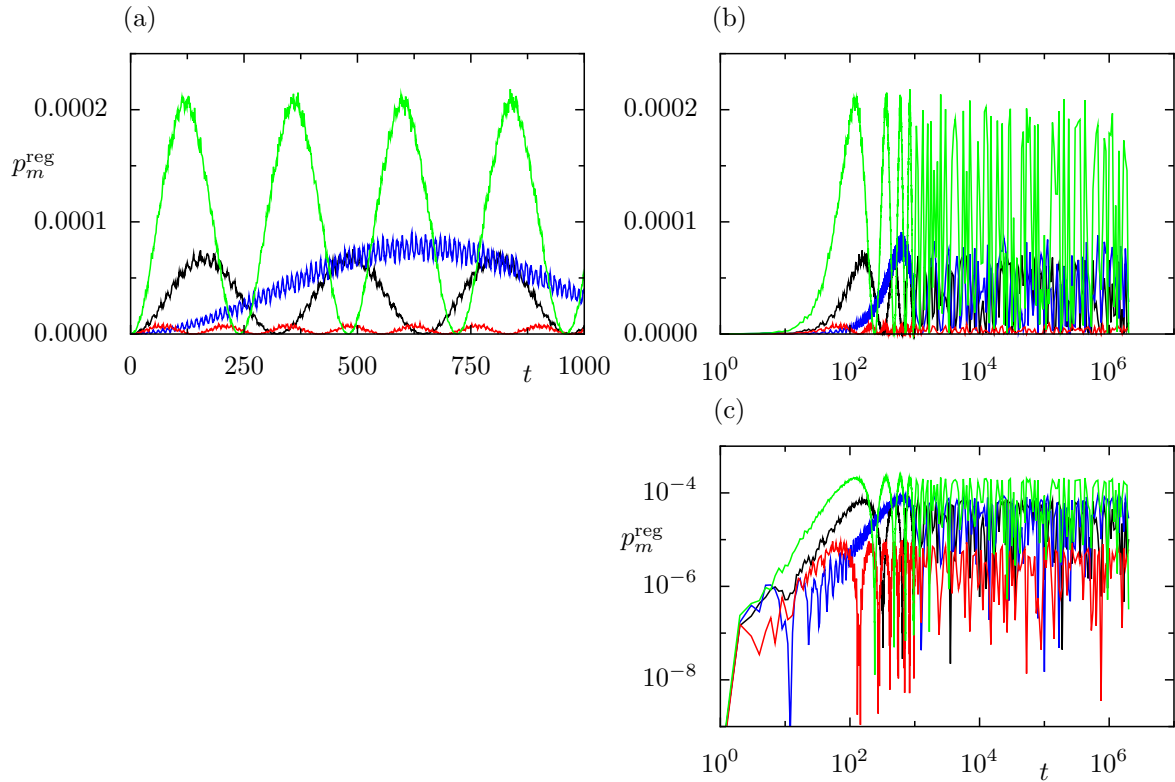


Figure 3.5: Occupation probability p_m^{reg} on the regular torus $m = 1$ (a). The phase θ_q was varied ($\theta_q = 0$ black, $\theta_q = 0.15$ blue, $\theta_q = 0.8$ red, $\theta_q = 0.95$ green). There are $N = 30$ states in the system and only $M_q = 1$ unit-cell in phase space. The same data is shown with a logarithmic time axis (b), and in a double log-plot (c).

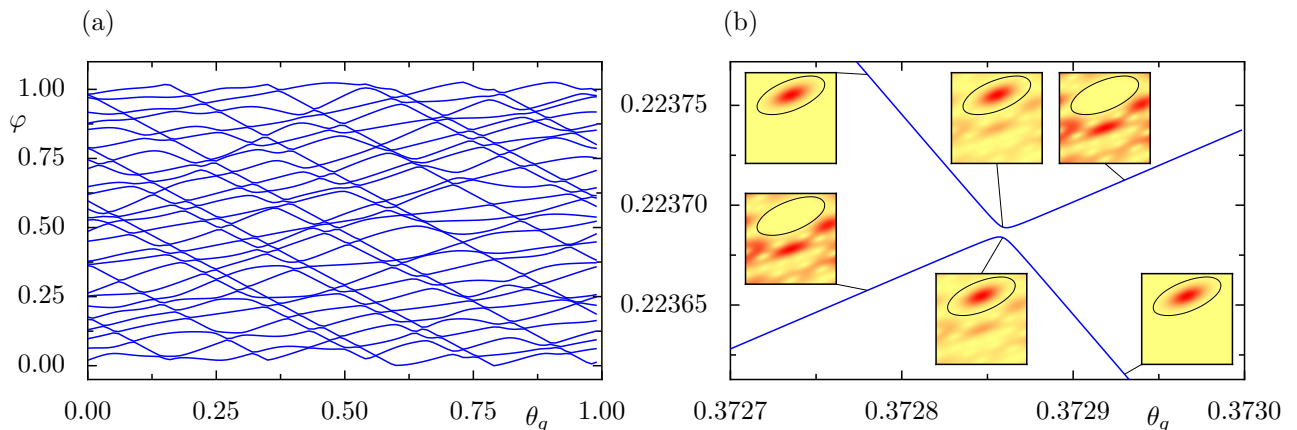


Figure 3.6: Spectrum of eigenphases φ of the quantum map \mathcal{M}_1 with $N = 30$ and $M_q = 1$ under variation of the Bloch phase θ_q . The straight lines with negative slope mark the position of regular states. A magnification of a very small avoided crossing is shown in (b). Additionally the Husimi functions of the corresponding eigenfunctions are shown as insets.

a mixing of chaotic and regular components, as the insets in the middle illustrate. For strong regular to chaotic coupling the avoided crossing is extended and we find such a strong mixing of both components for most of the Bloch phases θ_q . Also for small couplings the amplitude of the oscillation of $p_m^{\text{reg}}(t)$ is very large for θ_q -values in the narrow region of the avoided crossing.

The oscillation frequency depends on the width of the level splitting.

We use the average over many phases θ_q

$$\overline{p_m^{\text{reg}}} = \langle p_m^{\text{reg}} \rangle_{\theta_q} \quad (3.13)$$

to get information about the average flooding for each regular torus. At small times the oscillations are in phase and highly correlated, because we start with $p_m^{\text{reg}}(t=0) \approx 0$. Whereas for large times the correlations are lost due to different frequencies and only the mean value of the oscillations are important. The resulting graph in Fig 3.7 shows on a logarithmic timescale that the initial increase is preserved and that a plateau is obtained at large times due to the averaging. In between one observes a transition regime with oscillations, which are strongly damped with increasing t . As one would expect, the tori closer to the chaotic sea are flooded earlier and more strongly than the tori in the center of the island. The probability that is initially only in the chaotic sea distributes with time over all regular states in different amounts. Due to probability conservation the p_m^{reg} of one regular state cannot be independent from all others. The flooding of one regular state decreases the probability in the chaotic sea and therefore leads to smaller values of p_m^{reg} for other tori. To get a measure which compensates this effect we define the flooding value f by

$$f_m(t) = \frac{N_{\text{ch}} + M_q}{M_q} \frac{\overline{p_m^{\text{reg}}}}{1 - \sum_{i=0, i \neq m}^{m_{\text{max}}-1} p_i^{\text{reg}}} . \quad (3.14)$$

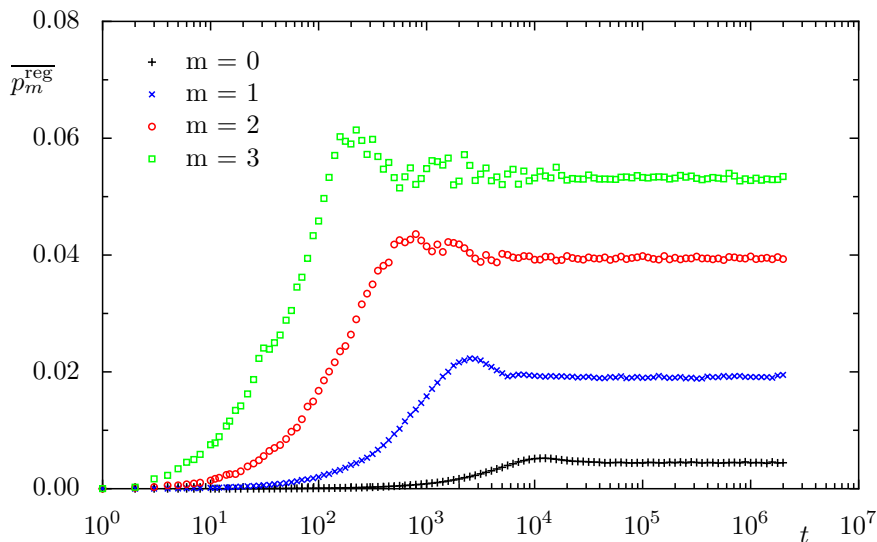


Figure 3.7: The averaged regular weights for a wave packet started in the chaotic sea using the map \mathcal{M}_1 with $M_q = 144$ unit-cells and $N = 2825$. The outer regular states are flooded faster and reach a higher saturation plateau than the inner ones.

The additional factor $\frac{N_{\text{ch}}+M_q}{M_q}$ ensures a flooding value $f = 1$ for a uniform distribution of probability over all states. This is obtained for the case of complete flooding, for which the regular probability is $\overline{p_m^{\text{reg}}} = \frac{M_q}{N_{\text{ch}}+M_q}$ because there are M_q regular states on the m -th torus and since we can disregard the other regular states. Due to the renormalization the total number of states is $N_{\text{ch}} + M_q$. This allows to treat exclusively one regular torus even for large regular islands, that contain many regular states. The influence of the renormalization is usually very small for weakly flooded systems with many chaotic states. Fig. 3.8 shows the same data as Fig. 3.7 renormalized and rescaled according to Eq. (3.14). We find that the outermost torus is almost completely flooded with $f(t)$ being close to one at large times. The second graph shows the same data on a double-logarithmic scale and we observe a linear slope at small times, which

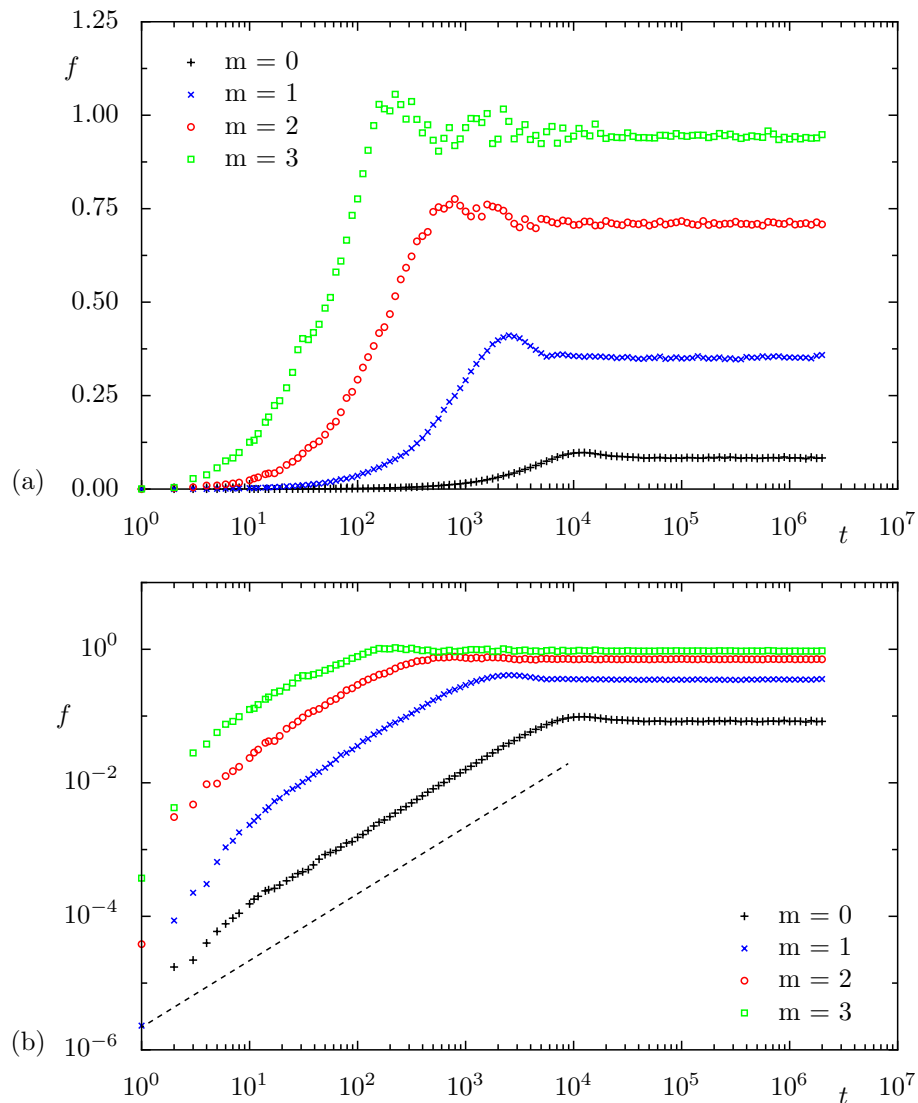


Figure 3.8: The flooding values for a wave packet stated in the chaotic sea using the map \mathcal{M}_1 with $M_q = 144$ unit-cells and $N = 2825$. Both graphs show the same data: in a semilogarithmic plot (a) and in a double-logarithmic plot (b). As a guide to the eye a linear slope of the form $f = \text{const} \cdot t$ is shown (dashed black line).

indicates a linear increase with time as is shown by the dashed black curve in comparison. In the following sections we will discuss the two regimes of the linear increase and the saturation regime in more detail. In Sec. 3.4 we introduce a simple matrix model which allows to understand the height of the saturation plateaus and qualitatively the transient behavior from the linear to the saturation regime.

3.2 Dynamical tunneling

The tunneling phenomenon is one of the fundamental quantum properties. If there are two potential wells separated by a barrier a wave packet passes through the barrier from one well to the other. This process is characterized by a timescale which is the inverse of the tunneling rate and depends on the shape of the barrier. Although there is no potential barrier between the regular and chaotic part of the mixed phase space, one finds tunneling through this dynamical barrier. For kicked maps the tunneling rates can be predicted analytically as described in Refs. [58–60] or numerically, see Ref. [61]. Although the analytic results agree in general very well with the numerical tunneling rates, occasionally there are errors up to a factor of two. Due to the large impact of such an error on flooding we use the numerical results for the tunneling rates whenever possible. We find that the linear regime (Sec. 3.2.1) of the flooding values is governed by the tunneling process and in Sec. 3.2.2 we will see that tunneling alone is sufficient to describe the the process of complete flooding.

3.2.1 Linear regime

We now want to study the linear flooding regime using the tunneling rates. Therefore we have to distinguish between tunneling in systems with a discrete spectrum where we usually observe Rabi-oscillations and systems with a continuous spectrum with an exponential decay. In the latter case Fermi's golden rule relates the tunneling rates with the coupling matrix elements $V_{\text{reg,ch}}$ of the involved states [62]

$$\gamma_m^{\text{reg} \rightarrow \text{ch}} = \frac{1}{h_{\text{eff}}} \langle V_{\text{reg,ch}}^2 \rangle \rho_{\text{ch}} \quad , \quad (3.15)$$

where ρ_{ch} is the density of chaotic states ρ_{ch} . Although we consider systems with a finite Hilbert-space dimension and thus discrete spectra, we will see that to some extent the decay rate can be described by Fermi's golden rule. In Sec. 3.3.3 a derivation of the same formula is given for a two-by-two matrix model where the average over many Rabi-oscillations leads to a linear increase. For now we will use Fermi's golden rule to relate the tunneling rates with the density of states and the coupling matrix elements. Due to the symmetry of the matrix element $\langle V_{\text{reg,ch}}^2 \rangle = \langle V_{\text{ch,reg}}^2 \rangle$ in Eq. (3.15) the opposite tunneling direction can also be expressed using Fermi's golden rule. It is almost the same compared to Eq. (3.15) except that the density of

states is that of the regular states

$$\gamma_m^{\text{ch} \rightarrow \text{reg}} = \frac{1}{h_{\text{eff}}} \langle V_{\text{reg, ch}}^2 \rangle \rho_{\text{reg}} . \quad (3.16)$$

Using both Eqs. (3.15) and (3.16) one obtains the tunneling rate from the chaotic sea to the regular island

$$\gamma_m^{\text{ch} \rightarrow \text{reg}} = \gamma_m^{\text{reg} \rightarrow \text{ch}} \frac{\rho_{\text{reg}}^m}{\rho_{\text{ch}}} = \gamma_m^{\text{reg} \rightarrow \text{ch}} \frac{M_q}{N_{\text{ch}}} . \quad (3.17)$$

The regular-to-chaotic tunneling rates are determined numerically and we use Eq. (3.17) to compute the tunneling rate for the opposite direction. The decay of a chaotic wave packet into the different regular states is given for $t = 0$ by the first derivative

$$\left. \frac{d}{dt} \overline{p_m^{\text{reg}}}(t) \right|_{t=0} = \gamma_m^{\text{ch} \rightarrow \text{reg}} . \quad (3.18)$$

Thus we obtain at small times the approximation for the regular weights

$$\overline{p_m^{\text{reg}}}(t) \approx \gamma_m^{\text{ch} \rightarrow \text{reg}} t \quad (3.19)$$

$$\approx \frac{M_q}{N_{\text{ch}}} \gamma_m^{\text{reg} \rightarrow \text{ch}} t \quad (3.20)$$

and the flooding values

$$f_m(t) \approx \frac{N_{\text{ch}} + M_q}{M_q} \gamma_m^{\text{ch} \rightarrow \text{reg}} t \quad (3.21)$$

$$\approx \frac{N_{\text{ch}} + M_q}{N_{\text{ch}}} \gamma_m^{\text{reg} \rightarrow \text{ch}} t . \quad (3.22)$$

In Fig. 3.9 we see that this linear approximation is valid for unexpectedly long times. A heuristic explanation for the applicability of Fermi's golden rule is given by the energy time uncertainty relation

$$\Delta E \Delta t \geq h_{\text{eff}} . \quad (3.23)$$

The system cannot resolve the mean energy level spacing in the chaotic sea Δ_{ch} before the Heisenberg time $\tau_{\text{H, ch}}$

$$\tau_{\text{H, ch}} = \frac{h_{\text{eff}}}{\Delta_{\text{ch}}} . \quad (3.24)$$

Thus one observes the decay of the system roughly up to the Heisenberg time $\tau_{\text{H, ch}}$, which is marked by the dotted line in Fig. 3.9. If the discreteness of the spectrum is resolved, the regular torus is either completely flooded with flooding value almost one or a plateau lower than one is formed. This argumentation is strongly related to existence criterion for regular states derived in Ref. [63]

$$\gamma_m^{\text{reg} \rightarrow \text{ch}} < \frac{1}{\tau_{\text{H, ch}}} . \quad (3.25)$$

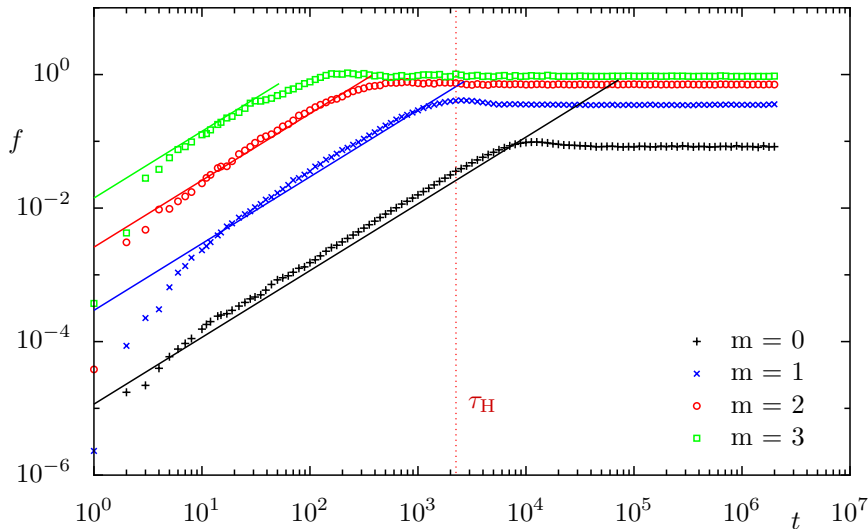


Figure 3.9: Flooding values (the same data as shown in Fig. 3.8) in double-logarithmic plot with the approximation of Eq. (3.22) as solid lines. The dotted line marks the Heisenberg time $\tau_{H,\text{ch}}$.

This criterion can be rephrased in terms of the tunneling time τ_t

$$\tau_t = \frac{1}{\gamma_m^{\text{reg} \rightarrow \text{ch}}} . \quad (3.26)$$

The flooding value derived from the linear approximation at the time $t = \tau_t$ is roughly one

$$f_{\text{linear}}(\tau_t) \stackrel{(3.22)}{=} \frac{N_{\text{ch}} + M_q}{N_{\text{ch}}} \approx 1 . \quad (3.27)$$

Thus the tunneling time yields the time a regular state needs to flood completely. But once the Heisenberg time has passed the tunneling stops and Eq. (3.22) is no longer valid. A regular state only exists if it is not flooded, which is the case when the tunneling time is larger than the Heisenberg time

$$\tau_t > \tau_{H,\text{ch}} \quad (3.28)$$

such that the linear increase stops with a flooding value smaller than one. This is a qualitative characterization and not at all quantitative as can be seen in Fig. 3.9 in which the Heisenberg time is marked by the dashed line. The tunneling time for $m = 3$ is very short and therefore the value of the plateau is one, whereas for $m = 0$ the Heisenberg time is much smaller than the tunneling time and the flooding values remain small for all times. This existence criterion is a very simple way to estimate the relevance of flooding in a system.

3.2.2 Complete flooding

Up to now we considered the tunneling from the chaotic sea to the regular island. This is sufficient to describe the short time behavior if the regular weights are small and thus almost all probability of the wave packet is still in the chaotic sea. For larger times the opposite tunneling direction becomes important, because the probability in the regular island is larger. We formulate a master equation, which models both tunneling directions and consider several regular states and one chaotic reservoir containing all chaotic states

$$\frac{d}{dt} \overline{p_m^{\text{reg}}}(t) = \gamma_m^{\text{ch} \rightarrow \text{reg}} \overline{p^{\text{ch}}}(t) - \gamma_m^{\text{reg} \rightarrow \text{ch}} \overline{p_m^{\text{reg}}}(t) \quad (3.29)$$

$$\frac{d}{dt} \overline{p^{\text{ch}}}(t) = \sum_m \left(\gamma_m^{\text{reg} \rightarrow \text{ch}} \overline{p_m^{\text{reg}}}(t) - \gamma_m^{\text{ch} \rightarrow \text{reg}} \overline{p^{\text{ch}}}(t) \right) , \quad (3.30)$$

where $\overline{p^{\text{ch}}}$ stands for the probability in the chaotic sea. We assume that all probabilities $\overline{p_m^{\text{reg}}}$ and $\overline{p^{\text{ch}}}$ are independent. This leads to the relation

$$p^{\text{ch}} + \sum_m p_m^{\text{reg}} = 1 \quad (3.31)$$

as the probability to find the wave packet somewhere in the whole phase space is one. We rephrase Eq. (3.30) in matrix notation

$$\frac{d}{dt} \begin{pmatrix} p_0^{\text{reg}}(t) \\ \vdots \\ p_{m_{\text{max}}}^{\text{reg}}(t) \\ p^{\text{ch}}(t) \end{pmatrix} = A \begin{pmatrix} p_0^{\text{reg}}(0) \\ \vdots \\ p_{m_{\text{max}}}^{\text{reg}}(0) \\ p^{\text{ch}}(0) \end{pmatrix} \quad (3.32)$$

with

$$A = \begin{pmatrix} -\gamma_0^{\text{reg} \rightarrow \text{ch}} & & 0 & \gamma_0^{\text{ch} \rightarrow \text{reg}} \\ & \ddots & & \vdots \\ 0 & & -\gamma_{m_{\text{max}}}^{\text{reg} \rightarrow \text{ch}} & \gamma_{m_{\text{max}}}^{\text{ch} \rightarrow \text{reg}} \\ \gamma_0^{\text{reg} \rightarrow \text{ch}} & \dots & \gamma_{m_{\text{max}}}^{\text{reg} \rightarrow \text{ch}} & -\sum_m \gamma_m^{\text{ch} \rightarrow \text{reg}} \end{pmatrix} . \quad (3.33)$$

The solution of this system is given by

$$\begin{pmatrix} p_0^{\text{reg}}(t) \\ \vdots \\ p_{m_{\text{max}}}^{\text{reg}}(t) \\ p^{\text{ch}}(t) \end{pmatrix} = \exp(At) \begin{pmatrix} p_0^{\text{reg}}(0) \\ \vdots \\ p_{m_{\text{max}}}^{\text{reg}}(0) \\ p^{\text{ch}}(0) \end{pmatrix} , \quad (3.34)$$

which can be evaluated numerically using either routines to solve linear differential equations (Eq. (3.30)), evaluating the exponential in Eq. (3.34) by Padé approximation, or by diagonal-

ization of the matrix A . The result is shown in the upper graph of Fig. 3.10 as solid lines compared to the numerical time evolution data.

The same type of rate equations can be obtained for the flooding values. Instead of one set of differential equations for all quantities $f_m(t)$ we use one independent set for every regular torus. Due to the rescaling and renormalization in Eq. (3.14) we cannot interpret $f_m(t)$ as a probability. We use a model of two reservoirs, the m -th regular torus $f_m(t)$ and the chaotic sea $f_{ch_m}(t)$. We also use the index m for the chaotic sea to indicate that there is a different chaotic reservoir for different regular tori, because of the renormalization in Eq. (3.14). As the flooding values are rescaled probabilities, it is ensured, that the sum of the flooding values is constant

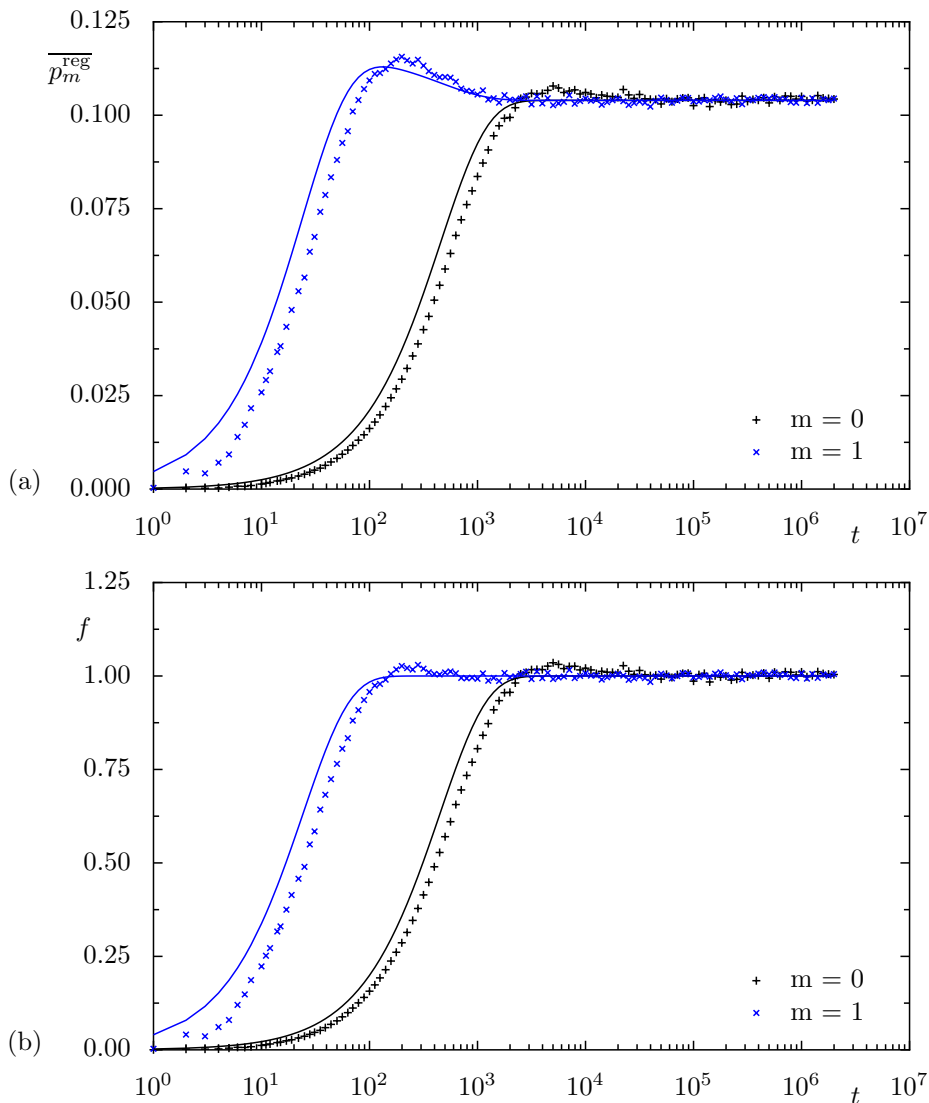


Figure 3.10: Regular weights of a completely flooded system (kicked map \mathcal{M}_1 with $N = 170345, M_q = 17711$) in semi-logarithmic plot in comparison to the solution of the master equation system in Eq. (3.30) are shown in the upper plot. The lower one shows the corresponding flooding values together with the analytic solution of Eq. (3.42).

at all times

$$f_{\text{ch}_m}(t) + f_m(t) = \text{const} . \quad (3.35)$$

In case of a uniform distribution of the wave packet in phase space, which is the case of complete flooding, we demand

$$f_m = f_{\text{ch}_m} = 1 , \quad (3.36)$$

because the flooding values are scaled to one in that case. At $t = 0$ the flooding value of the m -th regular torus is zero $f_m(t = 0) = 0$. With Eq. (3.35) we deduce that $f_{\text{ch}_m}(t = 0) = 2$. The symmetry of the definition in Eq. (3.35) leads to equal rates in both directions for the flooding values in contrast to the regular and chaotic weights. We arrive at a set of rate equation pairs

$$\frac{d}{dt} f_m(t) = \frac{N_{\text{ch}} + M_q}{2N_{\text{ch}}} \gamma_m^{\text{reg} \rightarrow \text{ch}} (f_{\text{ch}_m}(t) - f_m(t)) \quad (3.37)$$

$$\frac{d}{dt} f_{\text{ch}_m}(t) = \frac{N_{\text{ch}} + M_q}{2N_{\text{ch}}} \gamma_m^{\text{reg} \rightarrow \text{ch}} (f_m(t) - f_{\text{ch}_m}(t)) . \quad (3.38)$$

At $t = 0$ this equations reproduce the linear approximation of Eq. (3.22) using $f_{\text{ch}_m}(t = 0) = 2$ as initial condition. The analytic solution is given by

$$f_m(t) = \frac{1}{2} [(1 + \exp(-rt)) f_m(0) + (1 - \exp(-rt)) f_{\text{ch}_m}(0)] \quad (3.39)$$

$$f_{\text{ch}_m}(t) = \frac{1}{2} [(1 - \exp(-rt)) f_m(0) + (1 + \exp(-rt)) f_{\text{ch}_m}(0)] , \quad (3.40)$$

with

$$r = \frac{N_{\text{ch}} + M_q}{N_{\text{ch}}} \gamma_m^{\text{reg} \rightarrow \text{ch}} . \quad (3.41)$$

With respect to the chosen initial conditions, mentioned above, one gets

$$f_m(t) = 1 - \exp(-rt) . \quad (3.42)$$

The lower graph in Fig. 3.10 shows that this simple model is enough to fully describe the flooding values in the case of complete flooding, where the Heisenberg time is much larger than the tunneling time. The definition of the flooding values is appropriate to treat regular tori individually. But we have to emphasize that every model derived using Fermi's golden rule can only work for times much smaller than the Heisenberg time. The only exception is the case of complete flooding, where also the saturation plateaus are well reproduced. The plateaus represent the equilibrium where regular to chaotic and chaotic to regular tunneling exactly cancel each other and the occupation probabilities are equal. In the next section we search for a suitable model to predict all saturation plateaus even for weakly flooded systems.

3.3 Saturation regime

Since we were able to explain the behavior of the flooding values at small times due to the tunneling process and even the saturation plateaus in the complete flooding case, we are now going to give a quantitative prediction for all plateaus.

3.3.1 Saturation value and effective coupling

The flooding values saturate on plateaus of different heights shown in Fig. 3.8. We define the saturation value as the height of those plateaus from the numerical data by an average over the flooding values

$$s = \langle f(t) \rangle_{t > t_{\text{plateau}}} \quad , \quad (3.43)$$

which is determined at times larger than the beginning of the plateau t_{plateau} that is chosen for each plateau individually. Alternatively one can deduce the saturation values in terms of eigenstates of the system as shown in the following.

For simplicity let us assume a model with just one regular state $|\chi_{\text{reg}}\rangle$ in the system. A more general derivation with M_q regular states can be found in App. C.1. The initial wave packet $|\phi(t)\rangle$ at $t = 0$ is assumed to be a random superposition of chaotic states $|\chi_{\text{ch},j}\rangle$

$$|\phi(0)\rangle = \sum_{j=1}^{N_{\text{ch}}} a_j e^{i\xi_j} |\chi_{\text{ch},j}\rangle \quad , \quad \xi_j \in [0, 2\pi] \quad , \quad a_j \in [0, 1] \quad , \quad (3.44)$$

where ξ_j and a_j are random real values under the constraint of normalization. Within this model neither the regular nor the chaotic states are eigenstates of the system. Together they form a complete orthogonal basis. The expansion coefficients in the basis of eigenstates of the system $|\psi_i\rangle$ are

$$c_i = \langle \psi_i | \phi(0) \rangle = \sum_{j=1}^{N_{\text{ch}}} a_j e^{i\xi_j} \langle \psi_i | \chi_{\text{ch},j} \rangle \quad , \quad i = 1, \dots, N \quad . \quad (3.45)$$

The regular weight of $|\phi(t)\rangle$ is given by the modulus squared of the projection on the single regular state $|\chi_{\text{reg}}\rangle$ (see Eq. (3.12))

$$p^{\text{reg}} = |\langle \chi_{\text{reg}} | \phi(t) \rangle|^2 = \sum_{i,j=1}^N c_i c_j^* e^{2\pi i(E_i - E_j)t} \langle \chi_{\text{reg}} | \psi_i \rangle \langle \psi_j | \chi_{\text{reg}} \rangle \quad (3.46)$$

$$= \sum_{i=1}^N |c_i|^2 |\langle \chi_{\text{reg}} | \psi_i \rangle|^2 + 2\Re \left(\sum_{i>j} c_i c_j^* e^{2\pi i(E_i - E_j)t} \langle \chi_{\text{reg}} | \psi_i \rangle \langle \psi_j | \chi_{\text{reg}} \rangle \right) \quad . \quad (3.47)$$

Assuming no degeneracies the second sum only yields rapid oscillations that are uncorrelated at large times. Especially if we account for the ensemble average used in the following, spectral variations eliminate this term. Thus, for the saturation value only the first term is important. Since s is defined as the height of the saturation plateaus of the flooding values we rescale the regular weight just like in the definition of the flooding values in Eq. (3.14) with the total number of states in the subsystem $N = N_{\text{ch}} + 1$

$$s = N \sum_{i=1}^N \langle \langle |c_i|^2 \rangle_{\text{initial}} |\langle \chi_{\text{reg}} | \psi_i \rangle|^2 \rangle_{\text{ensemble}} . \quad (3.48)$$

This equation contains two averages. One is an ensemble average $\langle \cdot \rangle_{\text{ensemble}}$ that affects both the $|\psi_i\rangle$ and the $|c_i|^2$. The other is over initial conditions $\langle \cdot \rangle_{\text{initial}}$ which affects only the $|c_i|^2$. We evaluate the latter as

$$\langle |c_i|^2 \rangle_{\text{initial}} = \left\langle \sum_{j,k=1}^{N_{\text{ch}}} \langle \psi_i | \chi_{\text{ch}j} \rangle \langle \chi_{\text{ch}k} | \psi_i \rangle e^{i(\xi_j - \xi_k)} a_j a_k \right\rangle_{\text{initial}} \quad (3.49)$$

$$= \left\langle \sum_{j=1}^{N_{\text{ch}}} |\langle \psi_i | \chi_{\text{ch}j} \rangle|^2 a_j^2 \right\rangle_{\text{initial}} + \left\langle \sum_{j \neq k}^{N_{\text{ch}}} \langle \psi_i | \chi_{\text{ch}j} \rangle \langle \chi_{\text{ch}k} | \psi_i \rangle e^{i(\xi_j - \xi_k)} a_j a_k \right\rangle_{\text{initial}} \quad (3.50)$$

The second term vanishes because of the statistical independence of the random phases. The average over different initial conditions gives for $\langle a_j^2 \rangle_{\text{initial}} = \frac{1}{N_{\text{ch}}}$ and we get

$$\langle |c_i|^2 \rangle_{\text{initial}} = \frac{1}{N_{\text{ch}}} \sum_{j=1}^{N_{\text{ch}}} |\langle \psi_i | \chi_{\text{ch}j} \rangle|^2 \quad (3.51)$$

$$= \frac{1}{N_{\text{ch}}} (1 - |\langle \chi_{\text{reg}} | \psi_i \rangle|^2) . \quad (3.52)$$

In the second step the completeness and orthogonality of the basis of purely regular and chaotic states has been used. Thus, Eq. (3.48) yields with Eq. (3.48)

$$s = \frac{N_{\text{ch}} + 1}{N_{\text{ch}}} \left(1 - \sum_{i=1}^N \langle |\langle \chi_{\text{reg}} | \psi_i \rangle|^4 \rangle_{\text{ensemble}} \right) . \quad (3.53)$$

For the more general case with more than one regular state on the same regular torus ($M_q \neq 1$) we obtain with a similar approach the mean saturation value (App. C.1)

$$s = \frac{N_{\text{ch}} + M_q}{N_{\text{ch}}} \left(1 - \frac{1}{M_q} \sum_{i,j=1}^{M_q} \sum_{k=1}^{N_{\text{ch}} + M_q} \left\langle \left| \langle \psi_k | \chi_{\text{reg}i} \rangle \right|^2 \left| \langle \psi_k | \chi_{\text{reg}j} \rangle \right|^2 \right\rangle_{\text{ensemble}} \right) . \quad (3.54)$$

Please note, that the ensemble average still occurs in Eq. (3.53) and Eq. (3.54). The quantity s

has zero and one as extremal values. If an eigenstate of the system is equal to a purely regular state it is not flooded at all and the saturation value yields zero. In contrast for a completely flooded state we get a saturation value equal to one as shown in App. C.1.

The height of the saturation plateaus varies from torus to torus. Tori with larger tunneling rates usually also have larger saturation values s . If one increases the number of unit-cells in phase space while keeping the effective Planck constant fixed, the tunneling rates are unchanged, but the saturation values increase. Fig. 3.11 shows the saturation values in dependence of the tunneling rate γ and the number of chaotic states N_{ch}

$$N_{\text{ch}} = N - m_{\text{max}} M_q = M_q \left(\frac{1}{h_{\text{eff}}} - m_{\text{max}} \right) , \quad (3.55)$$

which is proportional to the Heisenberg time $\tau_{\text{H, ch}} = N_{\text{ch}}$. We observe that large tunneling rates and a large number of chaotic states lead to saturation values near one and show that both parameters can be combined such that a universal behavior for the saturation values is found.

As a starting point we consider the coupling matrix elements $V_{\text{reg, ch}}$. They are related to the

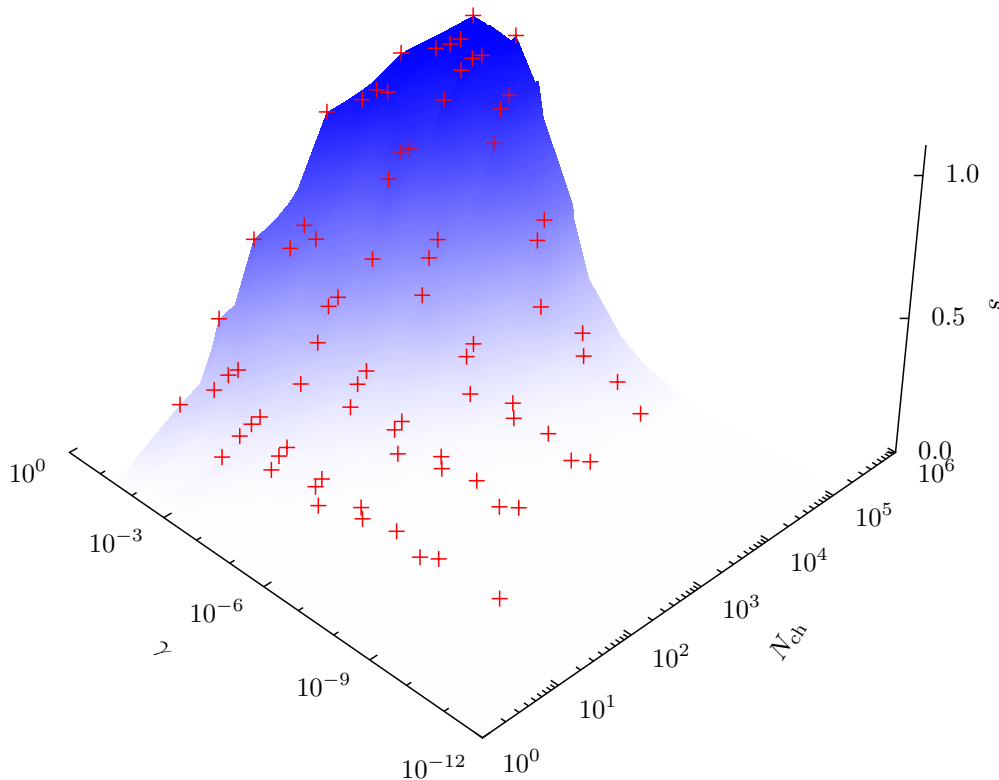


Figure 3.11: Saturation values under variation of the number of chaotic states N_{ch} and the tunneling rate γ . The data points marked in red are numerically computed for the quantum map \mathcal{M}_1 . The surface plot is a guide to the eye and scales from white for $s = 0$ to blue for $s = 1$. High saturation values are found at large tunneling rates and large number of chaotic states.

tunneling rates γ via Fermi's golden rule

$$\gamma = (2\pi)^2 N_{\text{ch}} \langle V_{\text{reg, ch}}^2 \rangle . \quad (3.56)$$

A universal scaling parameter should not depend on the mean level spacing and we rescale the spectrum with the total number of states $N_{\text{ch}} + M_q$ in the considered subsystem (due to the renormalization, we neglect $M_q(m_{\text{max}} - 1)$ states) and define an effective coupling v

$$v = (N_{\text{ch}} + M_q) \sqrt{\langle V_{\text{reg, ch}}^2 \rangle} = \frac{N_{\text{ch}} + M_q}{2\pi} \sqrt{\frac{\gamma}{N_{\text{ch}}}} . \quad (3.57)$$

The quantity is similar to the effective coupling in Ref. [23], where the authors used N_{ch} instead of $N_{\text{ch}} + M_q$ for the rescaling. In most of the considered cases the difference is very small, but for $N_{\text{ch}} = M_q$ large differences are found, see for example Sec. 3.3.2.

The effective coupling allows to handle the flooding independent of the number of involved states. Both parameters, the tunneling rate and the number of chaotic states shown Fig. 3.11 are combined in the definition of the effective coupling and if M_q is small compared to N_{ch} one obtains

$$v \propto \sqrt{N_{\text{ch}} \gamma} . \quad (3.58)$$

We indeed observe in Fig. 3.12 that there is a universal dependence of the saturation values as a function of the effective coupling. Next we want to develop a model to predict the behavior of the saturation values. Therefore we are going to evaluate Eqs. (3.53) and (3.54) by means of a random matrix Hamiltonian.

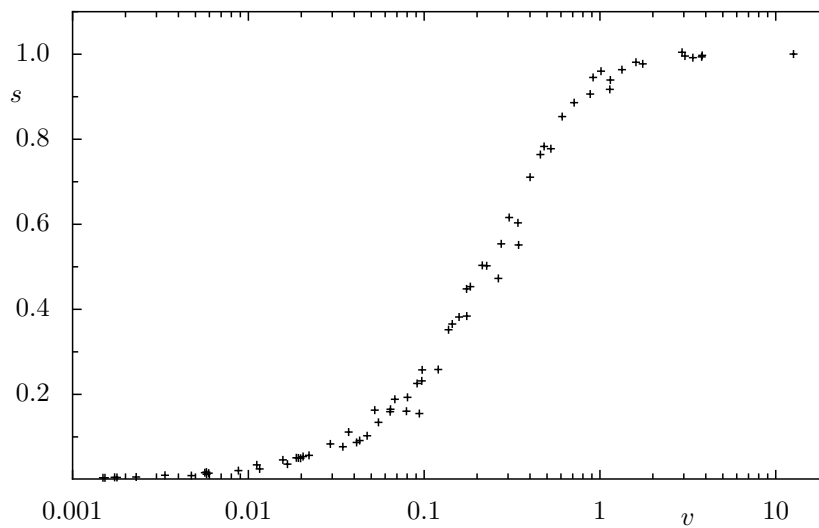


Figure 3.12: Saturation values versus the effective coupling. Every cross marks the height of a saturation plateau of the flooding values deduced from the time evolution in the quantum map \mathcal{M}_1 as are also shown in Fig. 3.11.

3.3.2 Random matrix model

The kicked systems we investigated so far are explicitly time-dependent and characterized by the eigenvalues and eigenstates of the time evolution operator. Thus the spectrum is compact and periodic. In order to describe systems with a mixed phase space one often uses a random matrix model with the time-independent Hamiltonian

$$H = \begin{pmatrix} H_{\text{reg}} & V \\ V^T & H_{\text{ch}} \end{pmatrix} \quad (3.59)$$

which was introduced in Refs. [11, 64, 65]. Here H_{reg} is the Hamiltonian of a purely regular system with the eigenstates $|\chi_{\text{reg}_i}\rangle$, H_{ch} represents a circular orthogonal ensemble with chaotic eigenstates $|\chi_{\text{ch}_j}\rangle$ and eigenvalues in $[-\frac{1}{2}, \frac{1}{2}]$ (see [5]). The coupling matrix V usually is assumed to contain random variables, which are Gaussian distributed with mean value zero. As long as the coupling effects on the spectrum are small such a model can be used to describe kicked systems although the model spectrum is non-periodic. The spectrum of the regular states usually is modeled by Poissonian distributed eigenvalues. Since we are dealing with one-dimensional systems this only holds far in the semi-classical limit. Especially for the elliptic island of the phase-space designed maps $\mathcal{M}_{1,2}$ we find equidistant spacing of eigenphases [59]. As we treat all regular states corresponding to a single quantized torus m separately, we also assume this in the context of the random matrix model and account for M_q regular states in H_{reg} . In the case of more than one unit-cell in phase space $M_q > 1$ there are two possibilities how energy levels of different regular states of the same torus arrange. In Fig. 3.13 the qualitative difference of the uncoupled spectra is shown. If we have a transporting island, as typically used throughout this thesis (\mathcal{M}_1), the classical transport behavior induces a strong coupling of states in different islands and the resulting regular states are far apart in the spectrum (a). Each regular state couples individually to the chaotic states. The case of non-transporting islands (b), e.g. map \mathcal{M}_2 , is quite different and will be discussed in Sec. 3.3.4. We choose the variance of the coupling

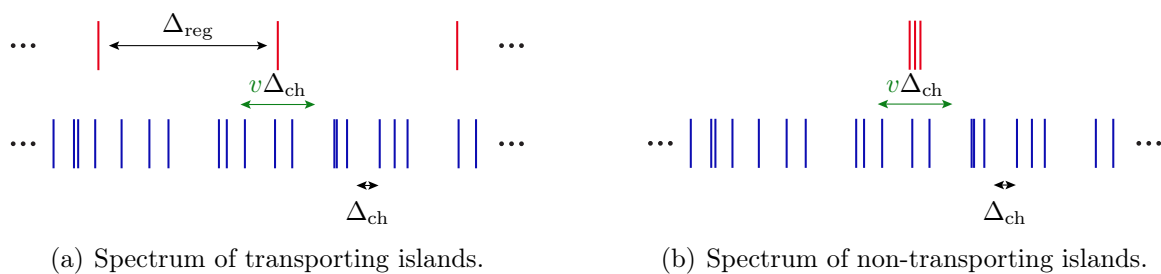


Figure 3.13: The regular spectrum of transporting islands is equidistant and chaotic states usually couple only to one regular state (a). For non-transporting islands we find almost degenerate regular spectra (b). The chaotic states couple to all regular states at once.

matrix elements as

$$\langle V_{\text{reg, ch}}^2 \rangle = \frac{v^2}{N-1} . \quad (3.60)$$

In contrast to Eq. (3.57) the rescaling is done with the factor of $N-1$ instead of just N . The difference is due to the compact but not periodic spectrum in the model system. We find $N-1$ level spacings in the interval of length one instead of one more with periodic boundary conditions.

The easiest approach to compute the saturation values is to diagonalize the Hamiltonian in Eq. (3.59) numerically and analyze the eigenfunctions with Eq. (3.54). Since the Hamiltonian matrix is written in the basis of the uncoupled regular and chaotic states χ_{reg} is a vector with elements

$$(\chi_{\text{reg}_i})_j = \delta_{ij} . \quad (3.61)$$

We are free to choose the number of regular and chaotic state, since we expect universal results independent of the choice we made. In our example systems typically there are more chaotic than regular states due to a regular island that is smaller than the chaotic sea and we consider only one quantized torus with M_q regular states.

The numerical analysis of the corresponding matrix model reveals an effect for strong couplings that is not found for kicked maps due to the periodicity of the corresponding spectrum. If the variance of the matrix elements in V is not small compared to one, the resulting saturation values are much smaller than expected and even decrease with increasing coupling strength. The spectral coupling width is comparable or even larger than the width of the total spectrum in this case. The effect can be explained by a coupling model of one regular state coupled to N_{ch} degenerate chaotic states, which is the reversed situation of the model discussed for systems with non-transporting islands in Sec. 3.3.4. We find an enhanced coupling of two states, whereas all other states retain their spectral position.

Such large individual coupling matrix elements can be avoided with fixed effective coupling v by increasing the number of states N (Eq. (3.60)). In the limit N going to infinity the saturation values converge as is shown in Fig. 3.14 for the two ratios of chaotic to regular states $\frac{N_{\text{ch}}}{N_{\text{reg}}} = 10$ as dashed lines and $\frac{N_{\text{ch}}}{N_{\text{reg}}} = 1$ as solid lines. For small $N = N_{\text{ch}} + N_{\text{reg}}$ each regular state couples only to one chaotic state. This leads especially in the case $\frac{N_{\text{ch}}}{N_{\text{reg}}} = 10$ to very low saturation values. This effect is enhanced with stronger effective coupling and thus there are cases where smaller couplings lead to higher saturation values. The convergence for large N restores the proper monotony of effective coupling and saturation values. We can use lower N in the symmetric case, where it is sufficient to use 400×400 matrices for coupling strength up to $v = 10$ in contrast to $\frac{N_{\text{ch}}}{N_{\text{reg}}} = 10$ where at least 10000×10000 matrices have to be evaluated for a good convergence. The numerical solution of the random matrix model is in good agreement with the saturation values of the quantum map \mathcal{M}_1 as shown in Fig. 3.15. If we consider only matrices, which are large enough, such that the saturation values are sufficiently near to the

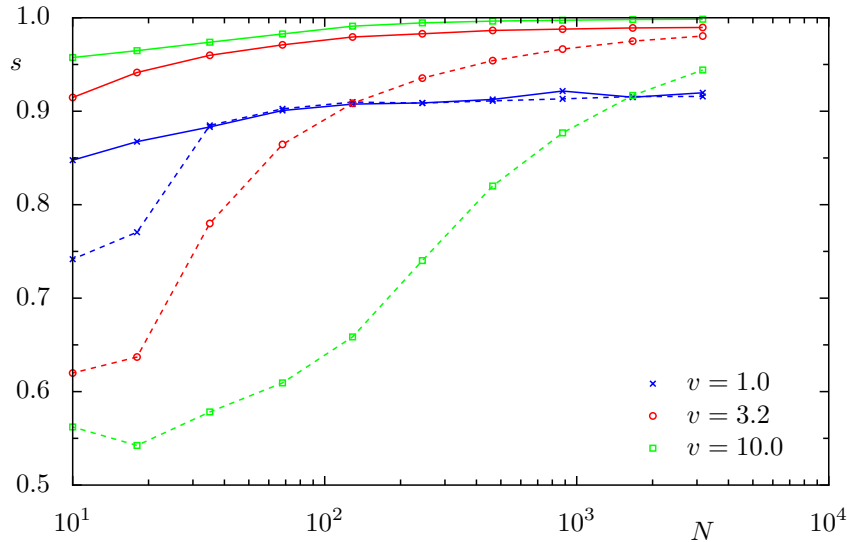


Figure 3.14: Convergence of the saturation value in dependence of the total number of states N in the system. The ratio of regular and chaotic states is fixed to $\frac{N_{\text{ch}}}{N_{\text{reg}}} = 1$ for the solid lines and $\frac{N_{\text{ch}}}{N_{\text{reg}}} = 10$ for the dashed lines. The different colors show calculations for different effective coupling v . The convergence is much slower for larger coupling strengths and larger ratios of chaotic to regular states.

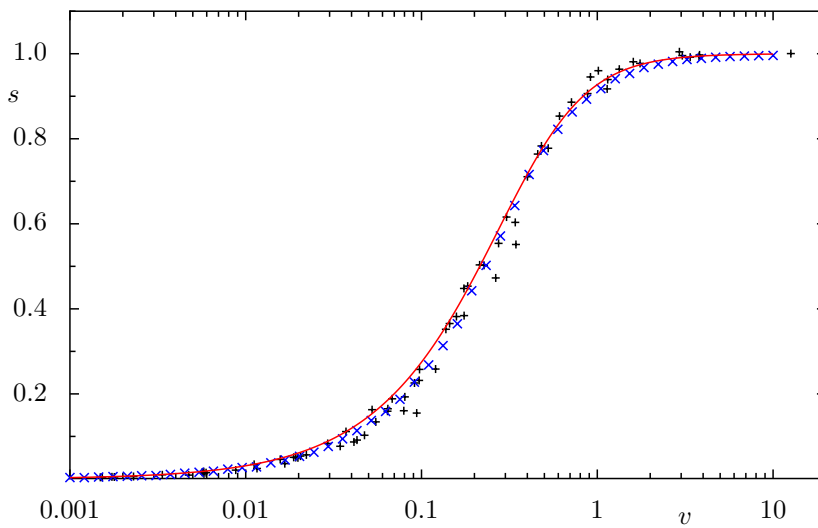


Figure 3.15: Saturation values of the quantum map \mathcal{M}_1 in black compared to the numerical simulation of the random matrix model in blue and the analytic solution of Eq. (3.64) in red. For the RMT model we used 200 regular and 200 chaotic states and averaged over 10 realizations of the system.

limiting value, the saturation values are independent of the ratio of regular to chaotic states.

3.3.3 Simplified RMT model

The very good agreement of the RMT model with the saturation values obtained for the kicked map \mathcal{M}_1 independent of the total number of states, Fig. 3.15, suggests that the matrix model

with only two states may already yield good results. This system is completely solvable analytically. The Hamiltonian is

$$H = \begin{pmatrix} \kappa & v \\ v & -\kappa \end{pmatrix}, \quad \kappa \in \left[-\frac{1}{2}, \frac{1}{2}\right], \quad v > 0. \quad (3.62)$$

In this case the effective coupling v appears directly in the matrix because the rescaling factor $N - 1 = 1$. Usually one would assume random variables for v and κ and average using the corresponding ensemble. But for simplicity we fix the coupling matrix element v and average over a uniform distribution in κ . The behavior of the eigenvalues is sketched in Fig. 3.16(a). The saturation values can be obtained from Eq. (3.53), see App. C.2 for the derivation,

$$s = 2 \left(1 - \left\langle \frac{\kappa^2 + \frac{v^2}{2}}{\kappa^2 + v^2} \right\rangle_{\text{ensemble}} \right) = 2 \left(1 - \int_{-\frac{1}{2}}^{\frac{1}{2}} d\kappa \frac{\kappa^2 + \frac{v^2}{2}}{\kappa^2 + v^2} \right) \quad (3.63)$$

$$= 2v \arctan \frac{1}{2v}. \quad (3.64)$$

Here the integration over κ represents a spectral (ensemble) average. The limits for small and strong coupling are

$$s \stackrel{v \ll 1}{\approx} \pi v \quad (3.65)$$

$$s \stackrel{v \gg 1}{\approx} 1. \quad (3.66)$$

The exact result can be seen in Fig. 3.15 together with the numerical calculations. The agreement of the simple 2×2 model is surprisingly good even for strong coupling where many level

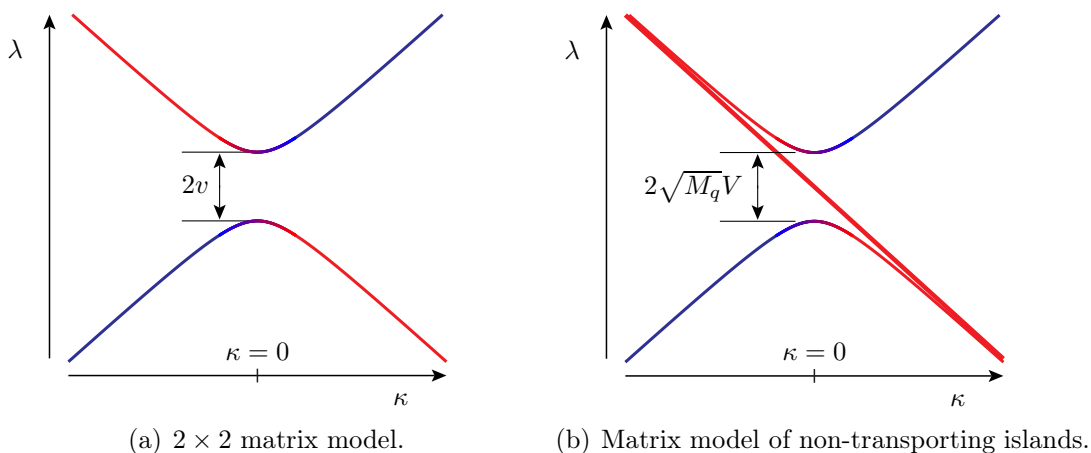


Figure 3.16: Avoided crossing for two different matrix models. The eigenvalues are plotted against the matrix parameter κ . Regular states are marked in red and chaotic states in blue. The Model of non-transporting islands is discussed in Sec. 3.3.4.

couplings are relevant in systems with more than one chaotic state. To obtain a saturation value of one, every regular state has to be coupled to all chaotic states equally. This demonstrates the effect of the rescaling in the saturation values with the factor $\frac{N_{\text{ch}} + M_q}{N_{\text{ch}}}$ and the effective coupling that is the variance of the coupling matrix elements in an unfolded matrix. Using the effective coupling the description of the saturation values is independent of the number of states and even the ratio of regular to chaotic states. The prediction is universal.

3.3.4 Non-transporting islands

The transporting behavior between islands in all unit-cells of phase space implies that usually all regular states corresponding to the same quantum number m are far apart in the spectrum due to their equidistant distribution ([59]). If such a transport is not present (using \mathcal{M}_2 , introduced in Sec. 2.1.2) the coupling between states of different islands is exponentially small resulting in a very small splitting that we can neglect to model the coupling to chaotic states. We treat all these states as degenerate, as shown in Fig. 3.13(b). In Fig. 3.17 such a spectrum is illustrated around the regular states corresponding to the regular torus $m = 0$ as a function of the Bloch-phase θ_q . Two chaotic states cross the group of three regular states. Each chaotic state couples to only one state, which results in just one avoided crossing each. We model such a crossing by a simple matrix with one chaotic state of energy $-\kappa$ and M_q exactly degenerate regular states with energy κ . As a further simplification we assume that all coupling matrix

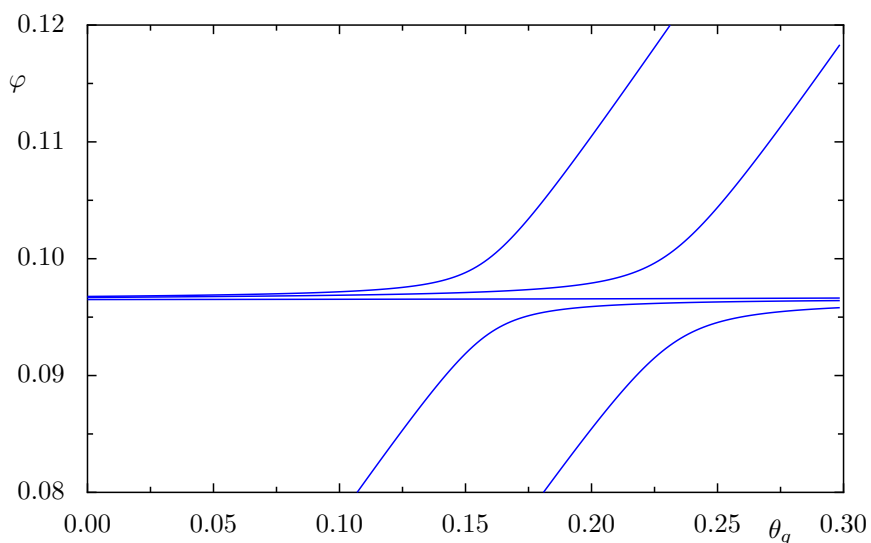


Figure 3.17: Spectrum of a non-transporting quantum map \mathcal{M}_2 with $N = 29$ and $M_q = 3$. Two chaotic states with positive slope cross the group of three regular states with $m = 0$.

elements V are equal

$$H = \begin{pmatrix} -\kappa & V & \cdots & V \\ V & \kappa & & 0 \\ \vdots & & \ddots & \\ V & 0 & & \kappa \end{pmatrix}. \quad (3.67)$$

The eigenvalues of this matrix are derived in App. C.3 and a sketch is shown in Fig. 3.16(b). We find

$$\lambda_{0,1} = \pm \sqrt{\kappa^2 + M_q V^2}, \quad \lambda_{2..M_q+1} = \kappa. \quad (3.68)$$

This model gives the same behavior as observed in Fig. 3.17. There is only one avoided crossing and most of the regular states are unchanged. The splitting of this crossing

$$(\lambda_1 - \lambda_0)|_{\kappa=0} = 2\sqrt{M_q}V \quad (3.69)$$

is enhanced by the factor of $\sqrt{M_q}$ compared to a 2×2 model. We have to take this into account when we define the effective coupling that reflects both, the width and the density of avoided crossings. As the width is larger and the density is smaller by a factor of M_q we get

$$v_{\text{nontrans}} = (N_{\text{ch}} + M_q) \sqrt{\frac{\langle V^2 \rangle}{M_q}} \stackrel{(3.56)}{=} \frac{N_{\text{ch}} + M_q}{2\pi} \sqrt{\frac{\gamma}{M_q N_{\text{ch}}}}. \quad (3.70)$$

This equation gives the relation to the tunneling rates and is used to compute the effective coupling for the map \mathcal{M}_2 . To check the scaling of v_{nontrans} we compare the numerical evaluation of the corresponding random matrix model with the analytic result of Eq. (3.64) and the numerics of the quantum map \mathcal{M}_2 . For the random matrix model $M_q = 5$ regular states and at least $N_{\text{ch}} = 1000$ chaotic states were used. For strong coupling we are forced to use $N_{\text{ch}} = 3000$ states due to the slow convergence. The results are shown in Fig. 3.18 (blue crosses). The analytic prediction (red line) is the same as before and only because of the rescaling by the factor of $\sqrt{M_q}$ in Eq. (3.70) of the effective coupling the good agreement is found. Also the saturation values of the quantum map \mathcal{M}_2 with parameters marked as black crosses are well described by this model. Unfortunately the behavior of v_{nontrans} prevents the possibility to reach high coupling strengths by increasing M_q . This can be seen by introducing the number of chaotic states per unit-cell

$$n_{\text{ch}} = N_{\text{ch}}/M_q, \quad (3.71)$$

which depends only on the area of the chaotic sea per unit-cell and the Planck constant h_{eff} . With Eq. (3.70) one obtains

$$v_{\text{nontrans}} = \frac{n_{\text{ch}} + 1}{2\pi} \sqrt{\frac{\gamma}{n_{\text{ch}}}}. \quad (3.72)$$

Thus, there are no high saturation values near one for the numerical results of the quantum map \mathcal{M}_2 . The effect of increasing the density of chaotic states, by increasing the number of unit-cells in phase space M_q , is exactly canceled by the rescaling of the effective coupling.

3.4 Full time-dependent solution

The simple two-by-two matrix model gives very good results for the prediction of the universal scaling of the saturation values. Now we want to discuss the circumstances in which this model can also describe the full time-dependence.

In the matrix model, Eq. (3.62), we directly use the effective coupling in the off-diagonal elements. Both parameters κ and v have the dimension of an energy. Although the rescaling with the mean density of states N gives the right saturation values in all cases we have to keep in mind, that this kind of rescaling of energies also changes the dimension of time measurements

$$\tilde{E} = NE \quad \rightarrow \quad \tilde{t} = \frac{1}{N}t, \quad N = N_{\text{ch}} + M_q. \quad (3.73)$$

The full solution of the 2×2 matrix model in Eq. (3.62), derived in App. C.2, gives for the flooding values $f(t)$ the expression

$$f(t) = 2v \int_0^{\frac{1}{2v}} d\delta \frac{1 - \cos(4\pi v t \sqrt{\delta^2 + 1})}{\delta^2 + 1}, \quad \text{with } \delta = \frac{\kappa}{v}. \quad (3.74)$$

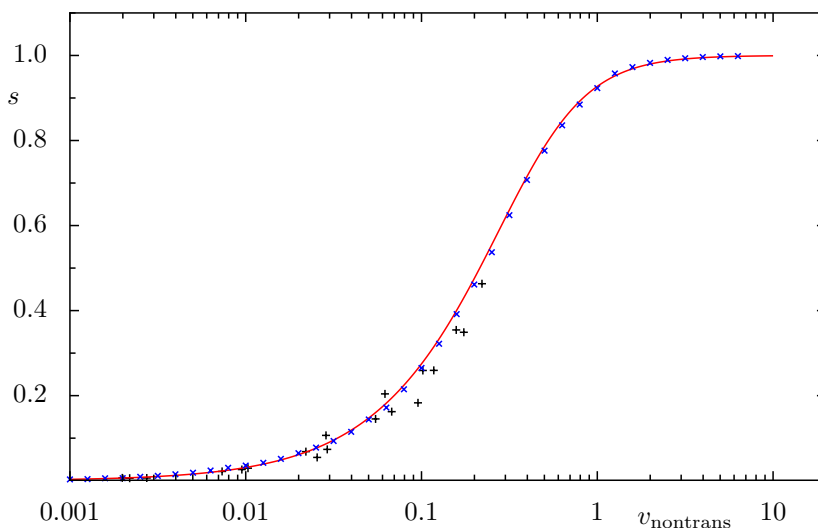


Figure 3.18: Saturation values of non-transporting islands plotted against the rescaled effective coupling. The blue crosses show the random matrix model results with 5 degenerate regular states. The solid red line represents the analytic prediction. The black points mark the saturation values of the non-transporting quantum map \mathcal{M}_2 .

To solve the integral we approximate the upper limit for small coupling strength v and extend the integration up to infinity

$$f(t) \stackrel{v \ll 1}{\approx} 2v \int_0^\infty d\delta \frac{1 - \cos(4\pi vt \sqrt{\delta^2 + 1})}{\delta^2 + 1} . \quad (3.75)$$

This yields after some manipulations (see App. C.2) the expression

$$f(t) \stackrel{v \ll 1}{\approx} 4\pi^2 v^2 t \left(\mathbf{J}_0(4\pi vt) - \frac{\pi}{2} [\mathbf{J}_0(4\pi vt) \mathbf{H}_1(4\pi vt) - \mathbf{J}_1(4\pi vt) \mathbf{H}_0(4\pi vt)] \right) . \quad (3.76)$$

Here \mathbf{J}_n are the Bessel functions and \mathbf{H}_n the Struve functions of integer order n . The first derivative of $f(t)$ is

$$\dot{f}(t) = 4\pi^2 v^2 \mathbf{J}_0(4\pi vt) . \quad (3.77)$$

As $\mathbf{J}_0(x) \approx 1 - \frac{x^2}{4}$ for small x , we find for small times t a linear time-dependence

$$f\left(t \ll \frac{1}{4\pi v}\right) = 4\pi^2 v^2 t . \quad (3.78)$$

If we replace the time t by t/N , where $N = N_{\text{ch}} + M_q$ is the number of states in the system we want to compare with, and the effective coupling with Eq. (3.57) we arrive at

$$f\left(t \ll \frac{N_{\text{ch}} + M_q}{4\pi v}\right) \approx \frac{N_{\text{ch}} + M_q}{N_{\text{ch}}} \gamma_m^{\text{reg} \rightarrow \text{ch}} t . \quad (3.79)$$

Thus we get a theoretical explanation of the relation Eq. (3.22). The integrand of Eq. (3.74) is a rapidly oscillating function, similar to the Rabi oscillations observed earlier in Sec. 3.1.2. By averaging we find a short time behavior that is equivalent to the Fermi golden rule result of Eq. (3.22) in Sec. 3.2.1. The black curve in Fig. 3.19 shows Eq. (3.76) compared to the numerical data of the quantum map \mathcal{M}_1 . The agreement is very good especially at short times. The saturation plateau, however, is too high, because we overestimated it by approximation of the upper bound of the integral.

If we evaluate the integral in Eq. (3.74) numerically (e.g. with the Romberg algorithm) we obtain the red curve in Fig. 3.19. The saturation plateau is much better approximated, but the behavior at small times is quadratic instead of linear, which can be understood by approximating the integrand in Eq. (3.74) for small times (t is again substituted by $\frac{t}{N}$)

$$f(t) = 2v \int_0^{\frac{1}{2v}} d\delta \frac{(4\pi v)^2 t^2}{2N^2} = 16v^2 \pi^2 \frac{t^2}{N^2} . \quad (3.80)$$

Here the time has to be smaller than the period of the Rabi oscillation $t \ll \frac{N}{2v\sqrt{\delta^2+1}}$. The

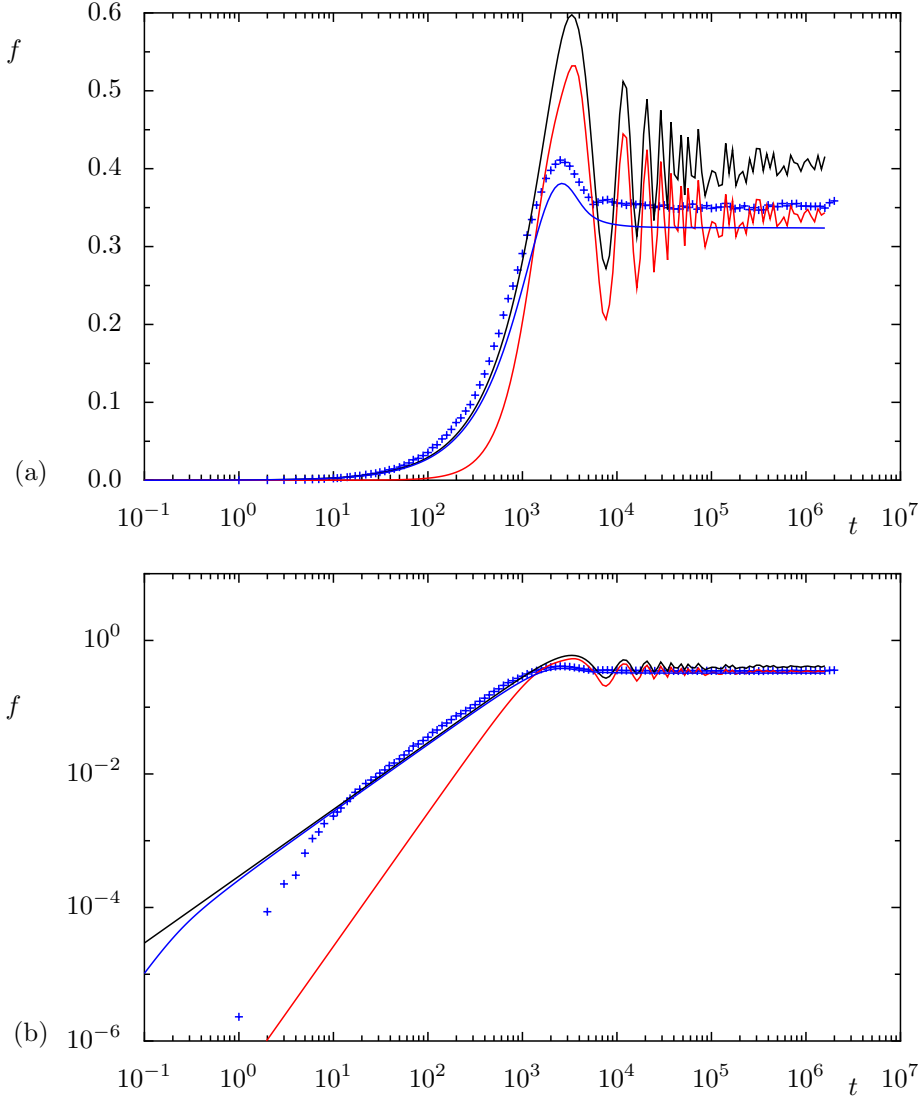


Figure 3.19: The flooding values with $m = 1$ for the quantum map \mathcal{M}_1 with $M_q = 144$ and $N = 2825$ as blue dots. The black curve shows the analytic approximation of the 2×2 model in Eq. (3.76). The red curve shows the numerical integration of Eq. (3.74) (using $\tilde{t} = \frac{1}{N}t$) and the blue curve demonstrates the numerical integration of Eq. (3.81) with shifted integration boundary and a Gaussian average over the coupling matrix elements. The flooding values are shown on a linear scale in (a) and on a logarithmic scale in (b).

smallest periodic time is given by the upper limit of the integration $t \ll \frac{N}{\sqrt{4v^2+1}}$. Thus we find a quadratic increase at small times as long as we consider a finite upper integration limit. This demonstrates that the linear increase is due to the Rabi oscillations far away from the center of the avoided crossings $\delta \gg 1$. The modulus of these oscillations is very small such that they are irrelevant for the saturation plateau, but they dominate the small flooding values at short times. Whenever there is a crossing with one state, the saturation value at this parameter is dominated by both states involved in the crossing, but the coupling to other states, although far away in the spectrum, is causing the linear increase. The rescaling of the energies and coupling matrix elements allows to consider only a single avoided crossing of two neighboring

states (regular and chaotic), that is well described by the 2×2 model. With this approximation, however, we neglect couplings to all other chaotic states in the spectrum that are farther away from the regular state.

The overshooting effect in the intermediate regime from linear increase to saturation is much stronger for both analytical solutions than in the numerical data (\mathcal{M}_1). This can be understood as follows: If there is only one avoided crossing, the width of that crossing sets the smallest frequency of Rabi oscillations in the system. This leads to very strong oscillations even at large times. In a typical system the coupling matrix elements and thus the width of avoided crossings are Gaussian distributed. If we do an additional ensemble average over different values of v of the solution in Eq. (3.76) we can account for this distribution

$$\bar{f}(t) = \sqrt{\frac{8}{\pi v^2}} \int_0^\infty d\tilde{v} \exp\left(-\frac{\tilde{v}^2}{2v^2}\right) f(\tilde{v}, t) . \quad (3.81)$$

The blue curve in Fig. 3.74 is computed by a numerical evaluation of Eq. (3.81). The overshooting effect now is well reproduced. The predicted saturation plateau is too low, while without the average it was overestimated. Using the approximation for small couplings in Eq. (3.65) $f(v, t \rightarrow \infty) \approx \pi v$ in Eq. (3.81) gives

$$\sqrt{\frac{2}{\pi v^2}} \int_0^\infty d\tilde{v} \exp\left(-\frac{\tilde{v}^2}{2v^2}\right) \pi \tilde{v} = \sqrt{\frac{2}{\pi}} \pi v \approx 0.8\pi v . \quad (3.82)$$

Thus, the Gaussian average decreases the plateaus by a factor of 0.8.

To summarize the discussion: the two-by-two matrix model is capable to predict the saturation plateaus in systems where a sufficiently large spectral average is possible. The full time-dependence and especially the linear increase can only be reproduced if also couplings to chaotic states far away in the spectrum are considered. Although the corresponding flooding amplitudes are very small, they dominate the behavior at small times. The overshooting effect, a remnant of Rabi oscillations, can be explained qualitatively by a superposition of Rabi oscillations with different frequencies. A single avoided crossing leads to strongly correlated frequencies at the center of the crossing, which leads to a pronounced overshooting effect. The right behavior is reproduced if additionally an average over different coupling strengths v is considered. Hence, the flooding effect in the quantum map \mathcal{M}_1 can be well understood. All results rely strongly on averaging. In the following section we discuss a system, namely the standard map, where the possibility of spectral averaging is limited.

3.5 Flooding in the standard map

In contrast to the phase space designed maps $\mathcal{M}_{1,2}$, discussed in the previous sections, the standard map (see Eq. (2.10) Page 6) shows no transport behavior neither in the chaotic sea nor in the regular island. The Bloch phase θ_q is fixed due to the quasi periodicity condition Eq. (2.47) (Page (2.47)) and thus we can only vary the Bloch phase θ_p . Here we consider the case of just one unit-cell, $M_q = 1$. Therefore every quantized torus contains one regular state. As illustrated in Fig. 3.20 the occurrence of avoided crossings is very rare in this case. Around $\theta_p = 0.5$ where the position lattice is exactly centered in the interval $[0, 1]$ and the evaluation of the potential of the standard map is anti-symmetric in respect to $q = 0.5$, we find that almost every regular state is crossed or rather touched by a chaotic state. The only exception is the state $m = 0$, which should have the smallest coupling and thus the smallest splitting at the crossing. Later we will see that this state is not crossed at all. Due to the lack of substantial spectral averaging in this example the resulting flooding values in Fig. 3.21 do not show the same qualitative behavior as the previously considered systems. The linear increase is not formed clearly and the height of the saturation plateaus is not well reproduced by the analytic prediction. The usual fluctuations in the coupling matrix elements are directly reflected in the saturation values, because there is just one or two crossings with only one chaotic state. The regular state with quantum number $m = 0$ is not crossed at all by a chaotic state and shows a significantly lower saturation plateau as expected. It is almost two orders of magnitude smaller than the prediction.

The distinctive time-dependence of the flooding value for $m = 1$ suggests that this curve

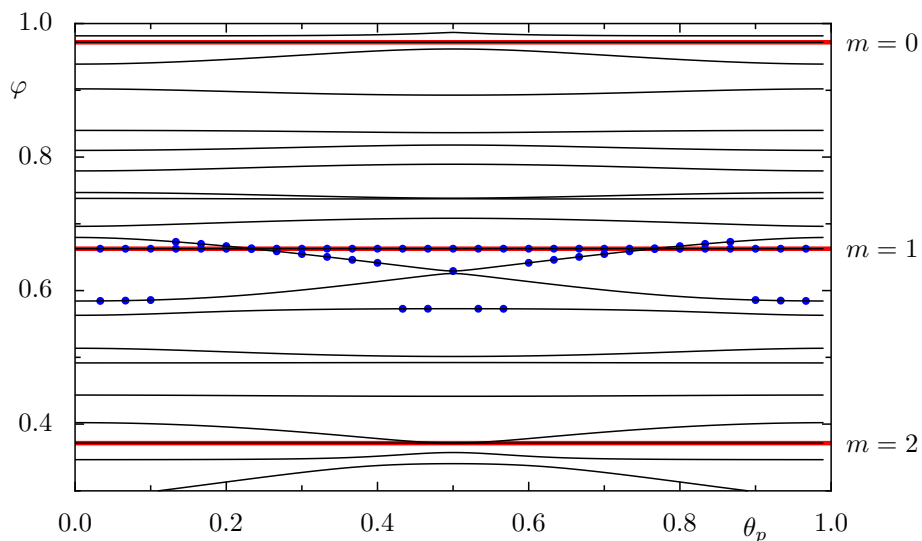


Figure 3.20: Spectrum of the standard map with $k = 2.9$ and $\theta_q = 0.5$ under variation of θ_p . The number of states is $N = 29$ with only one unit-cell in phase space $M_p = M_q = 1$. Regular states form horizontal lines marked in red. There are very few symmetry related avoided crossings around $\theta_p = 0.5$. The two states with the highest regular weight $|\langle \chi_{\text{reg}1} | \psi_i \rangle|^2$ with quantum number $m = 1$ are marked with blue dots for several phases θ_p .

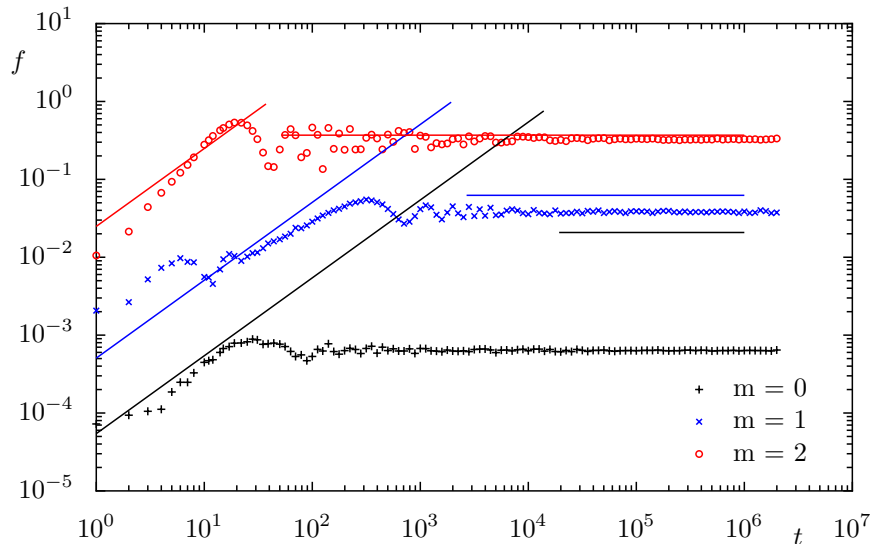


Figure 3.21: Flooding values of the standard map for $N = 29$ and $M_q = M_p = 1$. The linear slope derived from the tunneling rate, Eq. (3.22), and the theoretical prediction for the saturation values, Eq. (3.64), is shown for each quantum number m as solid lines to compare with the data of the time evolution.

is not just one flooding value with linear increase, overshooting, and saturation plateau, but actually two superimposed flooding curves with different time scales

$$f(t) = f_1(t) + f_2(t) . \quad (3.83)$$

We want to understand this behavior. As already shown in Fig. 3.20 there are at least three different eigenstates in the system which show strong couplings to the regular state with $m = 1$. The first follows the regular eigenphase and the second actually crosses this line and forms a small avoided crossing around $\theta_p \approx 0.23$. The modulus of the coupling matrix element $|V|$ can be computed from that splitting $\Delta\varphi = |\varphi_1 - \varphi_2|_{\theta_p \approx 0.23}$

$$|V| = \frac{\Delta\varphi}{2} \quad (3.84)$$

and the value is in good agreement with the value derived from the tunneling rates γ , Eq. (3.56),

$$|V| = 5.972 \cdot 10^{-4} \approx \sqrt{\frac{\gamma}{N_{\text{ch}}}} = 7.027 \cdot 10^{-4} . \quad (3.85)$$

To compare with a 2×2 matrix model we have to make adaptations to the coupling matrix element. Usually we scale the averaged coupling matrix element with the number of states in the system or the inverse density of states as defined in Eq. (3.57). This determines the influence region of the avoided crossing and tells how far apart the two particular states can be in the spectrum. Without sufficient averaging in the system this scaling factor can only be of

the order of magnitude of $N_{\text{ch}} + 1$ and the effective coupling v_1 is given by

$$v_1 = r(N_{\text{ch}} + 1)|V| , \quad (3.86)$$

where r is a free parameter. As we use this factor in the rescaling of time $\tilde{t} = t/(r(N_{\text{ch}} + 1))$, the timescale of oscillations is already fixed by the exact splitting of the avoided crossing as long as the effective coupling is small compared to one, $v \ll 1$. The only drastic effect of the scaling factor is the height of the saturation plateau. Assuming that only the coupling to the first state is relevant for the height of the plateau one gets

$$\langle f_{\mathcal{M}_{\text{standard}}}(t) \rangle_{t > t_{\text{plateau}}} \stackrel{(3.64)}{=} 2v_1 \arctan\left(\frac{1}{2v}\right) \approx \pi v_1 . \quad (3.87)$$

Thus we obtain the coupling v_1 from the saturation plateau and with Eq. (3.86) the scaling factor is evaluated $r \approx 0.752$,

$$v_1 = 1.121 \cdot 10^{-2} = 0.752(N_{\text{ch}} + 1)|V| . \quad (3.88)$$

We derive the first part of the flooding value

$$f_1(t) = 2v_1 \int_0^{\frac{1}{2v_1}} d\delta \frac{1 - \cos(4\pi v_1 t \sqrt{\delta^2 + 1})}{\delta^2 + 1} . \quad (3.89)$$

The third state involved in the coupling process is a bit more difficult to handle. Actually there are two states that qualify for this third state as shown in Fig. 3.20 marked with the lowest blue dot for every phase θ_p . But the relevant distance from the regular state in the spectrum is comparable. In this case we cannot derive the coupling matrix element via the splitting of avoided crossings because there is no crossing. We will model the influence of this state by a two-by-two matrix far away from the center of the avoided crossing. To do that we choose a smaller integration region in the interval $\delta \in [\delta_0, \delta_1]$. There seems to be no obvious way to determine this interval accurately. Hence, we choose a rough estimate around the splitting of both involved states Δ for $\theta_p = 0$ and with the usual rescaling with the number of states in the considered subsystem $N_{\text{ch}} + 1$ we use

$$\delta_0 = \frac{0.8(N_{\text{ch}} + 1)\Delta}{v_2} \quad \delta_1 = \frac{1.2(N_{\text{ch}} + 1)\Delta}{v_2} . \quad (3.90)$$

Slight changes to that interval are partially nullified by the following least square fit to obtain the coupling matrix element v_2 . Therefore the first part of the solution is subtracted from the

numerical data

$$f_{\mathcal{M}_{\text{standard}}}(t) - f_1(t) = f_2(t) = \frac{v_2}{(1.2 - 0.8)(N_{\text{ch}} + 1)\Delta} \int_{\delta_0}^{\delta_1} d\delta \frac{1 - \cos(4\pi v_2 t \sqrt{\delta^2 + 1})}{\delta^2 + 1} \quad (3.91)$$

and we obtain

$$v_2 = 2.8551 \frac{N_{\text{ch}} + 1}{2\pi} \sqrt{\frac{\gamma}{N_{\text{ch}}}}. \quad (3.92)$$

The coupling matrix element is much larger than the average coupling matrix element computed from the tunneling rates. This might be expected since those levels are far from the regular state, but the coupling seems to be stronger than the nearer level with the small crossing. Now we can put both terms together as in Eq. (3.83). The result is shown in Fig. 3.22. The agreement is very good, but the gain is rather qualitative since quantitative information of the quantum map result is used. The saturation plateau is slightly too high, because the coupling to the third state also has a small impact on the saturation value, which was neglected. This demonstrates the strong effect of spectral fluctuations in systems with no possible average over many avoided crossings. Usually the effect of strongly coupled states far apart in the spectrum leads to a linear increase by averaging, but the spectral distance is almost constant in this case and this results in visible Rabi oscillations at short times.

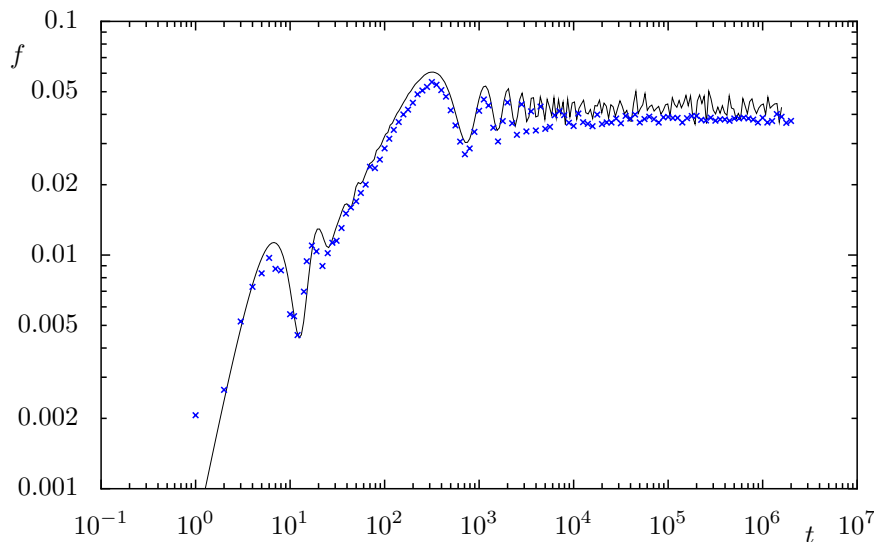


Figure 3.22: Flooding value of the torus $m = 1$ for the standard map with $N = 29$ and $M_q = M_p = 1$. The numerical time evolution is marked in blue and the combined model of two separate two-by-two matrix models is shown as a solid black line.

3.6 Flooding in the mushroom billiard

The phenomenon of flooding is not restricted to quantum maps and appears also in other systems with a mixed phase space such as two dimensional billiards. As an example we investigate the mushroom billiard. This billiard system is particularly suited, because the transition region from the regular island to the chaotic sea is very sharp and the purely regular eigenfunctions are analytically known as the eigenfunctions of the circular billiard. The most significant difference to quantum maps is the spectrum of eigenvalues. For billiards the spectrum is discrete and unbounded. We have to formulate the effective coupling and the saturation values in this case. Here we assume $\hbar = 2m = 1$. A formula for the tunneling rates can be obtained from Fermi's golden rule [1]

$$\gamma = 2\pi \langle |V|^2 \rangle \rho_{\text{ch}} \quad , \quad (3.93)$$

where ρ_{ch} is the density of states in the chaotic sea and V are the regular-to-chaotic coupling matrix elements. We approximate ρ_{ch} via the derivative of the first Weyl term as in Ref. [1]

$$\rho_{\text{ch}} \approx \frac{A_{\text{ch}}}{4\pi} = \frac{1}{4\pi} \left(la + [R^2 \arcsin(a/R) + a\sqrt{R^2 - a^2}]/2 \right) \quad . \quad (3.94)$$

To get the effective coupling from the matrix elements we have to rescale with the density of states. We concentrate again on each single regular state and assume a subsystem with one regular and the chaotic states. Thus we rescale just with the density of chaotic states

$$v = \sqrt{\langle |V|^2 \rangle} \rho_{\text{ch}} = \sqrt{\frac{\gamma \rho_{\text{ch}}}{2\pi}} \quad . \quad (3.95)$$

The saturation values are defined similarly to Eq. (3.53) with $N_{\text{ch}} \rightarrow \infty$

$$s = \left(1 - \sum_{i=0}^{\infty} \langle |\langle \chi_{\text{reg}}^{(n,m)} | \psi_i \rangle|^4 \rangle \right) \quad , \quad (3.96)$$

with the regular wave function

$$\chi_{\text{reg}}^{(n,m)}(\rho, \varphi) \propto \mathbf{J}_m(j_{mn}\rho) \sin(m\varphi) \quad (3.97)$$

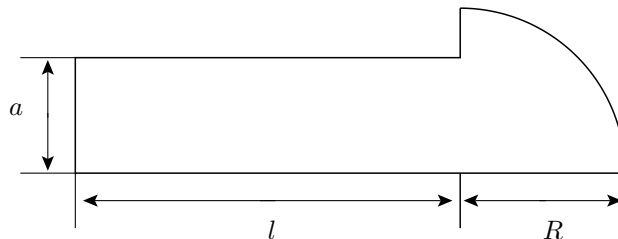


Figure 3.23: Desymmetrized mushroom billiard with stem length $l \in [1.4, 2.3]$, stem width $a = 0.7$, and radius $R = 1$.

where \mathbf{J}_m is the m -th Bessel function and j_{mn} the n -th zero of the m -th Bessel function.

We test the applicability of the formula for the saturation values via numerical computations using the improved method of particular solutions [55, 56] to evaluate eigenvalues and eigenfunctions in a desymmetrized mushroom billiard as shown in Fig. 3.23 with radius $R = 1$ and stem width $a = 0.7$. For an ensemble average we vary the length of the stem in the interval $l \in [1.4, 2.3]$. Especially the chaotic eigenfunctions are strongly influenced by this variation, while the regular states are essentially unchanged. The effective coupling depends on the density of states in the chaotic sea, which is increasing with the length of the stem. We use the mean value of the effective coupling for all values of the length in Fig. 3.24. The saturation values are marked in black for all regular states in the energy interval $E \in [150, 2000]$. The errors in v -direction show the variation interval of v depending on the length. The error bars in s -direction illustrate the error of the mean value of all realizations. The overall agreement with the flooding prediction shown in red is good, but the deviations are stronger than the error bars suggest. One reason are errors in the tunneling rates. We consider large tunneling rates, which result from broad avoided crossings, that can be measured sufficiently accurate with the resolution of 480 values of the stem length l in the considered interval. The analytic prediction [1]

$$\gamma = \frac{8}{\pi} \sum_{s=1; s \neq 3k}^{\infty} \frac{\mathbf{J}_{m+\frac{2s}{3}}(j_{mn}a)^2}{\mathbf{J}_{m-1}(j_{mn})^2}, \quad (3.98)$$

however, gives better results for smaller tunneling rates. This formula leads to good predictions over many orders of magnitude but there are local deviations especially for large tunneling rates up to a factor of four. To increase the accuracy further one would have to determine the tunneling rates with a very fine resolution of avoided crossings. To find high saturation values near one, we would have to increase the length of the stem up to $l \approx 45$ to gain an effective coupling greater than one. However, the length of the stem enters the formula for v only in the square root via the density of states (Eqs. (3.94) and (3.95)). The numerical method used for this computation, however, is not sufficient to do these calculations as the algorithm gets more and more unstable and demands much more computation time for larger stem lengths.

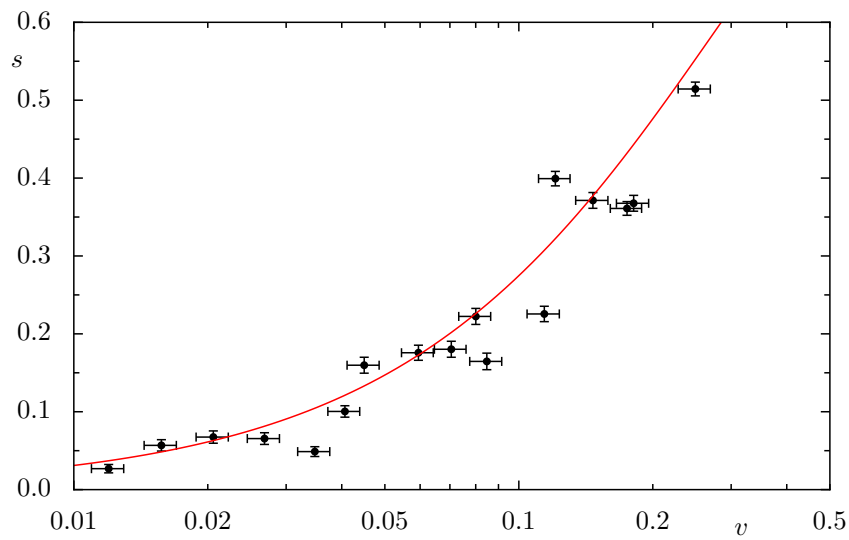


Figure 3.24: Saturation values for the mushroom billiard in black compared to the analytic prediction in red. The errors in v -direction show the variation interval of v depending on the length. The error bars in s -direction illustrate the error of the mean value of all realizations.

4 Flooding in open quantum systems

In this chapter we apply our knowledge of flooding in closed systems to open quantum systems. Starting from the situation of a closed system with flooded regular states in Sec. 4.1 we study quantum maps, which exhibit the reappearance of regular states when opening the system. In the following Sec. 4.2 we analyze two dimensional systems. Investigating the mushroom billiard experimentally, we find signatures of the reappearance effect.

4.1 Open quantum maps

We consider open systems with an effective Hamiltonian H_{eff} as described in Ref. [66]

$$H_{\text{eff}} = H_0 - iW = H_0 - iV^T V \quad , \quad (4.1)$$

where H_0 is a hermitian operator of the corresponding closed system and the imaginary part W in the Hamilton operator introduces an absorption. This absorption W can be described by V the coupling to different escape channels. For the designed map \mathcal{M}_2 we introduce in the chaotic sea an opening, which is defined in momentum space and the effective Hamiltonian operator is given by

$$H_{\text{eff}} = T(p) + \sum_n V(q)\delta(n-t) - i\hbar_{\text{eff}}\eta\Theta(\alpha-p)\Theta(p-1/2+\alpha) \quad . \quad (4.2)$$

As the additional imaginary part of H_{eff} only depends on the momentum, it can be included in the kinetic energy. There are two new parameters: The opening strength η and the width parameter α that controls the upper and lower limit of the absorbing region in p -direction. Increasing the parameter α increases the distance of the absorbing region to the regular island. The mapping defined by Eq. (2.5) with an effective Hamiltonian Eq. (4.2) using the kinetic energy $T(p)$ and the potential $V(q)$ of \mathcal{M}_2 will be called $\mathcal{M}_{\text{open}}$. For the number of cells in q -direction we use $M_q = 1$. The phase space is illustrated in Fig. 4.1 with an absorbing region, marked in blue, that is located within the chaotic sea. Quantum mechanically this system is described by a non-unitary time evolution operator U_{open} (using the effective Hamiltonian in

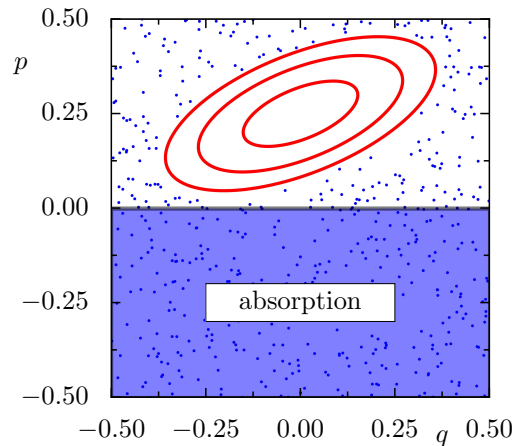


Figure 4.1: Classical phase space of the map \mathcal{M}_2 with an absorbing region in the chaotic sea marked in blue. The width parameter α of the opening is set to zero.

Eq. (4.2))

$$U_{\text{open}} = e^{-i/\hbar_{\text{eff}}V(q)} e^{-i/\hbar_{\text{eff}}T(p)} e^{-W(p)/\hbar_{\text{eff}}} \quad (4.3)$$

$$= U_{\mathcal{M}_2} A = U_{\mathcal{M}_2} e^{-\eta\Theta(\alpha-p)\Theta(p-1/2+\alpha)} . \quad (4.4)$$

The eigenequation follows as

$$U_{\text{open}} |\psi_n^R\rangle = e^{-\frac{\gamma n}{2} - 2\pi i \varphi_n} |\psi_n^R\rangle \quad (4.5)$$

$$\langle \psi_n^L | U_{\text{open}} = e^{-\frac{\gamma n}{2} - 2\pi i \varphi_n} \langle \psi_n^L | , \quad (4.6)$$

where $|\psi_n^R\rangle$ are the right and $\langle \psi_n^L |$ the left eigenfunctions. Both are referred to as resonance states. Due to the non-unitarity of the operator U_{open} the eigenfunctions $|\psi_n^R\rangle$ and $|\psi_n^L\rangle$ are not equal. Both sets, $|\psi_n^L\rangle$ and $|\psi_n^R\rangle$, do not form an orthonormal basis in \mathbb{C}^N . By generalization of the scalar product we find a biorthogonal basis consisting of both the left and the right eigenfunctions [67, 68]

$$\langle \psi_i^L | \psi_j^R \rangle = \delta_{ij} \quad (4.7)$$

implying the completeness relations

$$\mathbb{1} = \sum_i |\psi_i^R\rangle \langle \psi_i^L | \quad (4.8)$$

$$= \sum_i |\psi_i^L\rangle \langle \psi_i^R | . \quad (4.9)$$

In order to study flooding in open systems we have to adapt the derivations which are performed for closed systems in Sec. 3.3.2. The time evolution on very large timescales which leads to the final result of Eq. (3.53) is no longer applicable for open systems due to the loss of probability with every time step. Nevertheless, one may consider the saturation value of Eq. (3.53) as a

measure of how strongly a regular state $|\chi_{\text{reg}}\rangle$ is distributed over the resonance states $|\psi_i^{L,R}\rangle$ of the open system. In addition we introduce a renormalization, which accounts for the non-complete expansion in either set of left or right eigenfunctions

$$s_{\text{open}} = \frac{N_{\text{ch}} + 1}{N_{\text{ch}}} \left(1 - \frac{\sum_{i=1}^N \left| \langle \chi_{\text{reg}} | \psi_i^{L,R} \rangle \right|^4}{\left(\sum_{i=1}^N \left| \langle \chi_{\text{reg}} | \psi_i^{L,R} \rangle \right|^2 \right)^2} \right). \quad (4.10)$$

In this context we abandon the ensemble average that is present in Eq. (3.53) and study the coupling effect directly. Thereby we use the fluctuations of the saturation values s_{open} to find strong coupling even in systems with a low density of states. The Bloch phase θ_q of $QMap_2$ is fixed at a value with large saturation value s_{open} . This occurs if several chaotic states are very close to a regular state in the spectrum and the distance is smaller than the mean density of states. Note, that the renormalization has a small effect on the following numerical study as the denominator in Eq. (4.10) is always close to one.

4.1.1 Reappearance of regular states

First we consider the spectrum of eigenvalues under variation of the strength of the opening. In order to demonstrate the reappearance of regular states we concentrate on systems with a small number of states N . Fig. 4.2 shows the decay rate γ_n and the eigenphases φ_n under variation of the opening parameter η . Weak absorption is marked in blue and strong absorption is encoded in red on a logarithmic scale as indicated by the color bar on the right-hand side.

For small η absorption is weak and all decay rates are small. With increasing η absorption increases and all decay rates initially rise proportional to η . Yet there are some states, like the regular states in the center of the island, that show very slow decay.

The insets show the Husimi-functions for the right eigenfunctions of the red-marked eigenvalues. At a critical value of the absorption the decay rate of some states stops to increase. Although absorption is further increased the decay rate of these resonances remains small or even decreases slightly. These states are called trapped states. This effect is seen for example for the regular state depicted on the right-hand side of Fig. 4.2. A more detailed discussion on resonance trapping without the context of flooding can be found in Refs. [26–28]. Many of the trapped states are regular states, which is intuitively clear, because the opening is located in the chaotic sea.

For the three states, which are shown as Husimi-functions on the left-hand side, we find strong regular and chaotic mixing, indicated by a high saturation value s_{open} for weak absorption (small η). For strong absorption one of the states gets trapped and forms a purely regular state with small decay rate, while the other two states turn into states, which concentrate in the chaotic

part of the phase space, and exhibit a large decay rate ($s_{\text{open}} \approx 0$). This demonstrates the reappearance of a regular state, which is flooded in the closed system, but reappears if the absorption in the chaotic sea is strong enough.

The Husimi-functions of the same four resonance states as depicted in Fig. 4.2 are also shown in Fig. 4.3. There the Husimi-functions of the left eigenfunctions of U_{open} are compared to those of the right eigenfunctions at the same opening strengths as in Fig. 4.2, $\eta = 10^{-8}$ and $\eta = 1$. Additionally the case of very strong absorption with $\eta = 25$ is shown. The difference of left and right eigenfunctions for weak absorption as well as those of the regular states for strong absorption is exponentially small and thus not visible in this plot. However, for states with high probability in the absorbing region, the chaotic states, the difference becomes obvious for $\eta = 25$.

The computation, leading to Figs. 4.2 and 4.3, is done with the width parameter $\alpha = 0$, where the absorbing region is very large. Even regular states that are very close to this region get trapped in this case. Already for $\alpha = 0.05$ the data looks different. The number of trapped states increases and there are more trapped chaotic states. This results in a non-

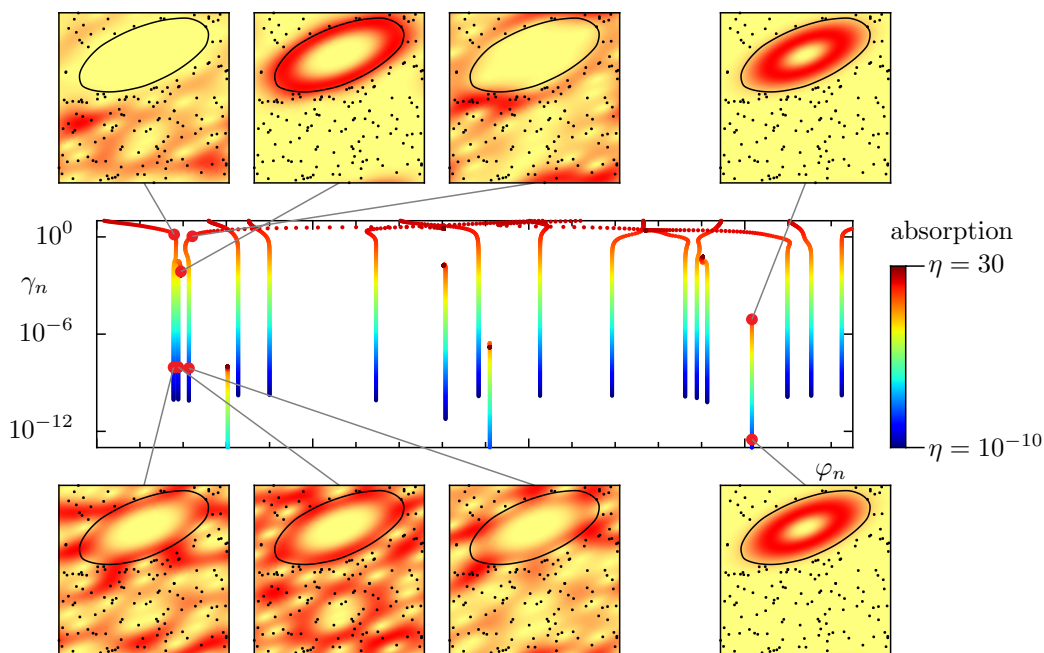


Figure 4.2: Spectrum of eigenvalues in dependence of the opening parameter η for the open quantum map $\mathcal{M}_{\text{open}}$ with $N = 31$, $M_q = 1$, and $\theta_q = 0.7057$. The phase θ_q is fixed at a value for which a maximal saturation value s_{open} occurs. The eigenphase φ is plotted along the x-axis and the escape rate γ along the y-axis. Different opening strengths are encoded with different colors as shown by the color bar with a logarithmic scale. Some resonances are trapped, their decay rate stops to increase with increasing opening η . The Husimi-function of different eigenfunctions are shown in the insets. On the right-hand side a regular state is shown. The Husimi-function is almost unchanged for all openings. The three other resonant states show regular and chaotic components for a small opening. For strong opening one regular state reappears and the other states show almost no regular components.

complete reappearance of regular states. The saturation value s_{open} approaches non-zero values for strong absorption. There are even cases, as shown in Fig. 4.4 (d) with the blue dots, where s_{open} decreases up to a critical opening parameter η and then the saturation value increases again because of the flooding effect due to trapped chaotic states. Hence a large absorbing region, which contains most of the chaotic part of the phase space is needed in order to observe a total reappearance of regular states.

In the following section an analytic understanding of the reappearance effect will be developed. Using a 2×2 matrix model we will demonstrate how two coupled states - a regular and a chaotic one - will decouple due to absorption.

4.1.2 Matrix model

We now construct a 2×2 matrix model to describe the reappearance of regular states. Similar to the discussion in Ref. [27] and in Sec. 3.3.3 we assume a system with one regular state (eigenvalue 0) and one chaotic state (eigenvalue κ) which are coupled via a matrix element v .

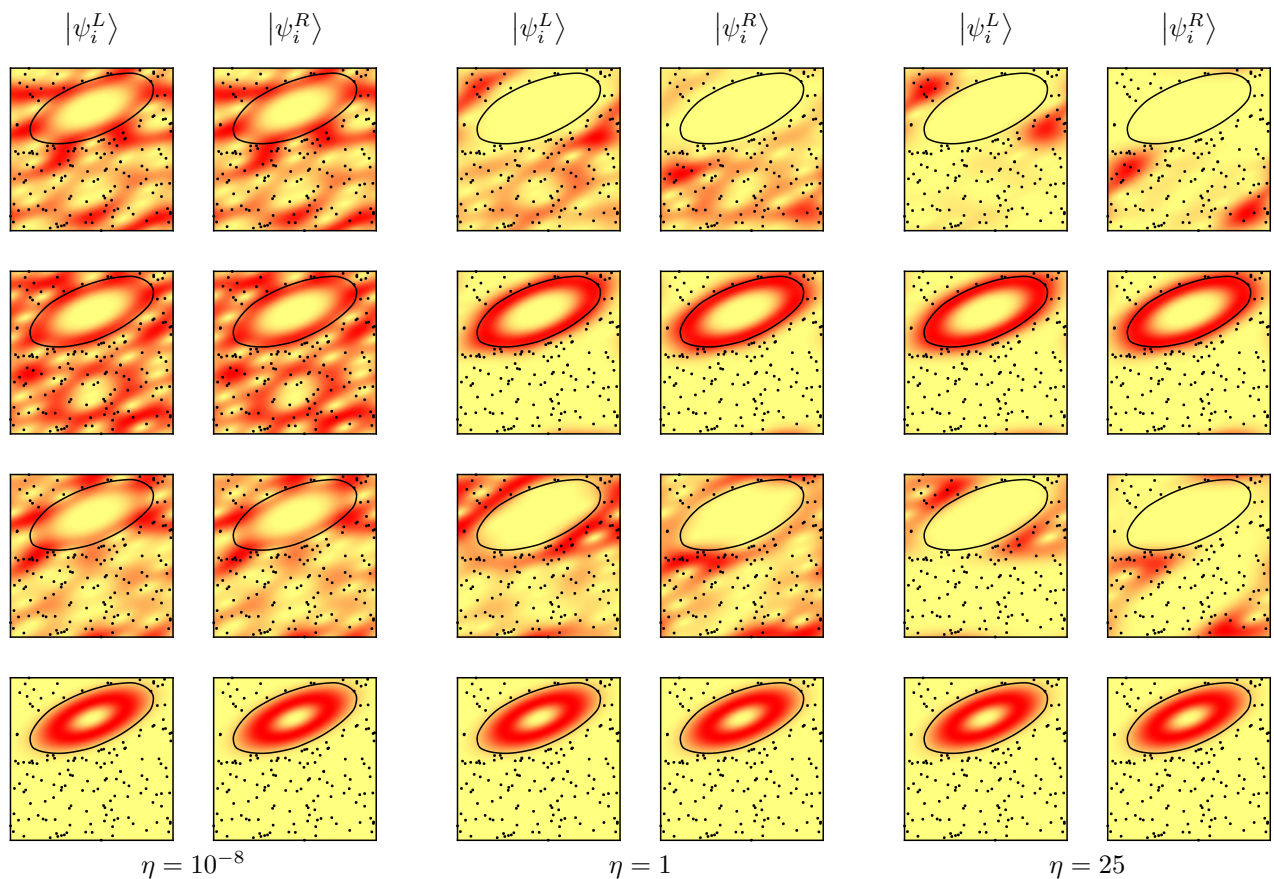


Figure 4.3: Husimi-functions of the left and right eigenfunctions of U_{open} for the same states as in Fig. 4.2. The resonance states are shown for three absorption strengths $\eta = 10^{-8}, 1, 25$. In each case the left column shows the left eigenfunctions and the right column the right eigenfunctions.

Only the chaotic state is coupled to the opening with the absorption strength η using the form of the effective Hamiltonian, Eq. (4.1),

$$H = \begin{pmatrix} \kappa & v \\ v & 0 \end{pmatrix} - \frac{i}{2}\eta \begin{pmatrix} 1 & 0 \\ 0 & 0 \end{pmatrix} . \quad (4.11)$$

For the eigenvalues $\lambda_{1,2}$ we obtain

$$\lambda_{1,2} = \frac{2\kappa - i\eta}{4} \pm \frac{1}{4}\sqrt{(2\kappa - i\eta)^2 + 16v^2} . \quad (4.12)$$

By computing the eigenvectors of Eq. (4.11) and evaluating the saturation values, e.g. Eq. (4.10) without the renormalization, we obtain

$$s_{\text{open}} = 2 \left(1 - \frac{|\lambda_1|^4}{(|\lambda_1|^2 + v^2)^2} - \frac{|\lambda_2|^4}{(|\lambda_2|^2 + v^2)^2} \right) . \quad (4.13)$$

For the qualitative discussion we restrict ourselves to the simple case of $\kappa = 0$ where s_{open} is maximal. This allows to deduce the critical value for the opening, $\eta_{\text{crit}} = 4v$, when the value below the square root in Eq. (4.12) becomes zero. For the behavior of the eigenvalues and saturation values it follows

$$\eta \leq \eta_{\text{crit}} : \quad \begin{aligned} \Im(\lambda_{1,2}) &= -\frac{\eta}{4} \\ s_{\text{open}} &= 1 \end{aligned} , \quad (4.14)$$

$$\eta > \eta_{\text{crit}} : \quad \begin{aligned} \Im(\lambda_{1,2}) &= -\frac{\eta}{4} \pm \frac{1}{4}\sqrt{16v^2 - \eta^2} \\ s_{\text{open}} &= \frac{16v^2}{\eta^2} \end{aligned} . \quad (4.15)$$

The result is visualized in Fig. 4.4 on the left-hand side. For small openings the decay rate of both states increases linearly and the saturation value remains constant at $s_{\text{open}} = 1$. If the opening parameter becomes critical ($\eta = \eta_{\text{crit}}$) we find for the special case of $\kappa = 0$ an abrupt decoupling (blue curves), whereas for $\kappa \neq 0$ the decoupling is smoothed (red curves). The right-hand side of Fig. 4.4 illustrates the same quantities for the three flooded states that are shown in Fig. 4.2. Although three states are involved, we find a qualitatively similar behavior: The blue and the black state are almost degenerate ($\kappa \approx 0$). This leads to a very sharp decoupling at $\eta_{\text{crit}} \approx 0.04$. We can deduce that the coupling matrix element in this case is around $v = \frac{\eta_{\text{crit}}}{4} = 0.01$. Shortly after decoupling from the black state the decay rate starts to increase again for the blue state before the decoupling from the red state takes place. The corresponding coupling matrix element has to be larger than the first one, but the spectral distance of the uncoupled states κ is also larger and the decoupling is smoother. In contrast to the 2×2 model the decay rate of the blue state saturates. The final decay rate corresponds to the regular-to-chaotic tunneling rate of the regular state, as the probability which tunnels to the

chaotic sea immediately ends in the absorbing region. Even the red state becomes trapped and saturates. Although this saturation of decay rates cannot be described by the simple matrix model the reappearance of regular states is well reproduced.

4.2 Experiments in microwave billiards

We verify the reappearance of regular states in microwave experiments. After the investigation of one dimensional systems with quantum maps in the last section we increase the complexity of the problem by using billiards, for which microwave billiards are well suited to study open systems, because we can mimic the imaginary part of the effective Hamiltonian (Eq. (4.1)) by the use of absorbing materials. The measurements were done in collaboration with U. Kuhl and H.-J. Stöckmann in Marburg.

After a short introduction to microwave cavities and their similarity to quantum billiards

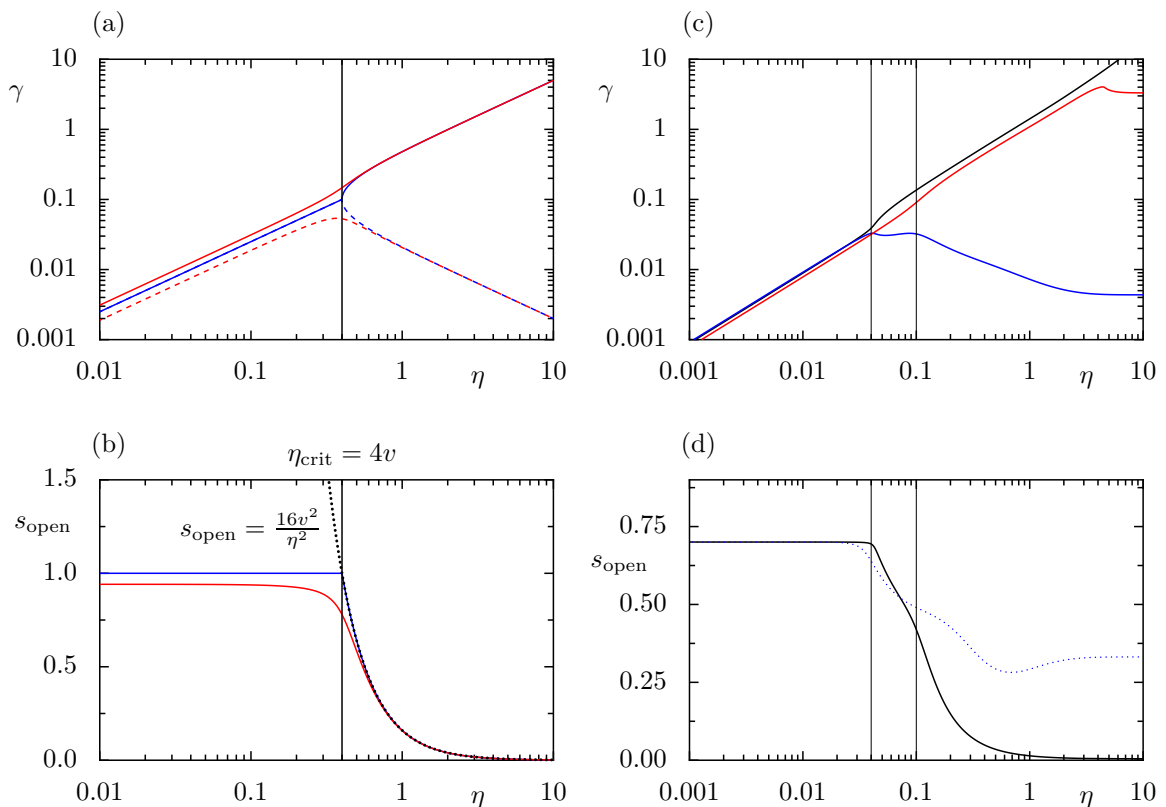


Figure 4.4: Behavior of the decay rates (a) and saturation values (b) for the 2×2 model, Eq. (4.11), in dependence of the opening parameter η . The blue curves show the special case for $\kappa = 0$. The red curves show the smoothed results for $\kappa \neq 0$ but small. The analytic solution for the above-critical ($\eta > \eta_{crit}$) saturation value is shown in dotted black. On the right-hand side the behavior of the decay rates (c) and saturation values s_{open} (d) for the three strongly coupled states from Fig. 4.2 is shown for comparison. In graph (d) the saturation values for the widths parameter $\alpha = 0.05$ is also shown in dotted blue whereas all other data in (c) and (d) is obtained with $\alpha = 0$.

we describe the experimental setup in Sec. 4.2.1 and sketch the analysis of the reflection and transmission data in Sec. 4.2.2. This data is used to construct the wave functions in Sec. 4.2.3. The reappearance of regular states for the mushroom billiard is finally discussed in Sec. 4.2.4.

Microwave measurements give a very good tool to investigate phenomena in quantum chaos. The reason is the similarity of the two dimensional Helmholtz equation to the Schrödinger equation for billiard systems. For cylindrical resonators in two dimensions, we find the Helmholtz equation for the electric field component in z -direction [45, 69]

$$-\left(\frac{\partial^2}{\partial x^2} + \frac{\partial^2}{\partial y^2}\right) E_{z,n} = k_n^2 E_{z,n} . \quad (4.16)$$

Here the height of the resonator has to be smaller than half of the minimal wavelength, such that only transverse magnetic modes exist. The z -component of the electric field E_z is equivalent to the wave function ψ in the Schrödinger equation and obeys the same boundary conditions

$$-\frac{\hbar^2}{2m} \left(\frac{\partial^2}{\partial x^2} + \frac{\partial^2}{\partial y^2}\right) \psi_n = E_n \psi_n \quad (4.17)$$

in units $\hbar = 2m = 1$ with the eigenenergies E_n , which are equal to the square of the wave numbers k_n^2 and the eigenfunctions ψ_n . In the experiment we have to open the system to measure its properties. Thus we insert small antennas into the resonator. The eigenfunctions turn into resonances that are very close to the form of the original wave functions if the coupling of wave functions and the antennas is small enough. The system is best described by the S -matrix. It relates incoming waves a_i to outgoing waves b_j

$$b_j = \sum_i S_{ji} a_i . \quad (4.18)$$

Diagonal elements contain information about the reflection and off-diagonal elements about the transmission. For non-overlapping resonances and point like coupling it is shown in Refs. [69, 70] that the S -matrix follows as

$$S_{ij} = \delta_{ij} - 2i\gamma \bar{G}(r_i, r_j, k) \quad (4.19)$$

with the modified Green's function

$$\bar{G}(r_i, r_j, k) = \sum_n \frac{\psi_n(r_i)\psi_n(r_j)}{k^2 - k_n^2 + i\gamma \sum_l |\psi_n(r_l)|^2} . \quad (4.20)$$

The parameter γ describes a broadening of resonances due to the coupling to the antennas and the absorption in not ideally conduction walls. Apart from that the Green's-function contains all the information about the system. The wave number k is related to the frequency ν

$$k = 2\pi \frac{\nu}{c} . \quad (4.21)$$

Thus we measure the frequency dependent reflection and transmission for two antennas to obtain the S -matrix.

4.2.1 Experimental setup

Fig. 4.5 shows the setup of the experiment. A microwave resonator (Fig. 4.6) is pressed against the top plate (1) with an elevating device (3). The data was measured with two antennas, one movable along the two dimensions of the table (2) and the second is fixed in the resonator from the downside of the table. The moving antenna is shifted by servo motors (4) and can be controlled by a serial interface (5) from a personal computer (PC). Details on the antenna positioning are discussed in App. D. The top plate contains a grid of holes every 5 mm to insert the antenna (2) into the cavity. The antennas are connected to a vector network analyzer that is also controlled and read out by the PC. The form of the resonator is shown in Fig. 4.6. The cavity has the shape of a desymmetrized mushroom billiard that is also discussed numerically in Sec. 3.6. The cavity is closed by the top plate of the table and the dimensions are listed in Tab. 4.1. The vector network analyzer acquires the amplitude and phase of all four possible channels that are the reflection in both antennas and the transmission in both directions. For the wave function measurements only two channels were used to save memory and measurement time. We determine the reflection of the moving antenna and the transmission to the fixed antenna.

4.2.2 Transmission and reflection measurements

In Fig. 4.7 the data of one specific arrangement of the antennas is shown. The graph illustrates the modulus of the reflection and the modulus, the real part, and the imaginary part of the transmission under variation of the frequency. We find resonances at the negative peaks in the reflection data and at peaks in the transmission measurement that is shown in a small frequency range. The total frequency range starts at 0.5 GHz and reaches up to 14.9 GHz with a resolution of 1 MHz.

The measurable width of the resonances is comparably large with about $\Delta\nu \approx 20 - 30$ MHz (see e.g. Refs. [71,72]). One reason for broad resonance is the size of the resonator, which results in a large surface that absorbs the microwaves. However, especially the large stem height l of

| | | |
|----------------------|-----|--------|
| radius of the cap | R | 300 mm |
| length of the stem | l | 700 mm |
| width of the stem | a | 210 mm |
| height of the cavity | h | 10 mm |

Table 4.1: Dimensions of the mushroom billiard cavity shown in Fig. 4.6.

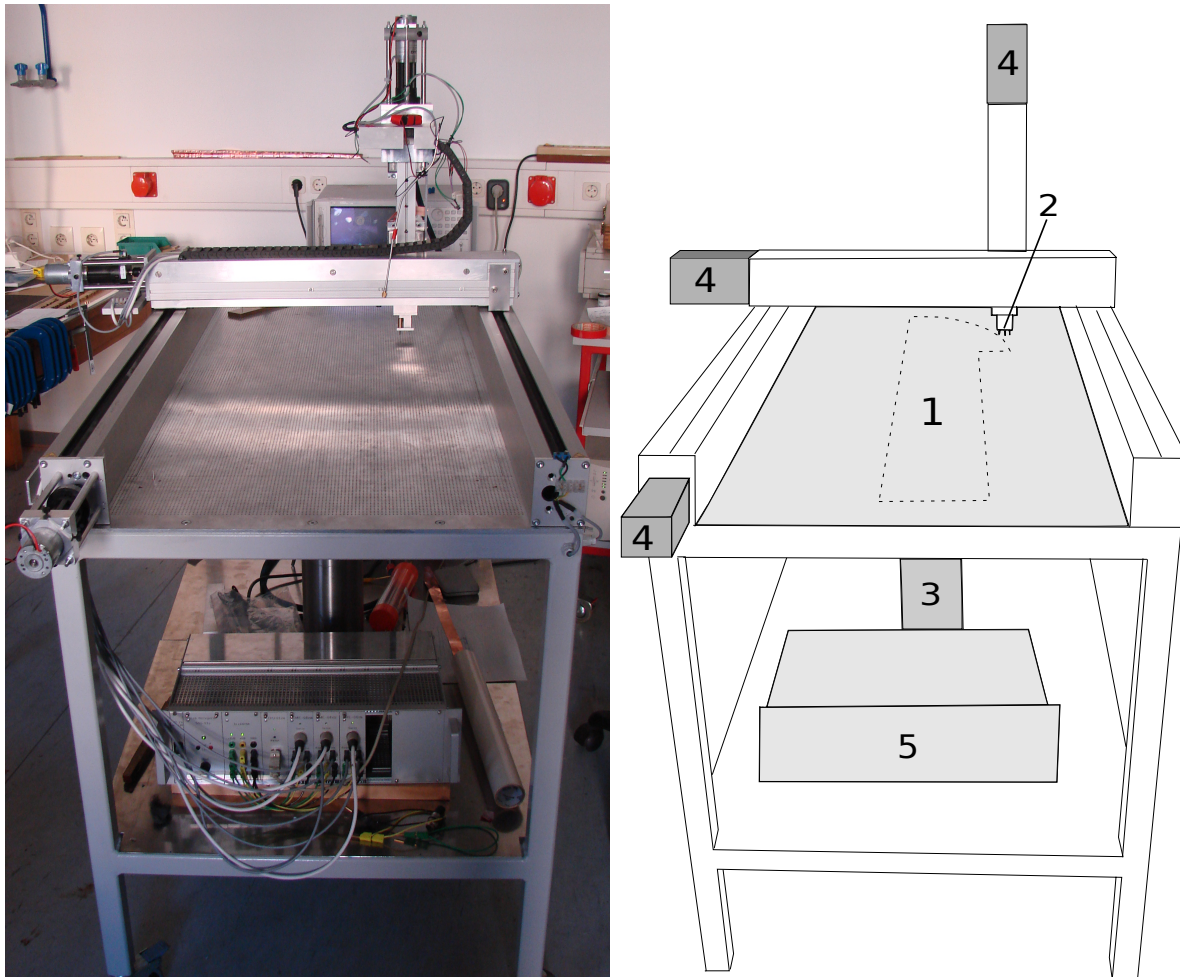


Figure 4.5: Experimental setup: The microwave resonator is pressed against the top plate of the table (1) with an elevating device (3). The first antenna (2) is movable via servo motors (4) along all dimensions. The top plate contains a grid of holes every 5 mm to insert the antenna into the cavity. The motion is controlled by the unit (5) that is connected to a PC. A second antenna is fixed on the lower plate of the resonator that is show in Fig. 4.6. The measurement is done via a vector network analyzer that is linked to the PC and both antennas.

the cavity is required, since high saturation values in the mushroom billiard occur if the density of states in the chaotic sea is high (see Sec. 3.6). And another reason is the flexible construction of the resonator that allows for fast opening to insert absorbing material as shown in Fig. 4.6. Therefore the top plate is not fixed with screws to the resonator. Unavoidably, there are small gaps in the connection of both aluminum plates, which are easily passed by microwaves of the 0-th mode in z -direction. In experiments with superconducting materials such losses would be almost zero but the effort and cost would also increase drastically [32]. However, the flexibility to modify the geometry or insert absorbing material would be lost.

A calibration of the antennas is necessary to compensate the frequency dependent response of the reflection in the cables, at the connections, and the antenna itself. Deformations of the cable or loosening of connections during the automatic movement of the first antenna are

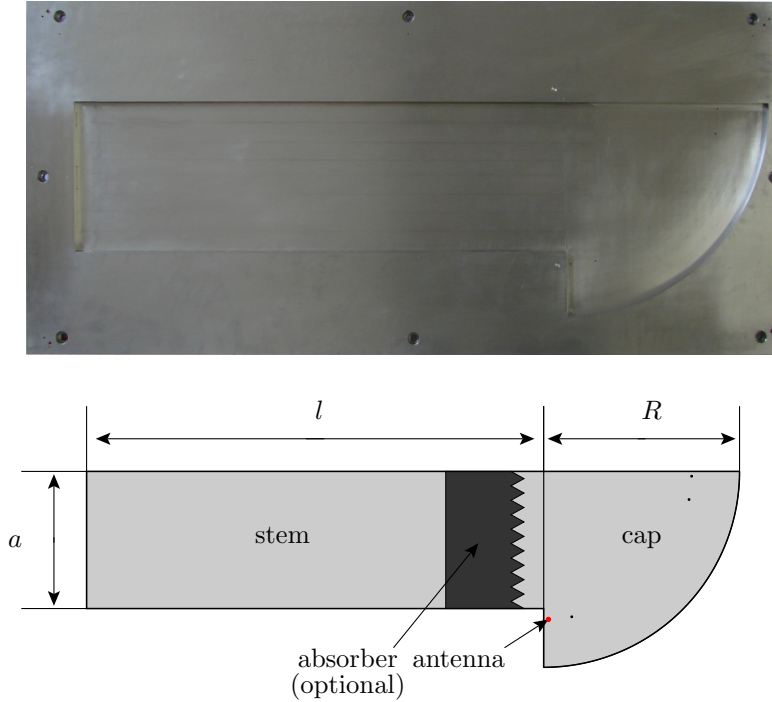


Figure 4.6: Mushroom shaped microwave resonator. The dimensions are shown in Tab. 4.1. The four small holes in the resonator mark the possible positions for the second antenna. They are also displayed as black or red dots in the drawing below. For all wave function measurements the red marked antenna position was used. An absorbing material can be put in the stem to open the cavity in the chaotic part of the phase space. To avoid direct back reflection the absorber has a zig-zag shape.

possible sources for errors in the measured data. This antenna is inserted through a 2 mm hole in the top plate. The alignment within that hole, which causes varying capacities, and altering contact resistance to the top plate leads to non-uniform couplings to the resonator at different measurement positions. These experimental constraints strongly influence the quality of the wave functions, which we can construct from the S -matrix. The reflection measurement is especially sensitive to this type of errors because the point of reference is one in this case (see Eq. (4.19)).

4.2.3 Wave functions measurements

Using Eq. (4.19) we can reconstruct the wave function data from the measured S -matrix channels

$$\delta_{ij} - S_{ij}(r_i, r_j, k) \propto \sum_n \frac{\psi_n(r_i)\psi_n(r_j)}{k^2 - k_n^2 + i\gamma \sum_l |\psi_n(r_l)|^2} . \quad (4.22)$$

The reflection coefficient S_{11} can be used to determine the modulus squared of a wave function $|\psi(r_1)|^2$

$$|\psi_n(r_1)|^2 \propto |1 - S_{11}(r_1, r_1, k_n)| \quad (4.23)$$

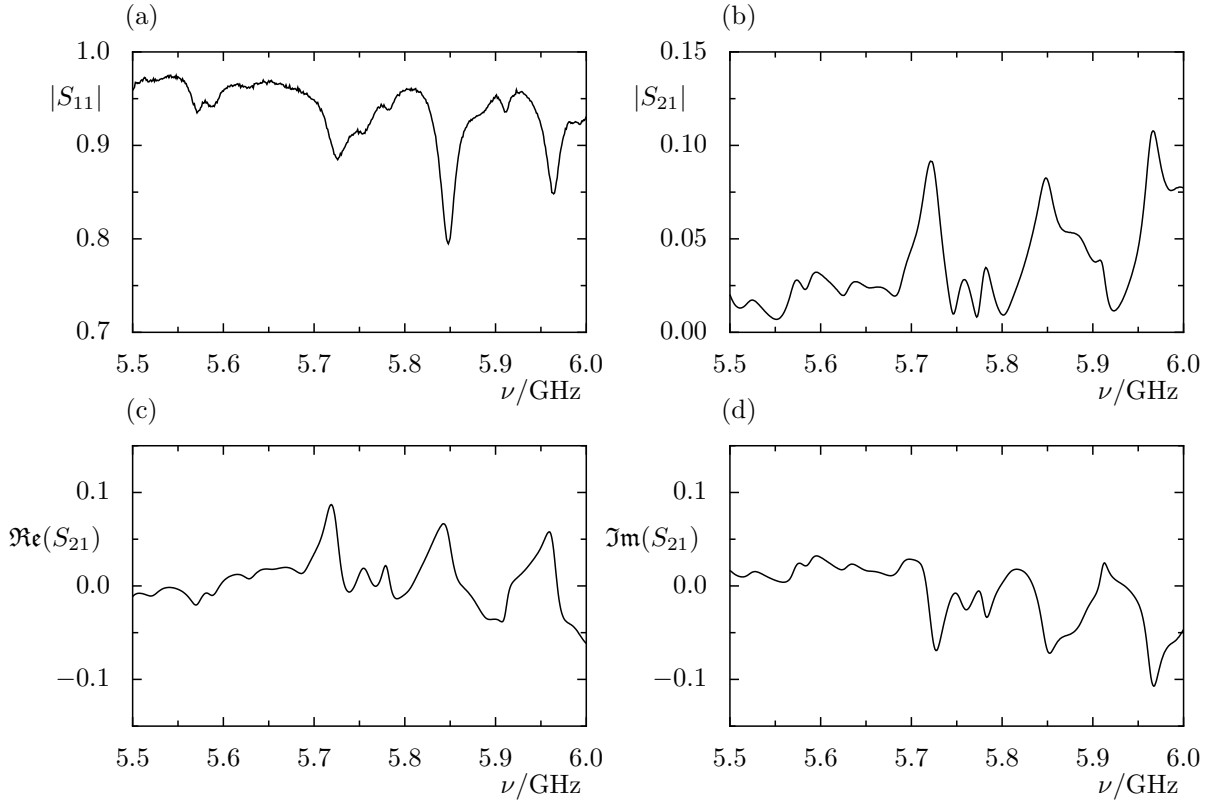


Figure 4.7: Reflection and transmission data of the mushroom microwave experiment. The modulus of the reflection is shown in (a), whereas the other graphs illustrate the transmission data for the same antenna positions, as the modulus (b), real part (c), and imaginary part (d).

at a certain frequency $\nu_n = \frac{k_n c}{2\pi}$, which ideally is a resonance frequency. Due to absorption and openings in the resonator cavity, this resonance frequency is shifted to lower frequencies in most cases. This data is very sensitive to errors, because, as shown in Fig. 4.7 (a), the modulus of the reflection coefficient is of the order of one $|S_{11}| \approx 1$. Thus small relative errors in S_{11} lead to large relative errors in the wave function $|\psi(r_1)|^2$.

The transmission measurement yields the wave function with amplitude and phase information (Eq. (4.22))

$$\psi_n(r_1) \propto S_{21}(r_2, r_1, k_n) \propto \frac{\psi_n(r_2)\psi_n(r_1)}{\sum_l |\psi_n(r_l)|^2} . \quad (4.24)$$

This quantity is much more stable against measurement errors due to the lack of subtraction in the formula. To use this efficiently, one has to choose a good position of the fixed antenna. Wave functions that have a nodal line ($\psi(r_2) = 0$) at that position are invisible in the transmission and the amplitude of the resonances is strongly influenced by this position. The coordinates of the fixed antenna was chosen such that regular wave functions near the border of the stem have a high probability. To find these coordinates we maximized the product $w(x, y)$ of the

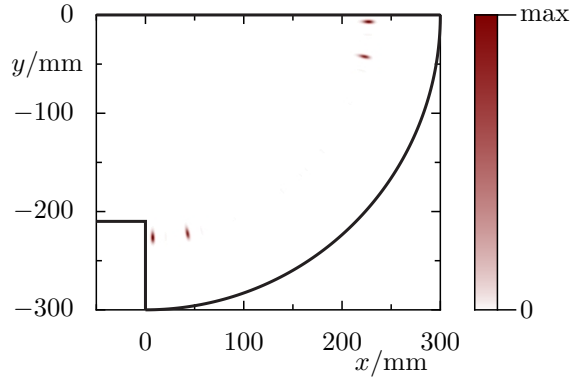


Figure 4.8: Product of the probability distributions of regular wave functions with high saturation values (see Eq. (4.25)). A list of the quantum numbers of the regular wave functions used for this quantity is shown in Tab. 4.2.

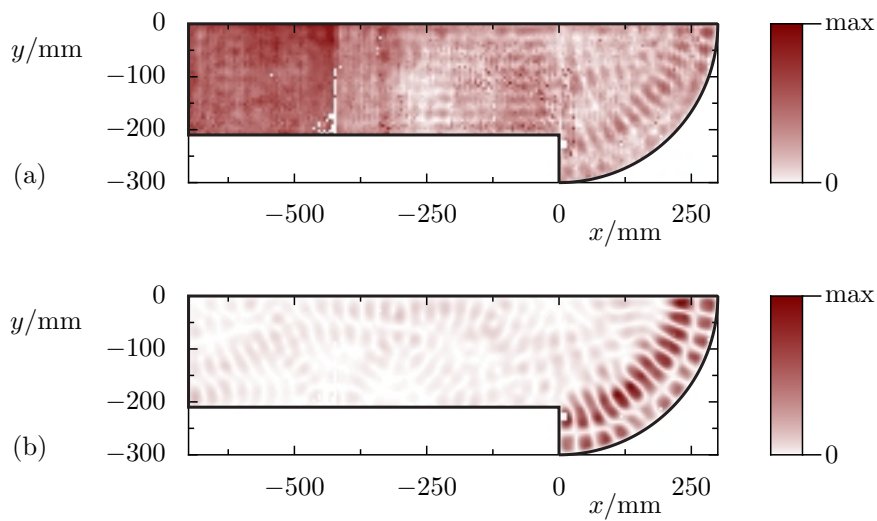


Figure 4.9: Wave function data $|\psi|^2$ reconstructed from the reflection (a) and transmission data (b). The frequency is 5.816 GHz.

probability distributions of those regular states $\chi_{\text{reg}}^{(n,m)}$, which have high saturation values

$$w(x, y) = \prod_{(n,m) \in \mathfrak{F}} |\chi_{\text{reg}}^{(n,m)}(x, y)|^2 . \quad (4.25)$$

Here \mathfrak{F} represents the set of strongly flooded states. The function $w(x, y)$ is shown in Fig. 4.8 and we find four optimal positions for the fixed antenna, which therefore were chosen in the experiment (Fig. 4.6).

A list of all these states is shown in Tab. 4.2 together with the approximate saturation values s calculated with the mean density of states and the analytic tunneling rate (see Sec. 3.6). The last column shows the non-averaged saturation values s_{open} for a numerical calibration of eigenfunctions using the same setup. We expect the wave functions in the experiment to be good approximations for eigenfunctions. However, small changes in the geometry, such as fabrication errors, lead to changing saturation values. Thus the values listed in Tab. 4.2 serve

as a guide for the experiment.

In Fig. 4.9 an example wave function $|\psi|^2$ constructed from the reflection (a) and transmission data (b) at 5.816 GHz is shown. In contrast to the reflection data (a), which is very noisy, the transmission data (b) shows a clear pattern of a flooded regular state with regular components in the cap and chaotic components in the stem.

However the assumption of well separated resonances is not justified in this measurement. The density of states is higher than the averaged width of resonances. For example at 6 GHz the density of states translates to a frequency level distance of about 11 MHz compared to the resonance width of about 20 MHz. Hence, we have to keep in mind that all wave function data we show in the following are superpositions of several wave functions of the closed billiard. Also additional effects due to the nonlinear coupling of different resonances may arise. Fortunately the selection in the transmission data, due to the position of the fixed antenna, reduces the number of visible states. Thus those problems are much less relevant for the transmission measurements.

At some points the moving antenna was not completely connected to the resonator. These points are disregarded in the following. The number of disregarded points is small compared to number of measured data points (less than 1% for all measurements), see Tab. 4.3. In the following we discuss two different measurements. The first is the mushroom cavity without any absorbing material that will be referred to as closed mushroom. The second is the open mushroom where absorbing material is prepared in the stem of the mushroom.

In order to get the right phases for the complex wave functions we have to remove further correlations from the data ψ' as in Refs. [69, 73]

$$\psi = e^{-i\varphi_{g,0}} \psi' \quad (4.26)$$

| quantum numbers (n, m) | saturation values s | numerical saturation values s_{open} |
|--------------------------|-----------------------|---|
| (2, 26) | 67% | 51% |
| (2, 28) | 61% | 32% |
| (3, 40) | 73% | 57% |
| (3, 42) | 67% | 65% |
| (3, 44) | 62% | 23% |
| (4, 54) | 76% | 57% |
| (4, 56) | 72% | 66% |
| (4, 58) | 67% | 68% |
| (4, 60) | 62% | 32% |

Table 4.2: Table of regular states with high saturation values s . The numerical calibration of eigenfunctions for the same billiard setup yields the last column of non-averaged saturation values s_{open} .

| measurement | number of data points | error points |
|-----------------|-----------------------|--------------|
| closed mushroom | 8669 | 60 |
| open mushroom | 2873 | 24 |

Table 4.3: Number of measured data points for the moving antenna for all billiard realizations. The number of error points is given as well.

with the global phase $\varphi_{g,0}$

$$\varphi_{g,0} = \frac{1}{2} \arctan \left(\frac{2\langle \Re(\psi)\Im(\psi) \rangle_{\Omega}}{\langle \Re(\psi)^2 \rangle_{\Omega} - \langle \Im(\psi)^2 \rangle_{\Omega}} \right). \quad (4.27)$$

The average is meant as a spatial average over the whole measurement area Ω , which in this context is an average over all data points. In Fig. 4.10 the effect of the correlation correction can be seen. The first graph (a) shows the imaginary versus the real part of the wave function data collected from all grid points at 5.845 GHz. The real and imaginary part is clearly correlated and the data is not concentrated along the real axis. The correction, Eq. (4.26), by the phase $e^{-i\varphi_{g,0}}$ ensures that the main contribution is along the real axis as can be seen in (b). We also get a measure for the opening of the system via the phase rigidity $|\rho|^2$ [74] with

$$\rho = \frac{\int_{\Omega} dx dy \psi^2}{\int_{\Omega} dx dy |\psi|^2} = \frac{\langle \Re(\psi)^2 \rangle_{\Omega} - \langle \Im(\psi)^2 \rangle_{\Omega}}{\langle \Re(\psi)^2 \rangle_{\Omega} + \langle \Im(\psi)^2 \rangle_{\Omega}}. \quad (4.28)$$

The phase rigidity $|\rho|^2$ is one for systems with time reversal symmetry and zero in system where that symmetry is broken. The only physical reason for time reversal symmetry breaking in the mushroom billiard without magnetic field is dissipation. Fig. 4.10 (c) shows the phase rigidity $|\rho|^2$ around 5.8 GHz for a regular state with quantum numbers $n = 2, m = 26$. The black curve illustrates $|\rho|^2$ for the closed mushroom, whereas the blue curve is for the open mushroom. In Fig. 4.10(d) the regular overlap, which indicates the amount of regular weight in the wave function, is shown in comparison. In both measurements the phase rigidity $|\rho|^2$ has a maximum at the frequency with the highest regular overlap. There are no cases where the phase rigidity reaches one because of the dissipation that we already discussed. Between resonances the value $|\rho|^2$ decreases. For the open mushroom measurement the phase rigidity is concentrated around the eigenfrequency of the regular state, whereas we find several peaks in the closed mushroom measurement. This already indicates that chaotic states are affected stronger by the absorption than the regular states.

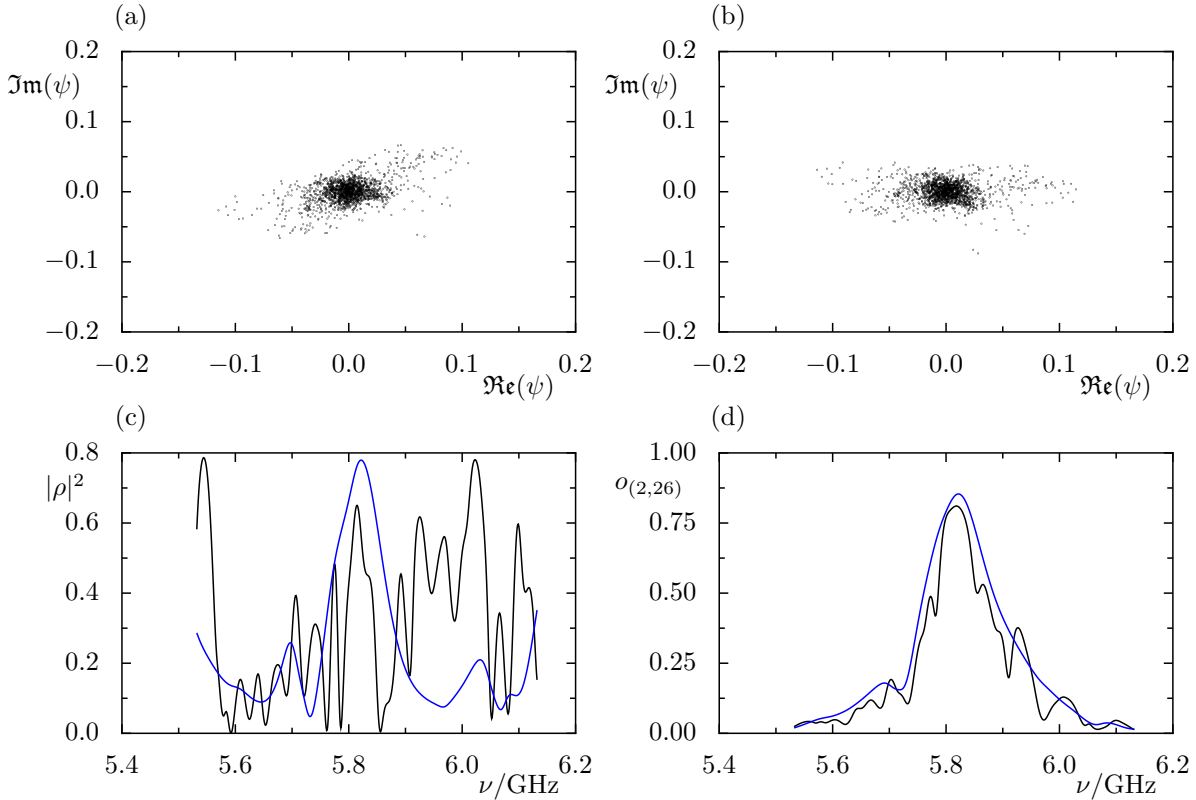


Figure 4.10: Distribution of the complex wave function data before (a) and after correlation correction (b) for the closed mushroom at 5.845 GHz. The phase rigidity around the regular state with quantum numbers $n = 2, m = 26$ is plotted (c) in comparison to the regular overlap (d) for both measurements. The closed mushroom is shown in black and the open mushroom in blue.

4.2.4 Reappearance of regular states

We want to study if signatures of the reappearance of regular states can be found in microwave experiments using the mushroom billiard. A promising quantity is the overlap of all eigenfunctions with a regular state of interest $\chi_{\text{reg}}^{(n,m)}(x, y)$

$$p_{\psi}^{\text{reg}} = \left| \int_{\Omega} dx dy \psi(x, y) \chi_{\text{reg}}^{(n,m)}(x, y) \right|^2. \quad (4.29)$$

The purely regular states in the mushroom billiard are given explicitly by the eigenfunctions of the circular mushroom billiard, see Eq. (3.97). The regular overlap can be used to compute the saturation values s_{open}

$$s_{\text{open}} = 1 - \sum_n |p_{\psi_n}^{\text{reg}}|^2. \quad (4.30)$$

We cannot isolate single eigenfunctions ψ_n with this experiment. Thus we approximate the sum by an integral over all frequencies. This works at least for the closed mushroom, as the wave functions reconstructed via the transmission data can be normalized over the whole resonator.

Even then the position of the fixed antenna leads to a non-uniform weighting of different resonances. For the open mushroom, however, only grid points in the cap were measured and in addition the absorption introduces outgoing waves in the stem. In this case it is not possible to normalize the wave functions.

Thus we are aiming at a more qualitative argument than in Sec. 4.1 and compare the wave function properties of the open and the closed mushroom without normalization. Instead we scale all amplitudes such that

$$\int_{\Omega_{\text{cap}}} dx dy |\psi(x, y)|^2 = 1 \quad , \quad (4.31)$$

holds, where we integrate over the area of the quarter circular cap of the mushroom Ω_{cap} . For purely regular states this rescaling is equivalent to a normalization, because the probability in the stem is zero. Then we define a regular overlap $o_{(n,m)}$ which is evaluated with all data points in the cap

$$o_{(n,m)} = \left| \int_{\Omega_{\text{cap}}} dx dy \psi(x, y) \chi_{\text{reg}}^{(n,m)}(x, y) \right|^2 . \quad (4.32)$$

The overlap, which depends on the frequency via the wave function, cannot be interpreted as a probability measure. But it can be used to find the frequency with the highest regular weight. Although we know the resonance frequency of each regular state analytically, in the experiment this resonance is shifted due to the opening. This overlap is shown in Fig. 4.11 together with the corresponding wave functions for two different regular states. The frequency for the wave functions is determined by the maximal regular overlap. For the closed mushroom $o_{(n,m)}$ is plotted in black with the wave functions (b) and (e) whereas for the open mushroom $o_{(n,m)}$ is plotted in blue with the wave functions (c) and (f). Although the overlap is not much different for both measurements, the wave functions show slightly different qualitative behavior in the cap. The region in the cap, given by a quarter circle with a radius equal to width of the stem ($\rho = a$), contains only exponentially small contributions of the regular states. They concentrate on classical regular trajectories that are within the region with radius $\rho > a$. In the part with $\rho < a$ chaotic components of the wave functions are visible. The more chaotic components a wave function has the larger the probability is in the quarter circle with smaller radii ($\rho < a$). This does not change for mixtures of eigenfunctions as observed in the experiment. We define a cap probability ratio $p_{\text{cap}}(\rho)$

$$p_{\text{cap}}(\rho) = \frac{R^2}{\rho^2} \int_0^\rho d\rho' \int_{-\frac{\pi}{2}}^0 d\varphi |\psi(\rho', \varphi)|^2 \quad , \quad (4.33)$$

where we integrate over Ω_{cap}^ρ , a quarter circle with radius ρ in the cap shown in Fig. 4.12, and compare to the probability of a uniform distribution $u(x, y) = \frac{4}{\pi R^2}$ in the same region. By

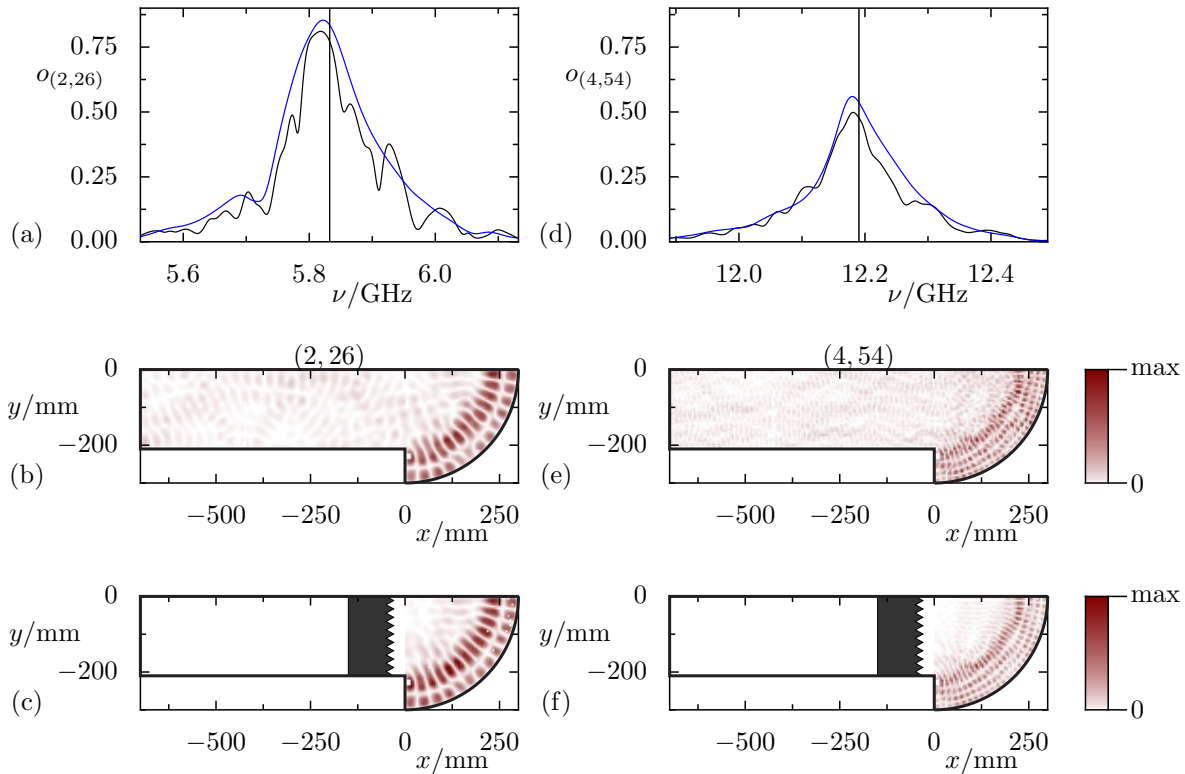


Figure 4.11: Regular overlap (Eq. (4.32)) with the state of quantum numbers $n = 2, m = 26$ (a) and $n = 4, m = 54$ (d) for the closed and open mushroom in black and for open mushroom in blue. The analytic resonance frequencies are marked as vertical lines. For the frequency with the maximal overlap corresponding wave functions $|\psi|^2$ reconstructed from the transmission data is shown below each overlap graph. The plots (b) and (e) illustrate the closed mushroom measurement whereas plots (c) and (f) show the open measurement with absorbing material in the stem.

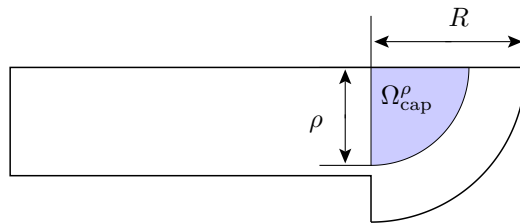


Figure 4.12: Integration area used in Eq. (4.33).

means of the scaling condition Eq. (4.31), the cap probability ratio is one for $\rho = R$. This quantity allows to distinguish regular and chaotic states especially for small radii ($\rho < a$), where we find almost no probability for regular states $p_{\text{cap}}(\rho < a) \approx 0$ and a high probability for chaotic states $p_{\text{cap}}(\rho < a) \geq 1$. In Fig. 4.13 $p_{\text{cap}}(\rho)$ is shown for the wave function at the frequency with maximal regular overlap for two different regular states. As a reference the cap probability for the corresponding regular state is marked in red. At small radii for the closed mushroom measurement (black) we find much higher cap probability ratios $p_{\text{cap}}(\rho)$ than for the open measurement (blue). The chaotic components are suppressed in both cases, but the

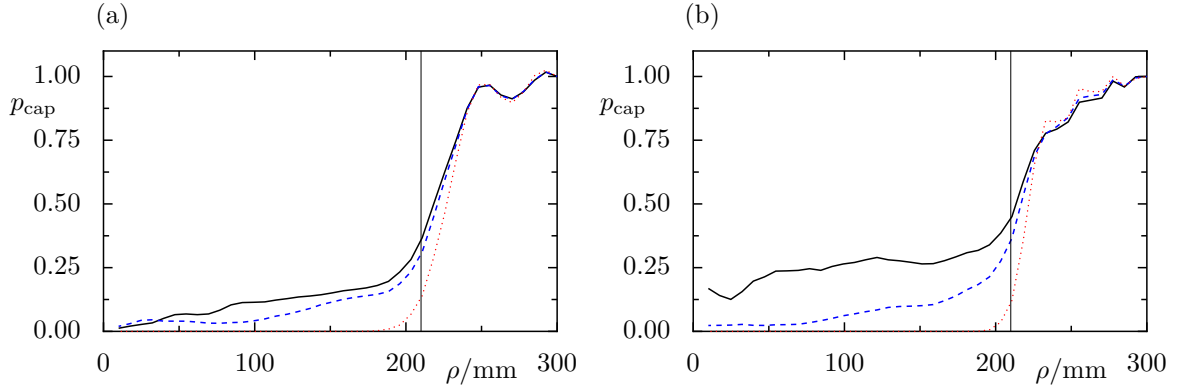


Figure 4.13: Integrated cap probability p_{cap} (Eq. (4.33)) at the frequency with maximum regular overlap $o_{(n,m)}$ for the regular state with quantum numbers $n = 2, m = 26$ (a) and $n = 4, m = 54$ (b). This quantity is shown for a regular state $\chi_{\text{reg}}^{(n,m)}$ in red compared to the closed mushroom data in black and the open mushroom data in blue.

difference of the blue and the black curve is much larger for $(n = 4, m = 54)$.

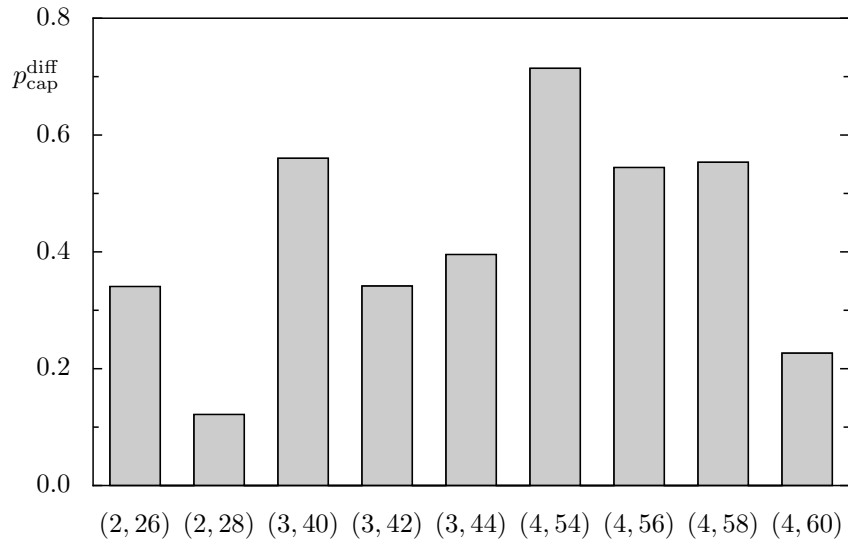


Figure 4.14: Differences $p_{\text{cap}}^{\text{diff}}$ of the integrated cap probability (4.34) for all regular states, which are listed in Tab. 4.2 together with the approximate saturation values. Under each bar the quantum numbers of the corresponding regular state are shown. Values of $p_{\text{cap}}^{\text{diff}}$ near one correspond to full reappearance of a flooded regular state.

A quantitative measure is $p_{\text{cap}}^{\text{diff}}$

$$p_{\text{cap}}^{\text{diff}} = \frac{\langle p_{\text{cap}}^{\text{closed}}(\rho) - p_{\text{cap}}^{\text{open}}(\rho) \rangle_{\rho < \rho_{\text{max}}}}{\langle p_{\text{cap}}^{\text{closed}}(\rho) \rangle_{\rho < \rho_{\text{max}}}}, \quad (4.34)$$

where we average the difference of the closed mushroom $p_{\text{cap}}^{\text{closed}}(\rho)$ and the open mushroom $p_{\text{cap}}^{\text{open}}(\rho)$ for radii smaller $\rho_{\text{max}} = 190$ mm. The maximal radius is chosen smaller than the stem

width a because of non-zero cap probability ratios for a regular state $p_{\text{cap}}(a = 210 \text{ mm}) \neq 0$ (Fig. 4.13 (a)). This relative difference $p_{\text{cap}}^{\text{diff}}$ can be positive if the chaotic components are suppressed by adding absorbing material or negative in the opposite case. A flooded regular state which reappears completely when opening the system yields a relative difference $p_{\text{cap}}^{\text{diff}} \approx 1$, because in the open mushroom the cap probability ratio $p_{\text{cap}}^{\text{open}}(\rho < a)$ is almost zero. Fig. 4.14 shows $p_{\text{cap}}^{\text{diff}}$ for all regular states which are listed in Tab. 4.14. In all cases we find reduced chaotic components in the open mushroom. Although we do not observe complete reappearance $p_{\text{cap}}^{\text{diff}} \approx 1$, due to mixing of eigenfunctions with overlapping resonances, the reappearance effect is clearly visible in the mushroom billiard experiments.

5 Summary and outlook

For systems with a mixed phase space one can construct regular states, which concentrate on classical tori in the regular island. However, due to dynamical tunneling these regular states are coupled to chaotic states. For strong coupling the regular island is flooded. In this thesis the flooding of regular states is investigated by means of the time evolution of wave packets initially started in the chaotic sea. The probability in the regular island is studied by extensive numerical simulations. For this purpose the projection onto regular states turns out to be an ideal measure of regular weights.

Three qualitative regimes are found in the time evolution simulations: a linear regime at small times, a saturation regime at large times, and a transition regime with oscillations between the linear and the saturation regime. For the first regime the linearly increasing regular weights are explained by dynamical tunneling from the chaotic sea to the regular island. For large times the weights saturate. A universal scaling of the saturation plateaus is found by introducing an effective coupling, which combines the information about the tunneling rates and the density of states in the system. This scaling remains unchanged if the system size, the effective Planck constant, or the tunneling rates are varied. The same behavior is found for two-dimensional billiard systems, for which the mushroom billiard is studied as an example.

The height of the saturation plateaus can be described by a random matrix model under consideration of the transport behavior in the regular island. Already a 2×2 matrix model, which is analytically solvable, is sufficient to predict the complete universal scaling of the saturation plateaus quantitatively. The analytic solution for the height of the plateaus s in dependence of the effective coupling v is given by

$$s = 2v \arctan \frac{1}{2v} . \quad (5.1)$$

The flooding mechanism is excellently described by this formula in all considered numerical simulations including quantum maps with different system sizes and transport behaviors as well as two-dimensional billiard systems. Even the full time-dependent behavior of the regular weights is reproduced for small couplings, which leads to a detailed understanding of the time evolution of wave packets in systems with flooded states including the oscillations of the transition regime between the linear increase and the saturation regime.

Although all results rely strongly on spectral averaging the same qualitative behavior is found for the standard map, where only a limited spectral variation is possible. In that case

the description using the effective coupling fails, because only a small number of chaotic states couple to regular states. Thus, spectral fluctuations govern the amount of flooding in such systems. By identifying the chaotic states involved in the coupling to the regular states and determining the corresponding coupling strengths, the behavior of the regular weights can also be modeled in this case.

To understand the influence of flooding in open quantum systems we consider quantum maps, where absorption is introduced in the chaotic part of phase space. By controlling the strength of the absorption, the complete transition from a closed system with flooded states to a fully open quantum system is studied. For a strong opening we find the reappearance of regular states. Only the chaotic states are coupled strongly to the opening and at some critical value of the absorption the flooded states, which are linear combinations of regular and chaotic states, decompose into purely regular and chaotic states. This can be understood by the phenomenon called resonance trapping, which occurs in open quantum systems. The escape rate of flooded states increases with increasing absorption in the chaotic sea. At a critical opening strength the escape rate of the regular states, which start to reappear, changes the monotonic behavior and decreases when further opening of the system. The value of the critical absorption depends on the coupling matrix elements of the regular state and the chaotic states, which are often used for theoretical descriptions. For some systems these matrix elements are difficult to determine, although the variance of all coupling matrix elements can be deduced from the tunneling rates. To compute the coupling to a single chaotic state one has to do spectral variations and measure the width of avoided crossings. This procedure can lead to changes of system parameters, which influence also the coupling. In these cases one could compare the opening characteristic of the system to the matrix models used to describe the reappearance and deduce the coupling strength from the critical opening strength.

In this thesis we present the first experiment on flooding and the reappearance of regular states using a microwave resonator, which has the shape of a mushroom. The microwave transmission patterns for this mushroom billiard were measured, which allows to reconstruct wave function data for this geometry. By inserting absorbing material in the resonator the system is opened and the comparison of the wave functions for open and closed measurement yields decreasing chaotic components in the open mushroom. Thus the reappearance of regular states is verified experimentally.

In the future the results of this thesis may help to understand the quantum mechanical influence of partial barriers in phase space. In such systems already a classical transport between different phase space regions is present. Depending on size of the effective Planck cell compared to the classical flux through the barrier the influence on the corresponding quantum system changes [42, 75, 76]. Also in higher dimensional systems, where due to Arnold diffusion the regular islands are classically not completely isolated from the chaotic sea, the flooding effect will be an interesting subject for future studies. A first indication, that flooding is especially

important in higher dimensional systems, is given in Ref. [77].

Continuing the work on the behavior of the conductance in nanowires with one sided surface roughness [24, 25], new applications of flooding in open quantum systems may be found. Furthermore, the knowledge of the reappearance of regular states is important to understand experimental results in such systems. A possible application are open optical microcavities [78], where the behavior of the resonance states influences the far-field emission pattern. As a first step the opening in the chaotic part of the phase space is understood, but in many experiments also the regular region is absorbing, e.g. due to losses by the imperfect reflection of walls in billiard systems. Using the results of this thesis it will be easier to recognize the flooding mechanism and its consequences in many applications in the field of quantum chaos.

A Classical and quantum kicked systems

A.1 System-adapted units

We introduce system-adapted units using the Hamiltonian of the kicked rotor in SI units as an example

$$\tilde{H}(\Theta, I) = \frac{I^2}{2mr^2} + rP \cos \Theta \sum_{n \in \mathbb{Z}} \delta(\tilde{t} - n\tau) \quad , \quad (\text{A.1})$$

where I is the angular momentum of a point mass m rotating at radius r , which is kicked periodically at times $n\tau$ with momentum P . The angle of the rotor is given by Θ . Each physical variable in this system is rescaled with a typical value. Thus all physical quantities are evaluated in multiples of these typical system values. The typical angle is a full circle $\Theta_0 = 2\pi$ and the typical time is the driving period τ . Furthermore we choose the angular momentum $I_0 = \frac{2\pi mr^2}{\tau}$, which corresponds to an angular velocity of one rotation per kicking period τ . All other quantities can be deduced using the previous typical variables. Thus one obtains a typical energy $V_0 = \frac{\Theta_0 I_0}{\tau} = \frac{(2\pi)^2 mr^2}{\tau^2}$ and the rescaled Hamiltonian H

$$H = \frac{\tilde{H}}{V_0} = \frac{I^2}{2mr^2 V_0} + \frac{rP}{V_0} \cos \frac{2\pi\Theta}{2\pi} \sum_{n \in \mathbb{Z}} \delta(\tilde{t} - n\tau) \quad (\text{A.2})$$

$$= \frac{I^2 \tau^2}{8m^2 \pi^2 r^4} + \frac{P \tau^2}{mr(2\pi)^2} \cos \frac{2\pi\Theta}{\Theta_0} \sum_{n \in \mathbb{Z}} \frac{1}{\tau} \delta\left(\frac{\tilde{t}}{\tau} - n\right) \quad (\text{A.3})$$

$$= \frac{I^2}{2I_0} + \frac{P\tau}{mr(2\pi)^2} \cos(2\pi q) \sum_{n \in \mathbb{Z}} \delta(t - n) \quad (\text{A.4})$$

$$= \frac{p^2}{2} + \frac{k}{(2\pi)^2} \cos(2\pi q) \sum_{n \in \mathbb{Z}} \delta(t - n) \quad , \quad (\text{A.5})$$

where p is the rescaled momentum $p = \frac{I}{I_0}$, q the rescaled position $q = \frac{\Theta}{2\pi}$ and t the rescaled time $t = \frac{\tilde{t}}{\tau}$. Now all free parameters are combined using the kicking strength $k = \frac{P\tau}{mr}$.

For the quantum mechanical description the Schrödinger equation has to be rescaled as well

$$i\hbar \frac{d}{dt} \tilde{\psi} = \tilde{H} \tilde{\psi} \quad (\text{A.6})$$

$$i \frac{\hbar \tau}{V_0 \tau} \frac{d}{dt} \tilde{\psi} = \frac{\tilde{H}}{V_0} \tilde{\psi} \quad (\text{A.7})$$

$$i \frac{\hbar}{V_0 \tau} \frac{d}{dt} \tilde{\psi} = H \tilde{\psi} \quad (\text{A.8})$$

$$i\hbar_{\text{eff}} \frac{d}{dt} \psi = H \psi , \quad (\text{A.9})$$

where the effective Planck constant $\hbar_{\text{eff}} = \frac{\hbar}{V_0 \tau}$ is defined. This quantity scales with the typical action $V_0 \tau$ of the system and goes to zero in the semiclassical limit. As the scaling factor of the wave function $\tilde{\psi}$ appears on both sides of the Schrödinger equation it is derived from the normalization condition

$$1 = \int_0^{2\pi} d\Theta |\tilde{\psi}|^2 = 2\pi \int_0^1 dq |\tilde{\psi}|^2 = \int_0^1 dq |\psi|^2 . \quad (\text{A.10})$$

Thus the rescaled wave function ψ is given by

$$\psi = \sqrt{2\pi} \tilde{\psi} . \quad (\text{A.11})$$

Using system-adapted units the number of free parameters is reduced, which allows to study the physical properties efficiently. Also the numerical calculations benefit from this procedure as the typical numbers are in the order of one, which ensures a good utilization of the limited range of floating point arithmetic. What is introduced as system-adapted units or rescaled physical variables is also called dimensionless variables in the literature as all quantities are divided by a typical scale, which has the same physical unit of measure.

For the billiard systems in this thesis a different set of units is used, which ensures the equivalence of the two dimensional Helmholtz equation with the Schrödinger equation. The Planck constant and the particle mass are fixed to $\hbar = 2m = 1$. Then the semiclassical limit is given by $E \rightarrow \infty$. The length scale for the mushroom billiard is defined by the radius R . However, for the experiments the SI unit meter is used.

A.2 Smoothing of designed maps

The designed maps are defined using piece wise linear functions, which allows to control the phase space structure in an easy way. However, for the quantum mechanical description continuous functions yield better results. Thus the discontinuous functions for the first derivatives

of the kinetic energy $T'(p)$ and the potential $V'(q)$ in Eq. (2.13) are smoothed

$$T'_s(p) = \int dx G_\varepsilon(p-x)T'(p), \quad V'_s(q) = \int dx G_\varepsilon(p-x)V'(q) \quad (\text{A.12})$$

by convolution with a Gaussian $G_\varepsilon(x)$ of width ε

$$G_\varepsilon(x) = \frac{1}{\sqrt{2\pi\varepsilon^2}} e^{-\frac{x^2}{2\varepsilon^2}}. \quad (\text{A.13})$$

Using the error function $\text{Erf}_\varepsilon(x)$

$$\text{Erf}_\varepsilon(x) = \int_{-\infty}^x G_\varepsilon(\tilde{x})d\tilde{x} \quad (\text{A.14})$$

one obtains the smoothed functions

$$V'_s(q) = \begin{cases} -k - rx - (1-r) \left(\text{Erf}_\varepsilon\left(x - \frac{1}{2}\right)\right) & (x \leq 0) \\ -k - rx + (1-r) \left(\text{Erf}_\varepsilon\left(-x - \frac{1}{2}\right)\right) & (x > 0) \end{cases} \quad (\text{A.15})$$

$$T'_s(p) = \begin{cases} -\tilde{T}'\left(p + \frac{1}{2}\right) & (p \leq -\frac{1}{4}) \\ \tilde{T}'(p) & (-\frac{1}{4} < p \leq \frac{1}{4}) \\ -\tilde{T}'\left(p - \frac{1}{2}\right) & (p > \frac{1}{4}) \end{cases} \quad (\text{A.16})$$

$$\tilde{T}'(p) = -\left(1 - \frac{s}{4}\right) + sp - 2s \left(p\text{Erf}_\varepsilon(p) + \varepsilon^2 G_\varepsilon(p)\right) + 2\text{Erf}_\varepsilon(p). \quad (\text{A.17})$$

For the quantum mechanics the function for the kinetic energy and potential are needed. They are obtained by integration

$$V_s(q) = (r-1) \left[\left(|x| - \frac{1}{2}\right) \text{Erf}_\varepsilon\left(|x| - \frac{1}{2}\right) + \varepsilon^2 G_\varepsilon\left(|x| - \frac{1}{2}\right) \right] - \frac{k^2}{2} - kx - \frac{rx^2}{2} \quad (\text{A.18})$$

$$T_s(p) = \begin{cases} \frac{1}{2} - \tilde{T}\left(p + \frac{1}{2}\right) - \tilde{T}\left(\frac{1}{4}\right) & (p \leq -\frac{1}{4}) \\ \tilde{T}(p) - \tilde{T}\left(\frac{1}{4}\right) & (-\frac{1}{4} < p \leq \frac{1}{4}) \\ \frac{1}{2} - \tilde{T}\left(p - \frac{1}{2}\right) - \tilde{T}\left(\frac{1}{4}\right) & (p > \frac{1}{4}) \end{cases}, \quad (\text{A.19})$$

where $\tilde{T}(p)$ is an auxiliary function

$$\tilde{T}(p) = -\left(1 - \frac{s}{4}\right)p + \frac{1}{2}sp^2 + (2-sp) \left(p\text{Erf}_\varepsilon(p) + \varepsilon^2 G_\varepsilon(p)\right) - s\varepsilon^2 \left(\text{Erf}_\varepsilon(p) - \frac{1}{2}\right). \quad (\text{A.20})$$

B Numerics with quantum maps

B.1 Time evolution of wave packets

For the time evolution of a quantum state $|\phi\rangle$ one applies the unitary time evolution operator U

$$|\phi(t+1)\rangle = U|\phi(t)\rangle, \quad (\text{B.1})$$

which is introduced in Sec. 2.2.1 for kicked maps. In this case the position representation is given by

$$\langle q_k | \phi(t+1) \rangle = \sum_{m=0}^{N-1} \langle q_k | e^{-\frac{i}{\hbar_{\text{eff}}}V(q)} e^{-\frac{i}{\hbar_{\text{eff}}}T(p)} | q_m \rangle \langle q_m | \phi(t) \rangle. \quad (\text{B.2})$$

The obvious, but not very efficient, method of computing the time evolution of $|\phi\rangle$ is done by matrix-vector multiplication, which requires $\mathcal{O}(N^2)$ operations. Using the completeness of the momentum basis in Eq. (B.2) leads to

$$\phi(q_k, t+1) = e^{-\frac{i}{\hbar_{\text{eff}}}V(q_k)} \sum_{m,n} e^{-\frac{i}{\hbar_{\text{eff}}}T(p_n)} \langle q_k | p_n \rangle \langle p_n | q_m \rangle \phi(q_m, t). \quad (\text{B.3})$$

Substituting the relations for $\langle q_k | p_n \rangle$, Eq. (2.35), and the lattice definitions Eqs. (2.25) and (2.26) gives

$$\phi(q_k, t+1) = \frac{1}{N} e^{-\frac{i}{\hbar_{\text{eff}}}V(q_k)} \sum_{m,n} e^{-\frac{i}{\hbar_{\text{eff}}}T(p_n)} e^{\frac{i}{\hbar_{\text{eff}}}(q_k - q_m)p_n} \phi(q_m, t) \quad (\text{B.4})$$

$$= \frac{1}{N} e^{-\frac{i}{\hbar_{\text{eff}}}V(q_k)} \sum_{m,n} e^{-\frac{i}{\hbar_{\text{eff}}}T(p_n)} e^{\frac{2\pi i}{N}(k-m)(n+n_p^{(0)}+\theta_q)} \phi(q_m, t). \quad (\text{B.5})$$

We obtain a formula that is easily implemented numerically

$$\phi(q_k, t+1) = \frac{1}{N} e^{-\frac{i}{\hbar_{\text{eff}}}V(q_k)} e^{\frac{2\pi i}{N}k(n_p^{(0)}+\theta_q)} \sum_{n=0}^{N-1} e^{\frac{2\pi i}{N}kn} e^{-\frac{i}{\hbar_{\text{eff}}}T(p_n)} \sum_{m=0}^{N-1} e^{-\frac{2\pi i}{N}mn} e^{-\frac{2\pi i}{N}m(n_p^{(0)}+\theta_q)} \phi(q_m, t). \quad (\text{B.6})$$

For better clarity we use the vector notation

$$\phi_m(t) = \phi(q_m, t) \qquad Q_k = e^{\frac{2\pi i}{N}k(n_p^{(0)} + \theta_q)} \qquad (\text{B.7})$$

$$T_n = e^{-\frac{i}{\hbar_{\text{eff}}}T(p_n)} \qquad V_k = \frac{e^{-\frac{i}{\hbar_{\text{eff}}}V(q_k)}}{N} \qquad (\text{B.8})$$

$$W_N = e^{-\frac{2\pi i}{N}} \qquad (\text{B.9})$$

and the definition of the discrete Fourier transform [79] of length N

$$F_k = \text{DFT}(N)_k^n \cdot f_n = \sum_{n=0}^{N-1} W_N^{kn} f_n \ . \qquad (\text{B.10})$$

The operator $\text{DFT}(N)_k^n$ transforms the vector f_n and due to the sum the index changes from n to k . The corresponding inverse Fourier transform is given by

$$f_n = \text{IDFT}(N)_n^k \cdot F_k = \sum_{k=0}^{N-1} W_N^{-kn} F_k \ . \qquad (\text{B.11})$$

One obtains a very efficient numerical algorithm for the time evolution

$$\phi_k(t+1) = Q_k V_k \text{IDFT}(N)_k^n \cdot T_n \text{DFT}(N)_n^m \cdot Q_m^* \phi_m(t) \ , \qquad (\text{B.12})$$

which contains vector multiplications with $\mathcal{O}(N)$ operations and discrete Fourier transformations. Efficient implementations, such as the ‘‘Fastest Fourier Transform in the West’’ FFTW [80], scale with $\mathcal{O}(N \log N)$ for any length N . However the best performance is achieved if N is a power of two. Thus as a result, the whole time evolution scales with $\mathcal{O}(N \log N)$ if a suitable Fourier transformation implementation is chosen. This approach is similar to the split-operator method, but here the factorization of the time evolution operator is exact.

For small N , the time evolution for long times can be done more efficiently by diagonalizing the time evolution operator matrix and expanding the initial state in the basis of eigenfunctions $|\psi_n\rangle$. Even in this case the algorithm in Eq. (B.12) can be used to compute the time evolution operator in position representation by time evolution of eigenstates of the position operator $|q_l\rangle$

$$U_{kl} = \langle q_k | U | q_l \rangle = \sum_{m=0}^{N-1} \langle q_k | U | q_m \rangle \langle q_m | q_l \rangle \qquad (\text{B.13})$$

$$= Q_k V_k \text{IDFT}(N)_k^n \cdot T_n \text{DFT}(N)_n^m \cdot Q_m^* \delta_{ml} \ . \qquad (\text{B.14})$$

If a single quantum state $|\phi\rangle$ is evolved for very long times, as it is done for the results of this thesis, further optimizations are possible. The iterative application of the time evolution

operator is done by

$$\phi_k(t+l) = [Q_k V_k \text{IDFT}(N)_k^n \cdot T_n \text{DFT}(N)_n^m \cdot Q_m^*]^l \phi_m(t) \quad (\text{B.15})$$

$$= Q_k [V_k \text{IDFT}(N)_k^n \cdot T_n \text{DFT}(N)_n^m \cdot]^l Q_m^* \phi_m(t) \quad , \quad (\text{B.16})$$

where we used implicit renaming of the indices from k to m for each step to avoid many new indices for all l time evolution operations. The vector multiplication of $Q_k^* Q_k$ cancels for successive applications: $Q_k^* Q_k = 1$.

For efficient numerical simulations on modern hardware one has to think about a parallelization of the most time consuming algorithms. Today at least two or four processors are standard in personal computers, and for demanding applications high performance computer clusters are used, which is only beneficial if the problem can be parallelized.

For most cases studied in this thesis, see Sec. 3.1, many initial states are evolved with slightly different time evolution operators to perform a phase average. This can be done in parallel without much effort and scales perfectly for small N . A performance limiting factor is the transfer speed between system memory and CPU. As long as the size of the whole vector is smaller than the cache of the processor the time evolution is very fast. For systems with more than one CPU and a shared cache memory this can lead to an unexpected performance drop of parallel time evolutions, because different processes require the same cache space and additional memory transfers are needed. For very large N the time evolution of a single quantum state can be already very time consuming as we usually perform about two million iterations until the flooding weights saturate, see Sec. 3.1.2. A phase average is not necessary in these cases. Thus, a parallelization of single time evolutions is useful. Although vector multiplications scale perfectly for this purpose, the Fourier transformations do not. Standard libraries such as the FFTW library provide parallel routines, which for small $N = 2^n$ give a small speed-up on two or four processors, but for large N the speed even decreases¹ compared to the single threaded algorithm.

Since the parallel FFTW is not sufficient for this purpose an OpenMP [81] parallelization of the whole time evolution is used. The idea is based on parallel FFT algorithms, which are discussed in Refs. [82, 83]. Therefore a single $\text{DFT}(N)$ is decomposed into M transformations

¹ Please note: These observations were made on a Linux system with a Intel® Core i7 860 processor, 8GB RAM and similar systems with Core 2 Duo or Core 2 Quad processors. The performance scaling may vary drastically for other systems especially if a different memory layout is available.

DFT(N/M) of smaller length, where N is a multiple of M and M threads are used

$$F_k = \text{DFT}(N)_k^n \cdot f_n = \sum_{n=0}^{N-1} e^{-\frac{2\pi i k n}{N}} f_n \quad (\text{B.17})$$

$$= \sum_{m=0}^{M-1} \sum_{j=0}^{N/M-1} e^{-\frac{2\pi i k (Mj+m)}{N}} f_{Mj+m} \quad \text{with } n = Mj + m \quad (\text{B.18})$$

$$= \sum_{m=0}^{M-1} W_N^{mk} \sum_{j=0}^{N/M-1} e^{-\frac{2\pi i k j}{N/M}} \tilde{f}(m)_j \quad \text{with } \tilde{f}(m)_j \equiv f_{Mj+m} \quad (\text{B.19})$$

$$= \sum_{m=0}^{M-1} W_N^{mk} \text{DFT}(N/M)_k^j \cdot \tilde{f}(m)_j \quad (\text{B.20})$$

The initial state vector is reordered, such that, in matrix notation, a transpose operation is done

$$\tilde{A}_{kl} = A_{lk} \quad \text{with } A_{kl} = f_{Ml+k} \quad \text{and } \tilde{A}_{kl} = \tilde{f}_{Mk+l} \quad , \quad (\text{B.21})$$

which allows to perform M Fourier transformations in parallel using standard single threaded libraries. The resulting vectors of length N/M are multiplied with phase factors W_N^{mk} and the sum in Eq. (B.20) is evaluated also in parallel to obtain the full DFT(N). This leads to the parallel time evolution algorithm:

1. multiply with the vector Q_m^* in parallel
2. rearrange the resulting vector
3. perform M different DFT(N/M) in parallel
4. evaluate the sum $\sum_{m=0}^{M-1} W_N^{mk}$ for all k and multiply with the vector T_k in parallel
5. transpose the resulting vector
6. perform M different IDFT(N/M) in parallel
7. evaluate the sum $\sum_{m=0}^{M-1} W_N^{-mk}$ for all k and multiply with the vector V_k in parallel
8. multiply with Q_m in parallel

In the iterative case only steps 2 – 7 are repeated as step 1 and 8 are canceling each other such as in Eq. (B.16). Although the total number of operations of the time evolution increases due to the sums in step 4 and 7, the performance gain by this parallelization increases with N and the number of processes. For example on a Intel® Core i7 860 CPU with $N = 5 \cdot 10^5$ the time evolution with four processors is about twice as fast as the single threaded version. The

algorithm works well with shared memory as at least in the steps 4 and 7 informations about the whole vector are needed. However if N is very large such that the quantum state vector is larger than the system memory an application of a parallel algorithm on more than one computer or a cluster with heterogeneous memory using “Message Passing Interface” (MPI) [84] techniques is the only possible solution and the performance compared to a single threaded algorithm is irrelevant.

B.2 Efficient calculations of the Husimi function

To compute the Husimi function of a quantum state $|\phi\rangle$ one needs coherent states on the torus. We use the position representation of the coherent state in the continuous form

$$\alpha^{\text{cont}}(q, \tilde{p}_0, \tilde{q}_0) = \left(\frac{\Re c}{\pi \hbar_{\text{eff}}} \right)^{1/4} \exp \left\{ -c \frac{(q - \tilde{q}_0)^2}{2 \hbar_{\text{eff}}} \right\} \exp \left\{ \frac{i}{\hbar_{\text{eff}}} \tilde{p}_0 q \right\} , \quad (\text{B.22})$$

where \tilde{p}_0 and \tilde{q}_0 are the expectation values of the momentum and position operator. The complex tilting factor c can be used to squeeze and rotate the coherent state in phase space, which is useful for instance to adapt the elliptical form of regular islands, in general $c = 1$. On the torus, the function of Eq. (B.22) is evaluated on the lattice points q_n and due to the periodic boundary condition one obtains

$$\alpha(q_n, \tilde{q}_0, \tilde{p}_0) = \left(\frac{2 \hbar_{\text{eff}} \Re c}{M_p^2} \right)^{1/4} \sum_{l=-\infty}^{\infty} \exp \left(-\frac{c}{2 \hbar_{\text{eff}}} (q_n - (\tilde{q}_0 + l M_q))^2 + i \frac{\tilde{p}_0 q_n}{\hbar_{\text{eff}}} + 2 \pi i \theta_q l \right) \quad (\text{B.23})$$

$$=: \left(\frac{2 \hbar_{\text{eff}} \Re c}{M_p^2} \right)^{1/4} \sum_{l=-\infty}^{\infty} \alpha_l(q_n, \tilde{q}_0 + l M_q, \tilde{p}_0) . \quad (\text{B.24})$$

The sum over l ensures that periodic images of the coherent state on the torus of length M_q are added using the Bloch phase factor $\exp(2\pi i \theta_q l)$. In contrast to the continuous representation α^{cont} , the standard vector normalization is used for α instead of the integral norm. Although the form of Eq. (B.23) is analytically correct, it is not efficient for numerical usage. For quantum systems on the torus the infinite sum can be reduced to just a few terms as the function is only evaluated on lattice points with $n \in [0, N - 1]$ and the absolute value of each summand $\alpha_l(q_n, \tilde{q}_0 + l M_q, \tilde{p}_0)$ decreases very fast away from the center of the Gaussian $\tilde{q}_0 + l M_q$. Therefore the contribution of terms with large $|l|$ is negligible. Only a limited accuracy can be achieved with numerical computations, which is useful in this case as the maximal relevant distance Δq from the center point $\tilde{q}_0 + l M_q$ can be calculated. Therefore we define the accuracy ϵ , which is

the smallest relative amplitude, we want to consider in $\alpha_l(q_n, \tilde{q}_0 + lM_q, \tilde{p}_0)$

$$\epsilon \geq \left| \frac{\alpha_l(q_{n_\epsilon}, \tilde{q}_0 + lM_q, \tilde{p}_0)}{\alpha_l(\tilde{q}_0 + lM_q, \tilde{q}_0 + lM_q, \tilde{p}_0)} \right| \quad (\text{B.25})$$

$$\epsilon \geq \exp \left(-\frac{\Re c}{2\hbar_{\text{eff}}} (q_{n_\epsilon} - (\tilde{q}_0 + lM_q))^2 \right) . \quad (\text{B.26})$$

Then the maximal relevant distance from the center of the Gaussian Δq is given by

$$\Delta q = \sqrt{-\frac{2\hbar_{\text{eff}}}{\Re c} \ln \epsilon} , \quad (\text{B.27})$$

which corresponds to a maximal relevant number of lattice points Δn

$$\Delta n = \left\lceil \frac{N}{M_q} \Delta q \right\rceil = \left\lceil M_p \sqrt{-\frac{\ln \epsilon}{\pi \hbar_{\text{eff}} \Re c}} \right\rceil . \quad (\text{B.28})$$

Thus the sum in Eq. (B.23) can be reduced to terms with $(|l| - 1)M_q < \Delta q$ and $l = 0$ as q_n is evaluated only within $0 \leq q_n < M_q$

$$\alpha(q_n, \tilde{q}_0, \tilde{p}_0) \approx \left(\frac{2\hbar_{\text{eff}} \Re c}{M_p^2} \right)^{\frac{1}{4}} \sum_{l=0, (|l|-1)M_q < \Delta q} \alpha_l(q_n, \tilde{q}_0 + lM_q, \tilde{p}_0) . \quad (\text{B.29})$$

The Husimi function is given by

$$\mathcal{H}_{|\phi\rangle}(\tilde{q}_0, \tilde{p}_0) = \frac{1}{\hbar_{\text{eff}}} |\langle \alpha(\tilde{q}_0, \tilde{p}_0) | \phi \rangle|^2 \quad (\text{B.30})$$

$$= \left(\frac{2\hbar_{\text{eff}} \Re c}{M_p^2} \right)^{\frac{1}{2}} \left| \sum_l \sum_{n=0}^{N-1} \alpha_l^*(q_n, \tilde{q}_0 + lM_q, \tilde{p}_0) \phi(q_n) \right|^2 . \quad (\text{B.31})$$

The numerical calculation of the double sum takes a lot of time. We can reduce the effort further by extending the wave vector $\phi(q_n)$ for lattice indices $n < 0$ or $n > N - 1$ using the relation

$$\phi(q_{n-N}) = \phi(q_n) \exp(-2\pi i \theta_q) . \quad (\text{B.32})$$

This allows to use only one term in the sum over l namely the term for $l = 0$ but extends the sum over n . To achieve the accuracy ϵ only $2\Delta n$ summands in the sum over n need to be considered. The center lattice point n_c is given by rounding of

$$n_c \approx \frac{N}{M_q} \tilde{q}_0 - n_q^{(0)} . \quad (\text{B.33})$$

One obtains an approximation for the Husimi function, which is accurate within numerical errors

$$\mathcal{H}_{|\phi\rangle}(\tilde{q}_0, \tilde{p}_0) \approx \left(\frac{2h_{\text{eff}} \Re c}{M_p^2} \right)^{\frac{1}{2}} \left| \sum_{n=n_c-\Delta n}^{n_c+\Delta n} \alpha_i^*(q_n, \tilde{q}_0 + lM_q, \tilde{p}_0) \phi(q_n) \right|^2 . \quad (\text{B.34})$$

Depending on the given accuracy and the effective Planck constant this single sum contains usually much less than N terms. For example if $M_q = 144$, $M_p = 1$, $N = 4265$, and an accuracy of $\epsilon = 10^{-15}$ only $2\Delta n = 38$ terms have to be considered. To reduce the numerical errors in this calculation the sum should be evaluated in an alternating way, starting with $n = n_c - \Delta n$ and $n = n_c + \Delta n$ till $n = n_c$ as the loss of significance occurs by adding or subtracting values of strongly different magnitudes.

The Husimi function usually is calculated on a two dimensional grid in phase space, which allows for trivial parallelization, e.g. using OpenMP techniques. The benchmark results on processors with HyperThreading capability for this algorithm show, that it is beneficial to use as many threads as there are logical processor units for the system.

B.3 Numerical errors in the regular weight

Many results of this thesis are supported by numerical calculations of the regular weight p_m^{reg} of a time evolved wave packet ϕ . Therefore one has to make sure that numerical errors are not growing too fast. Usually a wave packet is iterated two million times by applying the time evolution operator. To test the influence of unavoidable numerical errors we apply after every time step an extra noise term to every element in the wave vector

$$\langle q_m | \phi(t+1) \rangle = \sum_n \langle q_m | \hat{U} | q_n \rangle \langle q_n | \phi(t) \rangle + a\xi_m , \quad (\text{B.35})$$

where ξ_m is a complex random number with uniformly distributed real and imaginary part between $-1/2$ and $1/2$. The amplitude a controls the magnitude of the noise. We obtain a noisy regular weight $p_{m \text{ noise}}^{\text{reg}}(t)$, which is computed for the same quantum map using the same initial condition as the usual regular weight $p_m^{\text{reg}}(t)$, defined in Eq. (3.12), but by applying the time evolution of Eq. (B.35). The difference of the regular weight and the noisy regular weight, is given by

$$\Delta p_{m \text{ noise}}^{\text{reg}}(a, t) = |p_m^{\text{reg}}(t) - p_{m \text{ noise}}^{\text{reg}}(a, t)| . \quad (\text{B.36})$$

The results are shown in Fig. B.1 for different noise amplitudes a . All amplitudes are larger or equal to the expected numerical error of about 10^{-16} for double precision floating point values. The squared modulus in the definition of the regular weight, Eq. (3.12), leads to absolute errors, which are smaller than the noise amplitude for each time step. Even assuming a very large

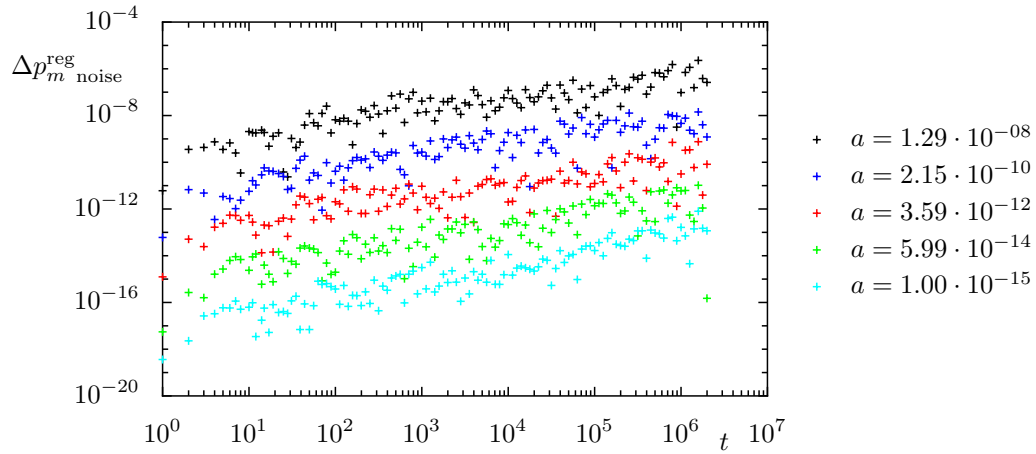


Figure B.1: Errors of the regular weight for the regular torus with $m = 8$ resulting by time evolution with an additional noise for each time step. The time evolution operator of quantum map \mathcal{M}_1 , see Sec. 2.1.2, is used with $N = 40$ and $M_q = 1$.

numerical error per time step of $a = 10^{-12}$ the increase of the error is so small that plateaus of regular weights larger than 10^{-9} can be used with sufficient certainty. There are additional sources for numerical errors, such as the construction of regular states. However these additional errors are not growing with time as it happens in the iterative algorithm of the time evolution.

C Analytic solutions of the matrix models

C.1 Saturation value

The saturation values are defined as the height of saturation plateaus of the flooding values, which contain information about the flooding of a particular regular torus. As there are M_q regular states on each regular torus one uses a matrix model with M_q regular states $|\chi_{\text{reg}_i}\rangle$ and N_{ch} chaotic states $|\chi_{\text{ch}_j}\rangle$. A wave packet $|\Phi(t)\rangle$, which is started in the chaotic sea, can be written for $t = 0$ as

$$|\Phi(0)\rangle = \sum_{j=1}^{N_{\text{ch}}} a_j e^{i\xi_j} |\chi_{\text{ch}_j}\rangle \quad , \quad \xi_j \in [0, 2\pi] \quad , \quad a_j \in [0, 1] \quad , \quad (\text{C.1})$$

and its expansion in the basis of the system $|\psi_i\rangle$ is given by

$$c_i = \langle \psi_i | \Phi(0) \rangle = \sum_{j=1}^{N_{\text{ch}}} a_j e^{i\xi_j} \langle \psi_i | \chi_{\text{ch}_j} \rangle \quad , \quad i = 1, \dots, N \quad . \quad (\text{C.2})$$

In contrast to the model with a single regular state the regular weights are obtained by summation, see Eq. (3.12)

$$p^{\text{reg}}(t) = \sum_{i=1}^{M_q} |\langle \chi_{\text{reg}_i} | \Phi(t) \rangle|^2 \quad . \quad (\text{C.3})$$

Every summand has the form

$$|\langle \chi_{\text{reg}_k} | \Phi(t) \rangle|^2 = \sum_{i,j=1}^{N_{\text{ch}}+M_q} c_i c_j^* e^{2\pi i(E_i - E_j)t} \langle \chi_{\text{reg}_k} | \psi_i \rangle \langle \psi_j | \chi_{\text{reg}_k} \rangle \quad (\text{C.4})$$

$$= \sum_{i=1}^{N_{\text{ch}}+M_q} |c_i|^2 |\langle \chi_{\text{reg}_k} | \psi_i \rangle|^2 \quad (\text{C.5})$$

$$+ 2\Re \left(\sum_{i>j} c_i c_j^* e^{2\pi i(E_i - E_j)t} \langle \chi_{\text{reg}_k} | \psi_i \rangle \langle \psi_j | \chi_{\text{reg}_k} \rangle \right) \quad . \quad (\text{C.6})$$

The second sum gives only rapid oscillations, which are uncorrelated for large times. For the saturation value we concentrate on the first term

$$s = \frac{N_{\text{ch}} + M_q}{M_q} \sum_{k=1}^{M_q} \sum_{i=1}^{N_{\text{ch}}+M_q} \langle \langle |c_i|^2 \rangle_{\text{initial}} |\langle \chi_{\text{reg}_k} | \psi_i \rangle|^2 \rangle_{\text{ensemble}} . \quad (\text{C.7})$$

This equation contains two averages. The first is an ensemble average that affects both the $|\psi_i\rangle$ and the $|c_i|^2$. While the second average is a variation of initial conditions, which affects only the $|c_i|^2$. The latter average is applied by considering

$$\langle |c_i|^2 \rangle_{\text{initial}} = \left\langle \sum_{j,k=1}^{N_{\text{ch}}} \langle \psi_i | \chi_{\text{ch}_j} \rangle \langle \chi_{\text{ch}_k} | \psi_i \rangle e^{i(\xi_j - \xi_k)} a_j a_k \right\rangle_{\text{initial}} \quad (\text{C.8})$$

$$= \left\langle \sum_{j=1}^{N_{\text{ch}}} |\langle \psi_i | \chi_{\text{ch}_j} \rangle|^2 a_j^2 \right\rangle_{\text{initial}} + \left\langle \sum_{j \neq k}^{N_{\text{ch}}} \langle \psi_i | \chi_{\text{ch}_j} \rangle \langle \chi_{\text{ch}_k} | \psi_i \rangle e^{i(\xi_j - \xi_k)} a_j a_k \right\rangle_{\text{initial}} , \quad (\text{C.9})$$

where the second term vanishes because of independent random phases ξ_j and one obtains

$$\langle |c_i|^2 \rangle_{\text{initial}} = \frac{1}{N_{\text{ch}}} \sum_{j=1}^{N_{\text{ch}}} |\langle \psi_i | \chi_{\text{ch}_j} \rangle|^2 \quad (\text{C.10})$$

$$= \frac{1}{N_{\text{ch}}} \left(1 - \sum_{k=1}^{M_q} |\langle \chi_{\text{reg}_k} | \psi_i \rangle|^2 \right) . \quad (\text{C.11})$$

The completeness of the basis formed by regular and chaotic states is used in this derivation. Combining Eqs. (C.10) and (C.7) yields

$$s = \frac{N_{\text{ch}} + M_q}{N_{\text{ch}}} \left(1 - \frac{1}{M_q} \sum_{i,j=1}^{M_q} \sum_k^{N_{\text{ch}}+M_q} \left\langle |\langle \psi_k | \chi_{\text{reg}_i} \rangle|^2 |\langle \psi_k | \chi_{\text{reg}_j} \rangle|^2 \right\rangle_{\text{ensemble}} \right) . \quad (\text{C.12})$$

Considering the extremal case of no flooding, we find that purely regular states are eigenstates of the system. Thus for each of the M_q purely regular states just one term $|\langle \psi_k | \chi_{\text{reg}_j} \rangle|^2$ is different from zero and equal to one. As all purely regular states are linearly independent, only the diagonal terms in the double sum contribute and the expected result, a vanishing saturation value, is obtained

$$s_{\text{no flooding}} = \frac{N_{\text{ch}} + M_q}{N_{\text{ch}}} \left(1 - \frac{1}{M_q} \sum_{i=1}^{M_q} \sum_k^{N_{\text{ch}}+M_q} \left\langle |\langle \psi_k | \chi_{\text{reg}_i} \rangle|^4 \right\rangle_{\text{ensemble}} \right) \quad (\text{C.13})$$

$$= \frac{N_{\text{ch}} + M_q}{N_{\text{ch}}} \left(1 - \frac{1}{M_q} \sum_{i=1}^{M_q} 1 \right) \quad (\text{C.14})$$

$$= 0 . \quad (\text{C.15})$$

The maximum saturation value corresponds to the complete flooding. In this case the average of the probability $|\langle \psi_k | \chi_{\text{reg}_j} \rangle|^2$ is one over the number of states in the system $N_{\text{ch}} + M_q$ as all basis functions are needed to expand a purely regular state. And we find the maximal saturation value

$$s_{\text{complete flooding}} = \frac{N_{\text{ch}} + M_q}{N_{\text{ch}}} \left(1 - \frac{1}{M_q} \sum_{i,j=1}^{M_q} \sum_k^{N_{\text{ch}}+M_q} \left(\frac{1}{N_{\text{ch}} + M_q} \right)^2 \right) \quad (\text{C.16})$$

$$= \frac{N_{\text{ch}} + M_q}{N_{\text{ch}}} \left(1 - \frac{1}{M_q} \sum_{i,j=1}^{M_q} \frac{1}{N_{\text{ch}} + M_q} \right) \quad (\text{C.17})$$

$$= \frac{N_{\text{ch}} + M_q}{N_{\text{ch}}} \left(1 - \frac{M_q}{N_{\text{ch}} + M_q} \right) \quad (\text{C.18})$$

$$= 1 \ . \quad (\text{C.19})$$

C.2 Two by two coupling model

We want to model the coupling of regular and chaotic states for quantum maps using a 2×2 matrix model system. Thus, we consider a model Hamiltonian H in the basis of one regular state χ_{reg} and one chaotic state χ_{ch}

$$H = \begin{pmatrix} \kappa & v \\ v & -\kappa \end{pmatrix} \ , \quad (\text{C.20})$$

where v is the coupling matrix element and κ and $-\kappa$ are the energies of the uncoupled states χ_{ch} and χ_{reg} , which are given in matrix notation

$$\chi_{\text{reg}} = \begin{pmatrix} 0 \\ 1 \end{pmatrix} \quad \chi_{\text{ch}} = \begin{pmatrix} 1 \\ 0 \end{pmatrix} \ . \quad (\text{C.21})$$

The time-independent Schrödinger equation is given by

$$Hx_i = e_i x_i \ . \quad (\text{C.22})$$

As this model is used to compare with results obtained by quantum maps, where the corresponding eigenequation contains a unitary operator with a spectrum of periodic eigenphases on the unit circle, we choose the appropriate dimensions of time and energy such that the time evolution operator of one unit in time τ has the same eigenvectors and the eigenvalues e_i are equivalent to the eigenphases φ_i , see Eq. (2.29)

$$Ux_i = e^{-2\pi i H} x_i = e^{-2\pi i e_i} x_i \ . \quad (\text{C.23})$$

This implies $\frac{\tau}{h} = 1$ and we vary the parameter κ in the interval

$$\kappa \in \left[-\frac{1}{2}, \frac{1}{2} \right] , \quad (\text{C.24})$$

which yields all possible realizations of a corresponding quantum map as an eigenphase spectrum is restricted to an interval of length one. The eigenvalues for this system are given by

$$e_1 = \sqrt{\kappa^2 + v^2} \quad e_2 = -\sqrt{\kappa^2 + v^2} \quad (\text{C.25})$$

and the corresponding normalized eigenvectors by

$$x_1 = \begin{pmatrix} \frac{v}{\sqrt{v^2 + (\sqrt{\kappa^2 + v^2 - \kappa})^2}} \\ \frac{\sqrt{\kappa^2 + v^2 - \kappa}}{\sqrt{v^2 + (\sqrt{\kappa^2 + v^2 - \kappa})^2}} \end{pmatrix} \quad x_2 = \begin{pmatrix} -\frac{v}{\sqrt{v^2 + (\sqrt{\kappa^2 + v^2 + \kappa})^2}} \\ \frac{\sqrt{\kappa^2 + v^2 + \kappa}}{\sqrt{v^2 + (\sqrt{\kappa^2 + v^2 + \kappa})^2}} \end{pmatrix} . \quad (\text{C.26})$$

To compute the flooding values, a wave packet $\psi(t=0)$ is prepared in the chaotic sea

$$\psi(t=0) \stackrel{!}{=} \chi_{\text{ch}} = c_1 x_1 + c_2 x_2 . \quad (\text{C.27})$$

The corresponding expansion coefficients c_i in the eigenbasis are given by

$$c_1 = \frac{\sqrt{(\sqrt{\kappa^2 + v^2} + \kappa)^2 + v^2}}{2\sqrt{\kappa^2 + v^2}} \quad c_2 = -\frac{\sqrt{(\sqrt{\kappa^2 + v^2} - \kappa)^2 + v^2}}{2\sqrt{\kappa^2 + v^2}} . \quad (\text{C.28})$$

This allows to compute the time-dependent flooding values using Eq. (3.14)

$$f(t) = (N_{\text{ch}} + 1) \langle |\langle \chi_{\text{reg}} | \psi(t) \rangle|^2 \rangle_{\kappa} \quad (\text{C.29})$$

$$= 2 \left\langle \left| c_1 e^{2\pi i t \sqrt{\kappa^2 + v^2}} \langle \chi_{\text{reg}} | x_1 \rangle + c_2 e^{-2\pi i t \sqrt{\kappa^2 + v^2}} \langle \chi_{\text{reg}} | x_2 \rangle \right|^2 \right\rangle_{\kappa} . \quad (\text{C.30})$$

We assume a simplified ensemble average over different κ , which is realized by integration over all possible values using the symmetry with respect to $\kappa = 0$

$$f(t) = \left\langle v^2 \frac{1 - \cos(4\pi t \sqrt{\kappa^2 + v^2})}{\kappa^2 + v^2} \right\rangle_{\kappa} \quad (\text{C.31})$$

$$= 2v^2 \int_0^{\frac{1}{2}} d\kappa \frac{1 - \cos(4\pi t \sqrt{\kappa^2 + v^2})}{\kappa^2 + v^2} . \quad (\text{C.32})$$

Substituting $\delta = \frac{\kappa}{v}$ one obtains

$$f(t) = 2v \int_0^{\frac{1}{2v}} d\delta \frac{1 - \cos(4\pi vt \sqrt{\delta^2 + 1})}{\delta^2 + 1} . \quad (\text{C.33})$$

The integrand is always greater than zero, whereas it is approaching zero for large δ . For small coupling matrix elements v we approximate the upper integration limit $\frac{1}{2v} \approx \infty$, and we evaluated using Ref. [85, pages 429 and 653]

$$f(t) \approx 2v \int_0^{\infty} d\delta \frac{1 - \cos(4\pi vt \sqrt{\delta^2 + 1})}{\delta^2 + 1} \quad (\text{C.34})$$

$$= 2v \int_1^{\infty} dz \frac{1 - \cos(4\pi vt z)}{z \sqrt{z^2 - 1}} \quad (\text{C.35})$$

$$= 2v \int_0^{4\pi vt} da \int_1^{\infty} dz \frac{\sin(az)}{\sqrt{z^2 - 1}} \quad (\text{C.36})$$

$$= 2v \int_0^{4\pi vt} da \frac{\pi}{2} \mathbf{J}_0(a) \quad (\text{C.37})$$

$$= 4\pi^2 v^2 t \left(\mathbf{J}_0(4\pi vt) - \frac{\pi}{2} (\mathbf{J}_0(4\pi vt) \mathbf{H}_1(4\pi vt) - \mathbf{J}_1(4\pi vt) \mathbf{H}_0(4\pi vt)) \right) . \quad (\text{C.38})$$

Here \mathbf{J}_n are the Bessel functions and \mathbf{H}_n the Struve functions of integer order n . The first derivative is already given by the derivation of $f(t)$

$$\dot{f}(t) = 4\pi^2 v^2 \mathbf{J}_0(4\pi vt) . \quad (\text{C.39})$$

Using the definition of the Bessel function for $n \geq 0$

$$\mathbf{J}_n(x) = \sum_{k=0}^{\infty} \frac{(-1)^k \left(\frac{x}{2}\right)^{n+2k}}{k!(n+k)!} \quad (\text{C.40})$$

one obtains an approximation for small arguments x

$$\mathbf{J}_0(x) \approx 1 - \frac{x^2}{4} + \frac{x^4}{64} \quad \text{and} \quad \mathbf{J}'_0(x) \approx -\frac{x}{2} + \frac{x^3}{16} , \quad (\text{C.41})$$

which gives the small-time behavior of the flooding value f

$$f\left(t \ll \frac{1}{4\pi v}\right) \approx f(0) + \dot{f}(0)t + \frac{\ddot{f}(0)}{2}t^2 = 4\pi^2 v^2 t . \quad (\text{C.42})$$

Thus the linear increase is obtained.

The evaluation of the saturation plateaus in Eq. (3.53) leads to the same result as the time average of Eq. (C.33) at large t and we obtain

$$f_\infty = 2 \left(1 - \left\langle \sum_{i=1}^2 |\langle \chi_{\text{reg}} | x_i \rangle|^4 \right\rangle_\kappa \right) \quad (\text{C.43})$$

$$= 2 \left(1 - \left\langle \frac{\kappa^2 + \frac{v^2}{2}}{\kappa^2 + v^2} \right\rangle_\kappa \right) \quad (\text{C.44})$$

$$= 2v \int_0^{\frac{1}{2v}} d\delta \frac{1}{\delta^2 + 1} \quad (\text{C.45})$$

$$= 2v \arctan \left(\frac{1}{2v} \right) . \quad (\text{C.46})$$

C.3 Non-transporting islands

For non-transporting islands the matrix model with the Hamilton H is considered

$$H = \begin{pmatrix} -\kappa & V & \cdots & V \\ V & \kappa & & 0 \\ \vdots & & \ddots & \\ V & 0 & & \kappa \end{pmatrix} . \quad (\text{C.47})$$

To solve the corresponding eigenequation the characteristic polynomial is derived via expansion in subdeterminants with respect to the last row

$$d_{M_q}(\lambda) = (-1)^{M_q+2} V \begin{vmatrix} V & \cdots & V \\ \kappa - \lambda & & 0 & 0 \\ & \ddots & & \vdots \\ 0 & & \kappa - \lambda & 0 \end{vmatrix} + (\kappa - \lambda) d_{M_q-1}(\lambda) \quad (\text{C.48})$$

$$= -V^2 (\kappa - \lambda)^{M_q-1} + (\kappa - \lambda) d_{M_q-1}(\lambda) . \quad (\text{C.49})$$

In the second step an expansion with respect to the last column is made. Using $d_0(\lambda) = -\kappa - \lambda$ we obtain by recursive application of Eq. (C.49) the whole polynomial

$$d_{M_q}(\lambda) = (\lambda^2 - \kappa^2 - M_q V^2) (\kappa - \lambda)^{M_q-1} . \quad (\text{C.50})$$

The solutions for $d_{M_q}(\lambda) = 0$, and thus the eigenvalues of the Hamilton matrix H , are given by

$$\lambda_{0,1} = \pm \sqrt{\kappa^2 + M_q V^2} \quad \lambda_{2..M_q+1} = \kappa . \quad (\text{C.51})$$

D Adjustment of the antenna positioning in the microwave billiard experiment

One of the technical challenges of the microwave billiard experiment presented in this thesis is the positioning of the moving antenna. In contrast to other experiments for measuring wave function data, where both antennas are fixed and the whole resonator is moved against the top plate [69], here the top plate is fixed with respect to the resonator. The moving antenna is inserted through holes with a diameter of 2.0 mm, which allows large billiard dimensions.

In Fig. D.1 a scheme of the top view of the experimental setup is displayed. As the antenna (6) with a diameter of 1.4 mm is almost as large as the holes in the resonator, a very accurate control of the positioning on the two dimensional grid, with 5 mm distance between the holes (5), is needed. The accuracy of the servo motor control unit is very high and allows for 0.01

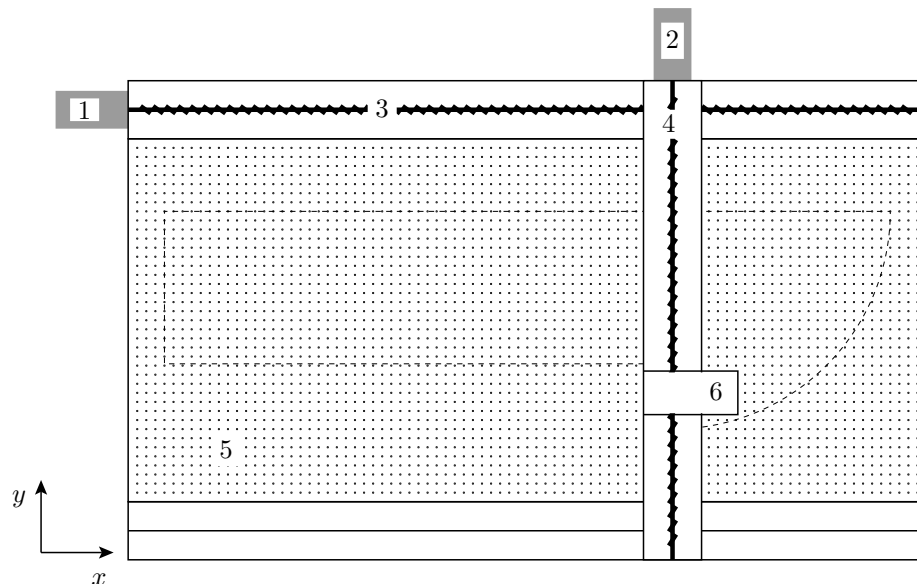


Figure D.1: Drawing of the experimental setup in top view. The servo motor in x -direction (1) drives the spindle (3) and the servo motor in y -direction (2) the spindle (4), which is located within a moving bar. The antenna (6) is inserted through the top plate (5) with a grid of holes.

mm steps. However this accuracy is not achieved in the positioning. The servo motors (1/2) are moving slides via spindles (3/4), which are limited technically such that a small clearance leads to errors after changing the direction of the antenna. Also the moving bar, which contains the spindle (4) is driven only from one side. This results in a small tilting of the bar, which leads to direction dependent errors.

Additionally the fabrication of the top plate with the grid of holes is a source for absolute positioning errors. The main contributions of these errors are a rotation of the whole grid compared to the coordinate system and relative misalignment of subparts of the grid, which is caused by a shifting during the fabrication because of the large size of the top plate, that does not fit in the machine.

A lot of these errors in the positioning are random errors. These can be tolerated to some extent by a mechanical centering of the antenna. The tilt or even small misalignments can be measured and compensated by an appropriate transformation of the coordinate system. The antenna is shown in Fig. D.2. It is mounted with a clearance, which allows movements up to a total of 1 mm in x - and y -direction. The additional bolts are conical and reach the grid before the antenna is inserted. The antenna is centered by the bolts, which only penetrate into the top plate and do not reach the resonator as they are supported with springs and are pressed back into messing cylinders.

To minimize systematic errors caused by a tilt or misalignments of the grid we use a manual adjustment. Therefore the absolute coordinates of the grid are measured manually to find a transformation for the grid matrix, which allows a full automatic measurement of the transmis-

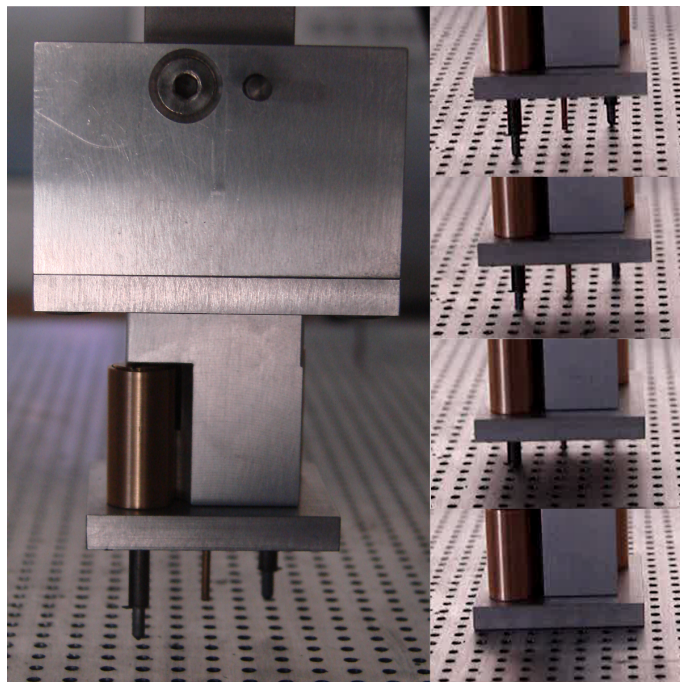


Figure D.2: Mechanical mount of the antenna, which tolerates positioning errors. Two conical bolts center the antenna before it is inserted in the resonator.

sion. The grid matrix contains the coordinates of the holes in multiples of 5 mm. Using a fixed mount without the centering mechanism for the antenna, some points $(x_{\text{grid}}, y_{\text{grid}})$ distributed over the whole grid are selected and the coordinates relative to an arbitrarily chosen center are measured such that the antenna is centered in each particular hole, which results in the real coordinates $(x_{\text{meas}}, y_{\text{meas}})$. Every grid point is approached from two directions varying both x - and y -coordinates to average over directional errors. This averaged data is shown in Tab. D.1.

To visualize the data we evaluate the difference of the measured data and the coordinates of the grid matrix

$$\begin{pmatrix} \Delta x \\ \Delta y \end{pmatrix} = \begin{pmatrix} x_{\text{meas}} \\ y_{\text{meas}} \end{pmatrix} - \begin{pmatrix} x_{\text{grid}} \\ y_{\text{grid}} \end{pmatrix}. \quad (\text{D.1})$$

In Fig. D.3 the selected grid points (blue) are shown together with the measured data $(\tilde{x}_{\text{meas}}, \tilde{y}_{\text{meas}})$ (red). The difference to the grid points is multiplied by 100 to make deviations visible

$$\begin{pmatrix} \tilde{x}_{\text{meas}} \\ \tilde{y}_{\text{meas}} \end{pmatrix} = \begin{pmatrix} x_{\text{grid}} \\ y_{\text{grid}} \end{pmatrix} + 100 \begin{pmatrix} \Delta x \\ \Delta y \end{pmatrix}. \quad (\text{D.2})$$

| $x_{\text{grid}}/\text{mm}$ | $y_{\text{grid}}/\text{mm}$ | $x_{\text{meas}}/\text{mm}$ | $y_{\text{meas}}/\text{mm}$ | $x_{\text{grid}}/\text{mm}$ | $y_{\text{grid}}/\text{mm}$ | $x_{\text{meas}}/\text{mm}$ | $y_{\text{meas}}/\text{mm}$ |
|-----------------------------|-----------------------------|-----------------------------|-----------------------------|-----------------------------|-----------------------------|-----------------------------|-----------------------------|
| 0 | 0 | 0.00 | 0.00 | -435 | 235 | -435.55 | 234.85 |
| -335 | 235 | -335.65 | 234.85 | -235 | 235 | -235.65 | 234.90 |
| -135 | 235 | -135.65 | 234.90 | -35 | 235 | -35.55 | 235.00 |
| 65 | 235 | 64.45 | 235.10 | 165 | 235 | 164.50 | 235.10 |
| 265 | 235 | 264.55 | 235.10 | 365 | 235 | 364.65 | 235.20 |
| 465 | 235 | 464.55 | 235.25 | 565 | 235 | 564.45 | 235.30 |
| 565 | 135 | 564.75 | 135.20 | 465 | 135 | 464.85 | 135.15 |
| 365 | 135 | 364.85 | 135.20 | 265 | 135 | 264.80 | 135.15 |
| 165 | 135 | 164.75 | 135.10 | 65 | 135 | 64.70 | 135.00 |
| -35 | 135 | -35.35 | 135.00 | -135 | 135 | -135.35 | 134.90 |
| -235 | 135 | -235.45 | 134.85 | -335 | 135 | -335.45 | 134.80 |
| -435 | 135 | -435.35 | 134.75 | -435 | 35 | -435.15 | 34.70 |
| -335 | 35 | -335.15 | 34.80 | -235 | 35 | -235.15 | 34.85 |
| -135 | 35 | -135.15 | 34.90 | -35 | 35 | -35.15 | 35.05 |
| 65 | 35 | 64.90 | 35.10 | 165 | 35 | 164.95 | 35.10 |
| 265 | 35 | 264.98 | 35.15 | 365 | 35 | 364.98 | 35.20 |
| 465 | 35 | 465.00 | 35.28 | 565 | 35 | 564.98 | 35.30 |
| 565 | -65 | 565.20 | -64.77 | 465 | -65 | 465.25 | -64.83 |
| 365 | -65 | 365.20 | -64.87 | 265 | -65 | 265.20 | -64.92 |
| 165 | -65 | 165.15 | -64.92 | 65 | -65 | 65.10 | -64.92 |
| -35 | -65 | -34.90 | -65.00 | -135 | -65 | -134.90 | -65.05 |
| -235 | -65 | -234.90 | -65.05 | -335 | -65 | -334.90 | -65.10 |
| -435 | -65 | -434.85 | -65.17 | | | | |

Table D.1: Manual measurement of grid points $(x_{\text{grid}}, y_{\text{grid}})$. The coordinates are measured approaching from two opposite directions and the averaged value is given as $(x_{\text{meas}}, y_{\text{meas}})$.

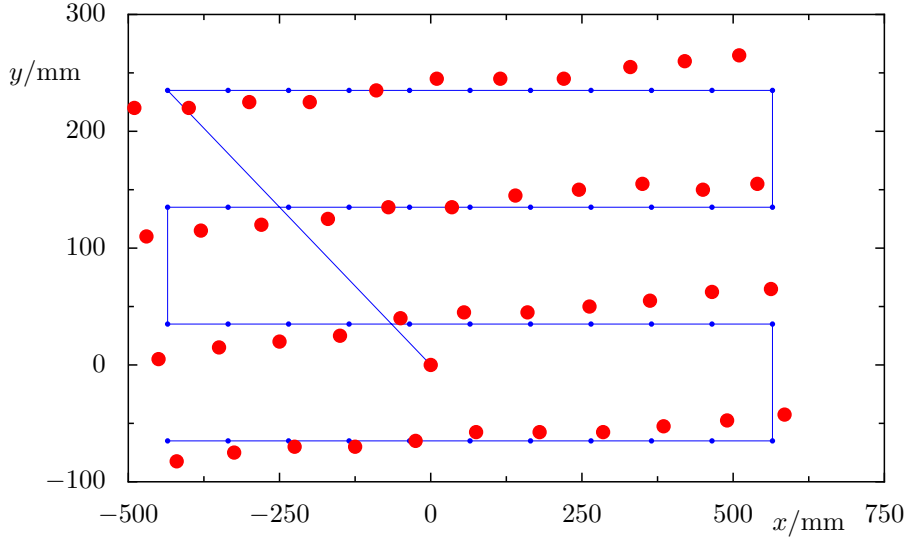


Figure D.3: Grid points $(x_{\text{grid}}, y_{\text{grid}})$ (blue) selected to calibrate the grid. The measured data is shown in red. The difference to the grid points is increased by a factor of 100, see Eq. (D.2).

Considering the measurement results a linear transformation of the grid points is sufficient to eliminate most of the differences. This is done by multiplying with a matrix T with four free parameters

$$\begin{pmatrix} t_{11} & t_{12} \\ t_{21} & t_{22} \end{pmatrix} \begin{pmatrix} x_{\text{grid}_0} & \cdots & x_{\text{grid}_n} \\ y_{\text{grid}_0} & \cdots & y_{\text{grid}_n} \end{pmatrix} = \begin{pmatrix} x_{\text{new}_0} & \cdots & x_{\text{new}_n} \\ y_{\text{new}_0} & \cdots & y_{\text{new}_n} \end{pmatrix}, \quad (\text{D.3})$$

where $(x_{\text{new}}, y_{\text{new}})$ represent the transformed grid coordinates, which are approximated by the measured data

$$\begin{pmatrix} t_{11} & t_{12} \\ t_{21} & t_{22} \end{pmatrix} \begin{pmatrix} x_{\text{grid}_0} & \cdots & x_{\text{grid}_n} \\ y_{\text{grid}_0} & \cdots & y_{\text{grid}_n} \end{pmatrix} \approx \begin{pmatrix} x_{\text{meas}_0} & \cdots & x_{\text{meas}_n} \\ y_{\text{meas}_0} & \cdots & y_{\text{meas}_n} \end{pmatrix}. \quad (\text{D.4})$$

Using the definitions

$$T = \begin{pmatrix} t_{11} & t_{12} \\ t_{21} & t_{22} \end{pmatrix}, \quad G = \begin{pmatrix} x_{\text{grid}_0} & \cdots & x_{\text{grid}_n} \\ y_{\text{grid}_0} & \cdots & y_{\text{grid}_n} \end{pmatrix}, \quad M = \begin{pmatrix} x_{\text{meas}_0} & \cdots & x_{\text{meas}_n} \\ y_{\text{meas}_0} & \cdots & y_{\text{meas}_n} \end{pmatrix}, \quad (\text{D.5})$$

we get

$$TG \approx M \quad (\text{D.6})$$

$$G^T T^T \approx M^T. \quad (\text{D.7})$$

To obtain the matrix elements one has to solve the minimization problem

$$\min_T \|G^T T^T - M^T\|_2, \quad (\text{D.8})$$

which is done by solving the equation

$$(GG^T)T^T = (GM^T) . \quad (\text{D.9})$$

Here, both (GG^T) and (GM^T) are 2×2 -matrices and the solution is obtained for example with the LAPACK routine 'dgesv', which yields the results listed in Tab. D.2. Without the transformation the maximal distance of the grid points and the measured points is

$$\max \left\| \begin{pmatrix} \Delta x \\ \Delta y \end{pmatrix} \right\|_2 = \max \left\| \begin{pmatrix} x_{\text{meas}} \\ y_{\text{meas}} \end{pmatrix} - \begin{pmatrix} x_{\text{grid}} \\ y_{\text{grid}} \end{pmatrix} \right\|_2 = 0.67 \text{ mm} , \quad (\text{D.10})$$

which is together with a directional error of about 0.2 mm more than the mechanical solution with a tolerance of at most 0.5 mm can handle. Using the transformation we obtain

$$\max \left\| \begin{pmatrix} \Delta \tilde{x} \\ \Delta \tilde{y} \end{pmatrix} \right\|_2 = \max \left\| \begin{pmatrix} x_{\text{meas}} \\ y_{\text{meas}} \end{pmatrix} - \begin{pmatrix} x_{\text{new}} \\ y_{\text{new}} \end{pmatrix} \right\|_2 = 0.13 \text{ mm} . \quad (\text{D.11})$$

This enables a full automatic measurement, which usually take several days to approach a few thousand grid points for each setup.

| | |
|----------|-------------------|
| t_{11} | 1.00018813980727 |
| t_{12} | -0.00231865628200 |
| t_{21} | 0.00047742772580 |
| t_{22} | 1.00001980334124 |

Table D.2: Transformation matrix elements obtained by minimization using the measured grid points.

Bibliography

- [1] A. Bäcker, R. Ketzmerick, S. Löck, M. Robnik, G. Vidmar, R. Höhmann, U. Kuhl and H.-J. Stöckmann: *Dynamical Tunneling in Mushroom Billiards*, Phys. Rev. Lett. **100** (2008) 174103 (4 pages).
- [2] Q. Jie Wang, C. Yan, L. Diehl, M. Hentschel, J. Wiersig, N. Yu, C. Pflügl, M. A. Belkin, T. Edamura, M. Yamanishi, H. Kan and F. Capasso: *Deformed microcavity quantum cascade lasers with directional emission*, New Journal of Physics **11** (2009) 125018 (19 pages).
- [3] S. Löck, A. Bäcker, R. Ketzmerick and P. Schlagheck: *Regular-to-Chaotic Tunneling Rates: From the Quantum to the Semiclassical Regime*, Phys. Rev. Lett. **104** (2010) 114101 (4 pages).
- [4] M. V. Berry and M. Tabor: *Closed orbits and the regular bound spectrum*, Proc. R. Soc. London Ser. A **349** (1976) 101–123.
- [5] O. Bohigas, M.-J. Giannoni and C. Schmit: *Characterization of chaotic quantum spectra and universality of level fluctuation laws*, Phys. Rev. Lett. **52** (1984) 1–4.
- [6] H.-J. Stöckmann and J. Stein: *“Quantum” chaos in billiards studied by microwave absorption*, Phys. Rev. Lett. **64** (1990) 2215–2218.
- [7] L. Markus and K. Meyer: *Generic Hamiltonian Dynamical Systems are neither Integrable nor Chaotic*, Mem. Amer. Math. Soc., American Mathematical Society, Providence, Rhode Island, (1974).
- [8] I. C. Percival: *Regular and irregular spectra*, J. Phys. B **6** (1973) L229–L232.
- [9] M. V. Berry: *Regular and irregular semiclassical wavefunctions*, J. Phys. A **10** (1977) 2083–2091.
- [10] A. Voros: *Semi-classical ergodicity of quantum eigenstates in the Wigner representation*, in: *Stochastic Behavior in Classical and Quantum Hamiltonian Systems*, Lecture Notes in Physics, 326–333, Springer-Verlag, Berlin, (1979).

- [11] O. Bohigas, S. Tomsovic and D. Ullmo: *Manifestations of classical phase space structures in quantum mechanics*, Phys. Rep. **223** (1993) 43–133.
- [12] T. Prosen and M. Robnik: *Distribution and fluctuation properties of transition probabilities in a system between integrability and chaos*, J. Phys. A **26** (1993) L319–L326.
- [13] B. Li and M. Robnik: *Separating the regular and irregular energy levels and their statistics in a Hamiltonian system with mixed classical dynamics*, J. Phys. A **28** (1995) 4843–4857.
- [14] G. Carlo, E. Vergini and A. Fendrik: *Numerical verification of Percival’s conjecture in a quantum billiard*, Phys. Rev. E **57** (1998) 5397–5403.
- [15] G. Veble, M. Robnik and J. Liu: *Study of regular and irregular states in generic systems*, J. Phys. A **32** (1999) 6423–6444.
- [16] J. Marklof, S. O’Keefe and S. Zelditch: *Weyl’s law and quantum ergodicity for maps with divided phase space (with an appendix Converse quantum ergodicity)*, Nonlinearity **18** (2005) 277–304.
- [17] M. V. Berry, N. L. Balazs, M. Tabor and A. Voros: *Quantum maps*, Annals of Physics **122** (1979) 26–63.
- [18] M. Kuś, J. Mostowski and F. Haake: *Universality of eigenvector statistics of kicked tops of different symmetries*, J. Phys. A **21** (1988) L1073–L1077.
- [19] J. P. Keating, F. Mezzadri and A. G. Monastra: *Nodal domain distributions for quantum maps*, J. Phys. A **36** (2003) L53–L59.
- [20] M. J. Davis and E. J. Heller: *Quantum dynamical tunneling in bound states*, J. Chem. Phys. **75** (1981) 246–254.
- [21] L. Hufnagel, R. Ketzmerick, M.-F. Otto and H. Schanz: *Eigenstates ignoring regular and chaotic phase-space structures*, Phys. Rev. Lett. **89** (2002) 154101 (4 pages).
- [22] A. Bäcker, R. Ketzmerick and A. G. Monastra: *Flooding of Chaotic Eigenstates into Regular Phase Space Islands*, Phys. Rev. Lett. **94** (2005) 054102 (4 pages).
- [23] A. Bäcker, R. Ketzmerick and A. G. Monastra: *Universality in the flooding of regular islands by chaotic states*, Phys. Rev. E **75** (2007) 066204 (11 pages).
- [24] J. Feist, A. Bäcker, R. Ketzmerick, S. Rotter, B. Huckestein and J. Burgdörfer: *Nanowires with Surface Disorder: Giant Localization Lengths and Quantum-to-Classical Crossover*, Phys. Rev. Lett. **97** (2006) 116804 (4 pages).

- [25] J. Feist, A. Bäcker, R. Ketzmerick, J. Burgdörfer and S. Rotter: *Nanowires with surface disorder: Giant localization length and dynamical tunneling in the presence of directed chaos*, Phys. Rev. B **80** (2009) 245322 (14 pages).
- [26] E. Persson, I. Rotter, H.-J. Stöckmann and M. Barth: *Observation of Resonance Trapping in an Open Microwave Cavity*, Phys. Rev. Lett. **85** (2000) 2478–2481.
- [27] E. Persson and I. Rotter: *Doorway concept at high excitation energy*, Phys. Rev. C **59** (1999) 164–171.
- [28] E. Persson, T. Gorin and I. Rotter: *Resonance trapping and saturation of decay widths*, Phys. Rev. E **58** (1998) 1334–1345.
- [29] H. Stöckmann and J. Stein: *“Quantum” chaos in billiards studied by microwave absorption*, Phys. Rev. Lett. **64** (1990) 2215–2218.
- [30] E. Doron, U. Smilansky and A. Frenkel: *Experimental demonstration of chaotic scattering of microwaves*, Phys. Rev. Lett. **65** (1990) 3072–3075.
- [31] S. Sridhar: *Experimental observation of scarred eigenfunctions of chaotic microwave cavities*, Phys. Rev. Lett. **67** (1991) 785–788.
- [32] H. Gräf, H. L. Harney, H. Lengeler, C. H. Lewenkopf, C. Rangacharyulu, A. Richter, P. Schardt and H. A. Weidenmüller: *Distribution of eigenmodes in a superconducting stadium billiard with chaotic dynamics*, Phys. Rev. Lett. **69** (1992) 1296–1299.
- [33] I. P. Cornfeld, S. V. Fomin and Ya. G. Sinai: *Ergodic Theory*, Grundlehren der Mathematischen Wissenschaften, Springer Verlag, New York, (1982).
- [34] E. Ott: *Chaos in Dynamical Systems*, Cambridge University Press, Cambridge, 2nd edn., (2002).
- [35] B. V. Chirikov: *A universal instability of many-dimensional oscillator systems*, Phys. Rep. **52** (1979) 263–379.
- [36] V. I. Arnold: *Proof of a theorem of A. N. Kolmogorov on the invariance of quasi-periodic motions under small perturbations of the Hamiltonian*, Russ. Math. Surv. **18** (1963) 9–36.
- [37] O. Brodier, P. Schlagheck and D. Ullmo: *Resonance-assisted tunneling in near-integrable systems*, Phys. Rev. Lett. **87** (2001) 064101 (4 pages).
- [38] O. Brodier, P. Schlagheck and D. Ullmo: *Resonance-Assisted Tunneling*, Ann. of Phys. **300** (2002) 88–136.

- [39] C. Eltschka and P. Schlagheck: *Resonance- and Chaos-Assisted Tunneling in Mixed Regular-Chaotic Systems*, Phys. Rev. Lett. **94** (2005) 014101 (4 pages).
- [40] P. Schlagheck, C. Eltschka and D. Ullmo: *Resonance- and Chaos-Assisted Tunneling*, in: *Progress in Ultrafast Intense Laser Science Volume I* (Eds. K. Yamanouchi, S. L. Chin, P. Agostini and G. Ferrante), vol. 84, 107–131, Springer-Verlag, Berlin, (2006).
- [41] R. S. MacKay, J. D. Meiss and I. C. Percival: *Stochasticity and Transport in Hamiltonian Systems*, Phys. Rev. Lett. **52** (1984) 697–700.
- [42] R. S. MacKay, J. D. Meiss and I. C. Percival: *Transport in Hamiltonian systems*, Physica D **13** (1984) 55–81.
- [43] J. Meiss: *Symplectic maps, variational principles, and transport*, Rev. Mod. Phys. **64** (1992) 795–848.
- [44] A. Bäcker: *Numerical aspects of eigenvalues and eigenfunctions of chaotic quantum systems*, in: *The Mathematical Aspects of Quantum Chaos I*, M. Degli Esposti and S. Graffi (Eds.), Springer Lecture Notes in Physics **618** (2003) 91–144.
- [45] H.-J. Stöckmann: *Quantum chaos*, Cambridge University Press, Cambridge, (1999).
- [46] S.-J. Chang and K.-J. Shi: *Evolution and exact eigenstates of a resonant quantum system*, Phys. Rev. A **34** (1986) 7–22.
- [47] J. P. Keating, F. Mezzadri and J. M. Robbins: *Quantum boundary conditions for torus maps*, Nonlinearity **12** (1999) 579–591.
- [48] H. Waalkens, J. Wiersig and H. R. Dullin: *Elliptic quantum billiard*, Annals of Physics **260** (1997) 50–90.
- [49] Ya. G. Sinai: *On the foundations of the ergodic hypothesis for a dynamical system of statistical mechanics*, Sov. Math. Dokl. **4** (1963) 1818–1822.
- [50] Ya. G. Sinai: *Dynamical systems with elastic reflections*, Russ. Math. Surveys **25** (1970) 137–189.
- [51] L. A. Bunimovich: *On ergodic properties of certain billiards*, Funct. Anal. Appl. **8** (1974) 254–255.
- [52] L. A. Bunimovich: *On the ergodic properties of nowhere dispersing billiards*, Commun. Math. Phys. **65** (1979) 295–312.
- [53] L. A. Bunimovich: *Mushrooms and other billiards with divided phase space*, Chaos **11** (2001) 802–808.

- [54] M. V. Berry: *Regularity and chaos in classical mechanics, illustrated by three deformations of a circular ‘billiard’*, Europ. J. Phys **2** (1981) 91–102.
- [55] T. Betcke and L. N. Trefethen: *Reviving the Method of Particular Solutions*, SIAM Rev. **47** (2005) 469–491.
- [56] T. Betcke: *The generalized singular value decomposition and the method of particular solutions*, MIMS EPrint **2006.396** (2006) (19 pages).
- [57] K. Husimi: *Some Formal Properties of the Density Matrix*, Proc. Phys.-Math. Soc. Japan **22** (1940) 264–314.
- [58] A. Bäcker, R. Ketzmerick, S. Löck and L. Schilling: *Regular-to-Chaotic Tunneling Rates Using a Fictitious Integrable System*, Phys. Rev. Lett. **100** (2008) 104101 (4 pages).
- [59] L. Schilling: *Direct dynamical tunneling in systems with a mixed phase space*, Ph.D. thesis, (2006).
- [60] S. Löck: *Dynamical Tunneling in Systems with a Mixed Phase Space*, Ph.D. thesis, (2010).
- [61] A. Bäcker, R. Ketzmerick and S.Löck: (in preparation).
- [62] C. Cohen-Tannoudji, B. Diu and F. Laloë: *Quantenmechanik Teil 2*, Walter de Gruyter, Berlin, 2nd edn., (1999).
- [63] A. Bäcker, R. Ketzmerick and A. G. Monastra: *Flooding of Chaotic Eigenstates into Regular Phase Space Islands*, Phys. Rev. Lett. **94** (2005) 054102 (4 pages).
- [64] F. Leyvraz and D. Ullmo: *The level splitting distribution in chaos-assisted tunnelling*, JPA **29** (1996) 2529–2551.
- [65] J. Zakrzewski, D. Delande and A. Buchleitner: *Ionization via chaos assisted tunneling*, Phys. Rev. E **57** (1998) 1458–1474.
- [66] C. Mahaux and H. A. Weidenmüller: *Shell-model approach to nuclear reactions*, North-Holland Pub. Co., Amsterdam, (1969).
- [67] F. H. M. Faisal and J. V. Moloney: *Time-dependent theory of non-Hermitian Schrödinger equation: application to multiphoton-induced ionisation decay of atoms*, J. Phys. B **14** (1981) 3603–3620.
- [68] T. Tanaka: *On existence of a biorthonormal basis composed of eigenvectors of non-Hermitian operators*, J. Phys. A **39** (2006) 7757–7761.
- [69] U. Kuhl: *Wave functions, nodal domains, flow, and vortices in open microwave systems*, Eur. Phys. J. Special Topics **145** (2007) 103–123.

- [70] J. Stein, H. J. Stöckmann and U. Stoffregen: *Microwave studies of billiard Green functions and propagators*, Phys. Rev. Lett. **75** (1995) 53–56.
- [71] R. Höhmann, U. Kuhl and H. Stöckmann: *Algebraic Fidelity Decay for Local Perturbations*, Phys. Rev. Lett. **100** (2008) 124101 (4 pages).
- [72] U. Kuhl, H. Stöckmann and R. Weaver: *Classical wave experiments on chaotic scattering*, J. Phys. A **38** (2005) 10433–10463.
- [73] U. Kuhl, R. Höhmann, H. Stöckmann and S. Gnutzmann: *Nodal domains in open microwave systems*, Phys. Rev. E **75** (2007) 036204 (7 pages).
- [74] S. A. van Langen, P. W. Brouwer and C. W. J. Beenakker: *Fluctuating phase rigidity for a quantum chaotic system with partially broken time-reversal symmetry*, Phys. Rev. E **55** (1997) 1–4.
- [75] T. Geisel, G. Radons and J. Rubner: *Kolmogorov-Arnol'd-Moser barriers in the quantum dynamics of chaotic systems*, Phys. Rev. Lett. **57** (1986) 2883–2886.
- [76] N. T. Maitra and E. J. Heller: *Quantum transport through cantori*, Phys. Rev. E **61** (2000) 3620–3631.
- [77] A. Ishikawa, A. Tanaka and A. Shudo: *Dynamical Tunneling in Many-Dimensional Chaotic Systems*, Phys. Rev. Lett. **104** (2010) 224102 (4 pages).
- [78] J. Wiersig and M. Hentschel: *Unidirectional light emission from high- Q modes in optical microcavities*, Phys. Rev. A **73** (2006) 031802 (4 pages).
- [79] W. H. Press, S. A. Teukolsky, W. T. Vetterling and B. P. Flannery: *Numerical Recipes in C. The Art of Scientific Computing*, Cambridge University Press, Cambridge, 2nd edn., (1992).
- [80] M. Frigo and S. G. Johnson: *The Design and Implementation of FFTW3*, Proceedings of the IEEE **93** (2005) 216–231, Special issue on “Program Generation, Optimization, and Platform Adaptation”.
- [81] *The OpenMP API specification for parallel programming*, <http://openmp.org/wp/>.
- [82] D. H. Bailey: *FFTs in external or hierarchical memory*, J. Supercomput. **4** (1990) 23–35.
- [83] D. Takahashi: *A parallel 1-D FFT algorithm for the Hitachi SR8000*, Parallel Comput. **29** (2003) 679–690.
- [84] *Message Passing Interface Forum*, <http://www.mpi-forum.org/>.

- [85] I. S. Gradshteyn and I. M. Ryzhik: *Table of Integrals, Series, and Products*, Academic Press, San Diego, 6th edn., (2000).

Danksagung

An dieser Stelle möchte ich Prof. Dr. Roland Ketzmerick für das interessante Thema, die vielseitige Unterstützung sowie zahlreiche hilfreiche Diskussionen herzlich danken. Darüber hinaus gilt mein besonderer Dank PD Dr. Arnd Bäcker für die Betreuung, umfangreiche Anregungen und die vielfältigen Hinweise zu meiner Arbeit.

Es war für mich eine außergewöhnliche Gelegenheit theoretische Untersuchungen auch experimentell prüfen zu können. Daher danke ich PD Dr. Ulrich Kuhl und Prof. Dr. Hans-Jürgen Stöckmann für eine lehrreiche und erfolgreiche Zusammenarbeit in Marburg.

Normann Mertig und Dr. Steffen Löck danke ich herzlich für zahlreiche, offene und erkenntnisreiche Diskussionen. Für das Korrekturlesen und wichtige Hinweise möchte ich mich bei PD Dr. Arnd Bäcker, Dr. Steffen Löck, Normann Mertig, Matthias Michler und PD Dr. Ulrich Kuhl bedanken.

Der gesamten Arbeitsgruppe Computational Physics verdanke ich eine freundschaftliche Atmosphäre geprägt von offenherziger und reger gegenseitiger Unterstützung.

Meiner gesamten Familie und besonders meiner Frau Eva möchte ich für viel Zuspruch, Unterstützung und ein großes Maß an Verständnis danken.

Diese Arbeit wurde von der Deutschen Forschungsgemeinschaft DFG im Rahmen der Forschergruppe 760 finanziert.

Die Grafiken dieser Arbeit wurden mit der Python-Bibliothek `PyXGraph` erstellt. Diese ermöglicht eine vereinfachte Nutzung von `PyX` (<http://pyx.sourceforge.net/>) um PostScript Grafiken mit `LATEX`-Schnittstelle zu generieren. Programme für numerische Berechnungen wurden in der Programmiersprache Python (<http://www.python.org>) mithilfe der Pakete NumPy und SciPy (<http://www.scipy.org>), sowie mit C++-Erweiterungen für rechenintensive Algorithmen erstellt.

Erklärung

Hiermit versichere ich, dass ich die vorliegende Arbeit ohne unzulässige Hilfe Dritter und ohne Benutzung anderer als der angegebenen Hilfsmittel angefertigt habe; die aus fremden Quellen direkt oder indirekt übernommenen Gedanken sind als solche kenntlich gemacht. Die Arbeit wurde bisher weder im Inland noch im Ausland in gleicher oder ähnlicher Form einer anderen Prüfungsbehörde vorgelegt.

Die Dissertation wurde in der Zeit von Januar 2007 bis Juni 2010 unter der Betreuung von Herrn Prof. Dr. Roland Ketzmerick am Institut für Theoretische Physik der Technischen Universität Dresden angefertigt. Es haben keine früheren erfolglosen Promotionsverfahren stattgefunden. Ich erkenne die Promotionsordnung der Fakultät Mathematik und Naturwissenschaften an der Technischen Universität Dresden vom 20. März 2000 an.

Dresden, den 23. Juni 2010

Lars Bittrich